Universidade de Brasília

Faculdade de Tecnologia

Departamento de Engenharia Mecânica

Magnetic emulsions in shear flow under external magnetic fields

Por

Lucas Hildebrand Pires da Cunha

Brasília

Julho 2018

Lucas Hildebrand Pires da Cunha

Magnetic emulsions in shear flow under external magnetic fields

Trabalho submetido ao Departamento de Engenharia Mecânica da Universidade de Brasília como requisito parcial para obtenção do Título de Mestre em Ciências Mecânicas.

Universidade de Brasília

Faculdade de Tecnologia

Orientador: Prof. Taygoara Felamingo de Oliveira, PhD.

Brasília

Julho 2018

Lucas Hildebrand Pires da Cunha

Magnetic emulsions in shear flow under external magnetic fields

Trabalho submetido ao Departamento de Engenharia Mecânica da Universidade de Brasília como requisito parcial para obtenção do Título de Mestre em Ciências Mecânicas.

Banca Examinadora

Prof. Taygoara Felamingo de Oliveira, PhD. – UnB/DF
Orientador

Prof. Francisco Ricardo da Cunha, PhD. – UnB/DF
Examinador 1

Prof. Yuri Dumaresq Sobral, PhD. – UnB/DF
Examinador 2

Brasília, 31 de julho de 2018.

Ao meu pai Divaldo, que hoje, em longa viagem, ainda

me ensina e sorri pelas lembranças do passado.

Acknowledgements

Due to the great amount of emotions content in the following words, those will be written in Portuguese.

Ao meu pai, Divaldo, homem sem o qual eu não estaria aqui, agora, escrevendo essas palavras. O qual eu ouvia adimirado ao se intitular engenheiro, o quê me fez seguir por tal caminho. Quem não mediu esforços para me criar da melhor maneira o possível, não me instruiu a ser um homem bom por palavras, mas por exemplos. Você, meu amado pai, é um exemplo concreto do que é ser um homem de bem. Se foi dessa vida sem deixar se quer uma mágoa ou desavença no coração de alguém, apenas boas lembranças. Eu queria ter te aproveitado mais. Ter dado mais valor às nossas longas conversas, e se possível fosse, extendê-las ainda mais. Por incrível que pareça, muitas das palavras por ti proferidas em meio a essas, e que apesar de encontrarem meus ouvidos passavam desapercebidas por meu interesse, hoje, ecoam em minhas memórias mostrando-se ensinamentos valiosos. Pois é meu velho, você fez a passagem, mas muito ainda ficou. Cada gesto e pensamento meu ainda traz, e sempre trará, mesmo que distante, um reflexo do que foi você. Até logo!

Ao professor Taygoara Felamingo de Oliveira, orientador e amigo, por toda a confiança em mim depositada durante os dois longos e conturbados anos deste mestrado. Pelas longas conversas, aulas, atenção, compreensão e tempo. Você é uma pessoa adimirável. Foi um grande prazer ter-lhe como orientador no meu mestrado, não poderia ter feito melhor escolha. Mesmo assim, ainda temos muito no que trabalharmos juntos. Foi só o começo de algo maior. Agradeço também a sua esposa, Isabel, pelas palavras de conforto e atenção em meio aos momentos difíceis.

Ao meu grande amigo, Ivan Rosa de Siqueira, por uma lista enorme de coisas que aqui não caberiam. Obrigado por sua contribuição direta nesta pesquisa, por todos os auxílios a mim concedidos em minha vida acadêmica, pelos tempo dedicado às pesquisas em que trabalhamos juntos, pela ajuda e incentivo nas apliações para o doutorado e por ser um amigo exemplar. Logo mais estou aí com você em Houston. Você é o cara.

Ao professor Francisco Ricardo da Cunha, pelo memorável curso de Mecânica dos Meios Contínuos, um divisor de águas em minha compreensão de Mecânica dos Fluidos.

Ao professor Éder Lima de Albuquerque, pela orientação no trabalho que resultou em meu primeiro artigo publicado em revista como autor principal. Ao professor Antônio Brasil Junior, por todo apoio durante o período em que fiz parte do grupo de pesquisa LEA.

À minha amada mãe, Vera, mulher forte e amoroza, que sempre me serviu de inspiração enquanto me concedia amor incondicional, e sempre me apoiou em meus sonhos não importa o qual fossem. Aos meus amados irmãos, Cássio e Vitor, os quais me serviram de exemplo nos mais diversos quesitos da vida. Aos meus amados sobrinhos, Marina e Caetano, que me fazem ter esperança no futuro do mundo por meio de seus jeitos sinceros e amorosos.

À minha namorada, Suelem, que foi fundamental na reta final de meu mestrado, período em que passei pelo momento mais difícil de minha vida. Você me serviu de suporte e porto seguro. Ouviu meus desabafos e suporto meus momentos de apatia. Serei eternamente grato por todo o carinho e atenção a mim concedidos.

Aos meus colegas de laboratório, Raphael, Nela, Vinícius, João, Miguel, Rafaela, Jhonny, Wesly e Ramsay, por todas as conversas construtivas sobre mecânica dos fluidos, bem como pelos papos furados na hora do café.

A todos os meus amigos que me apoiaram e incentivaram: Giordanno, Giovanni, Guilherme, Luiz, Guga, Caribé, Arthuzinho, Igor, Ítalo, Rachid, João, Kleniston, Fassheber, Carlos Couto, Rodrigo, Glawber, Manoel, Vinícius, Carlinhos, André, Joka, Luan, Marquinhos, André Yuji, Fred, Mario, Nuno, Christian, Dudu, Kayron, David, Cunha e Leo.

A TODOS da família Cerrado MMA, que me acolheram e foram fundamentais para a manutenção da minha saúde mental e física durante o meu mestrado. Serei eternamente grato. Vocês resgataram uma parte de mim que há tempo eu não via.

A todos os funcionários e servidores da Univeridade de Brasília sem os quais este trabalho não se faria possível.

Abstract

This work has analyzed the response of a planar ferrofluid droplet immersed in a non-magnetic Newtonian liquid to the combined action of an external magnetic field and a simple shear flow. A numerical methodology based on the Projection Method and the Level-Set Method has been developed to solve the magnetic field, the full Navier-Stokes equations with additional capillary and magnetic forces, and capture the liquid-liquid interface. The results show that the magnetic force has a strong influence on the droplet inclination and emulsion viscosity. The drop alignment with the magnetic field direction increases with the field intensity. When the external field is parallel to the flow direction, the drop strongly aligns with the streamlines of the flow, which reduces its contribution to emulsion viscosity. In turn, when the external field is perpendicular to the flow direction, the droplet inclination becomes higher, leading to a dramatic increase in the two-phase liquid viscosity. We also show that external magnetic fields can be used to control the drop rupture process in terms of time to breakup and size of the daughter drops. External fields applied in the flow direction delay the breakup process and reduce the size of the satellite drop. Remarkably, there is a critical magnetic capillary number above which the drop becomes so aligned with the flow that breakup does not happen. Alternatively, when the external field is applied perpendicularly to the flow direction, two opposite mechanisms dictate the breakup process. One the one hand, the drop inclination grows, which increases the shear forces that might lead to the rupture. On the other hand, the amount of liquid in the neck region of the deformed droplet also grows, which makes the breakup process more difficult. Thus, if the drop breaks, the magnetic field leads to a larger satellite drop. Finally, we also verified that external magnetic fields applied perpendicularly to the flow direction can be used to induce the breakup of drops that would not break under the shear action only. In summary, the results we present here highlight that external magnetic fields can be potentially used to control topological transformations of ferrofluid droplets and design magnetorheological emulsions with specific macroscopic material functions.

Key-words: magnetic emulsion; rheology; droplet rupture; Leve-Set.

Resumo

Este trabalho analisa a resposta de uma gota plana de ferrofluido imersa em um líquido new-toniano não magnético à ação combinada de um campo magnético externo e um escoamento cisalhante simples permanente. Uma metodologia numérica baseada no Método de Projeção e no Método Level-Set é desenvolvida para resolver o campo magnético, as equações completas de Navier-Stokes contemplando forças capilares e magnéticas, e capturar a interface líquido-líquido. Os resultados mostram que a força magnética exerce forte influência na inclinação da gota e na viscosidade da emulsão. O alinhamento da gota com a direção do campo magnético aplicado aumenta com a intensidade deste campo. Quando o campo externo é paralelo à direção do es-coamento, a gota se alinha fortemente com as linhas de corrente, o que reduz sua contribuição na viscosidade da emulsão. Por sua vez, quando o campo externo é perpendicular à direção do escomaneto, a inclinação da gota se torna mais alta, levando a um aumento dramático da vis-cosidade do fluido complexo resultante. Também mostramos que os campos magnéticos externos podem ser usados para controlar o processo de ruptura de gotas em termos de tempo para o rompimento e tamanho das gotas filhas. Campos externos aplicados na direção do escoamento atrasam o processo de ruptura e reduzem o tamanho da gota satélite. Notavelmente, há um número de capilaridade magnética crítico acima do qual a gota se torna tão alinhada com o escoamento que o rompimento não acontece. Alternativamente, quando o campo externo é apli-cado perpendicularmente à direção do escoamento, dois mecanismos opostos ditam o processo de ruptura. Por um lado, a inclinação da gota cresce, o que aumenta as forças de cisalhamento que podem levar à ruptura. Por outro lado, a quantidade de líquido na região do pescoço da gota deformada também cresce, o que torna o processo de ruptura mais difícil. Assim, se a gota romper, o campo magnético aumenta o tamanho da gota satélite. Finalmente, também verificamos que os campos magnéticos externos aplicados perpendicularmente à direção do es-coamento podem ser usados para induzir a ruptura de gotas que não iriam romper somente sob a ação do escoamento cisalhante. Em resumo, os resultados aqui apresentados destacam que os campos magnéticos externos podem ser potencialmente utilizados para controlar transformações topológicas de gotas de ferrofluido e projetar emulsões magnetoreológicas com funções específicas do material macroscópico.

Palavras-chaves: emulsão magnética; reologia; ruptura de gotas; Level-Set.

Contents

List of Figures

List of symbols

Latin symbols

$\boldsymbol{A}$	Matrix of the five-nodes stencil coefficients
a	Not deformed droplet radius
$a_{(i,j)}$	Coefficient of the left node of the five-nodes stencil
$\boldsymbol{B}$	Magnetic induction
$\boldsymbol{b}$	Product vector
$b_{(i,j)}$	Coefficient of the bottom node of the five-nodes stencil
c	Cut-off function
$c_{(i,j)}$	Coefficient of the center node of the five-nodes stencil
d	Particles diameter
$d_{(i,j)}$	Coefficient of the right node of the five-nodes stencil
e	Ellipse form factor
$\boldsymbol{E}$	Electrical field
$e_{(i,j)}$	Coefficient of the upper node of the five-nodes stencil
f	Generic continuous function
$\boldsymbol{f}$	Field force volume density
$\boldsymbol{f}_m$	Magnetic field force volume density
$\boldsymbol{F}_m$	Magnetic force
$\boldsymbol{F}_c$	Capillary force
$f_{(i,j)}$	Coefficient of the independent term of the five-nodes stencil
$\boldsymbol{H}$	Magnetic field

H	Magnetic field intensity
H_ε	Smoothed Heavyside function
H_p	Gap distance between the parallel plates
h	Cell size
$\boldsymbol{H}_0$	External magnetic field
$\boldsymbol{I}$	Identity tensor
i	Cell counter in the horizontal direction
j	Cell counter in the vertical direction
$\boldsymbol{J}$	Electric current
k	Boltzmann's constant
L	Side length of the square domain
L_p	Plates length
M	Magnetization intensity
$\boldsymbol{M}$	Magnetization
M_d	Particles magnetization
m_V	Mass of a volume
$\boldsymbol{n}$	Normal vector
N	Number of cells in a direction
N_x	Number of cells in the horizontal direction
N_y	Number of cells in the vertical direction
N_L	Region to proceed with the Level-Set reinitialization
n_x	Normal vector in the horizontal direction
n_y	Normal vector in the vertical direction

p	Arbitrary scalar function
p_h	Hydrodynamic pressure
S	Combined surfaces of the two plates
S_s	Smoothed signed function
t	Physical time
T	Absolute temperature
T_L	Level-Set tube
$\boldsymbol{u}$	Velocity vector
$\hat{\boldsymbol{u}}$	Velocity extrapolation in time
u	Velocity in the horizontal direction
U_p	Plates dislocation velocity
v	Velocity in the vertical direction
$\hat{x}$	Horizontal direction
$\boldsymbol{x}$	Eulerian position vector
$|x_s|$	Arc length metric
$\boldsymbol{x}_\Gamma$	Closest point at the interface to a given point
$\boldsymbol{X}$	Lagragian position vector
$\hat{y}$	Vertical direction

Greek symbols

α	Generic two-dimensional scalar function
$\boldsymbol{\alpha}$	Solution vector
α_t	First tube thickness

β_t	Second tube thickness
β_m	Volume fraction of magnetic particles
β_v	Dispersed to continuum phases volume fraction
Γ	Fluids interface
$\dot{\gamma}$	Shear rate
γ_t	Third tube thickness
Δx	Cell size in the horizontal direction
Δy	Cell size in the vertical direction
Δt	Time step
$\Delta \tau$	Virtual Time step
δ	Dirac delta function
δ_ε	Smoothed Dirac delta function
ε	Half of the artificial interface thickness
ϵ_0	Dielectric constant
ζ	Magnetic permeability ratio between the ferrofluid and the free space
ζ_ε	Smoothed magnetic permeability ratio
η	Continuous phase viscosity
$[\eta]$	Reduced viscosity
η_{eff}	Effective viscosity
θ	Angle
κ	Mean curvature
λ	Viscosity ratio between the dispersed and continuous phases
λ_ε	Smoothed viscosity ratio

μ	Magnetic permeability
μ_0	Free space magnetic permeability
ξ	Local coordinate
ρ	Fluids density
ρ_c	Electric charge density
$\boldsymbol{\sigma}$	Cauchy stress tensor
σ	Interfacial tension
$\langle \sigma_{xy} \rangle$	Average shear stress on the plates
τ_B	Brownian rotational diffusion characteristic time
τ_F	Flow characteristic time
τ_N	Néel characteristic time
τ	Virtual time
ϕ	Level-Set function
$\hat{\phi}$	Level-Set function extrapolation in time
χ	Magnetic susceptibility
ψ	Magnetic potential field
Ω	Volume of fluid domain
$\partial\Omega$	Volume of fluid boundary

Mathematical symbols

D/Dt	Material derivative operator
$D^{\pm}$	One side differences
∇	Gradient operator

$\nabla\cdot$ Divergence operator

$\nabla\times$ Curl operator

∇^2 Laplace operator

$\times$ Cross product

$\cdot$ Scalar product

$\cup$ Sets union

$\cap$ Sets intersection

$\perp$ Perpendicular to

Non-dimensional groups

Ca Capillary number

Ca_{mag} Magnetic capillary number

Re Reynolds number

Acronyms

ENO   Essentially Non-Oscillatory

TVD   Total Variation Diminishing

WENO   Weighted Essentially Non-Oscillatory

Life would be tragic if it weren't funny.

Stephen Hawking.

1 Introduction

1.1 Ferrofluids: principles and applications

Within the context of Fluid Mechanics, we usually refer to Ferrohydrodynamics as the field devoted to the study of the motion of ferrofluids – that is, colloidal suspensions of solid magnetic particles dispersed in a non-magnetic basis liquid – under the action of a flow field together with an external magnetic field. Typical ferrofluids are composed of nanoparticles of magnetite (Fe_3O_4) with diameters of the order of 10 nm suspended in a carrier liquid that can be either polar or non-polar, such as water or synthetic oils. Due to the small size of the suspended particles, the stabilization of ferrofluids is very complex and depends on different forces that act at the particle level, such as Brownian, van der Waals, electrical double layer, and magnetic forces between the particles and/or due to an external magnetic field. To avoid undesirable aggregation and keep the suspension stable, the magnetic particles are usually coated with surfactant molecules (surfaced ferrofluids) or electrical charges (ionic ferrofluids). Comprehensive introductions to ferrofluids and Ferrohydrodynamics are presented in the books by Rosensweig (1997) and Odenbach (2008, 2009).

A great and assorted literature in Ferrohydrodynamics has been developed in the last years, indicating the growing interest in this field. Indeed, ferrofluids play a key role in a wide range of applications in fluids engineering, materials processing, and biomedicine. For instance, magnetic fluids are a very promising alternative to develop less invasive drug delivery techniques (Lübbe et al., 2001; Voltairas et al., 2002; Puri & Ganguly, 2014). Ferrofluids and external magnetic fields can be also be used to induce drag reduction in pipe flows (Cunha & Sobral, 2005; Rosa et al., 2016) and stabilization of fluidized beds (Sobral & Cunha, 2003; Cunha et al., 2013). A new class of elastic polymeric materials has been studied using magnetic nanoparticles linked by DNA molecules to mimic polymer chains (Li et al., 2010; Byrom et al., 2014). In these cases, an external magnetic field can

be used to control the chain flexibility and persistence length, leading to a highly versatile artificial polymeric material. More recent works have shown that the interaction between the flow of ferrofluids and external magnetic fields can also be applied to control the oscillatory motion of bubbles (Malvar et al., 2018) and heat flux in microfluidic devices (Gontijo, 2018).

1.2 Emulsions and droplet microhydrodynamic

An emulsion is a biphasic mixture of two immiscible viscous liquids in which one is dispersed in the other as droplets. Generally, emulsions are produced by successive droplets rupture processes in a pair of fluids, defining the dispersed phase (droplets) and the continuous phase (based fluid). The addition of surfactants to the mixture aims to avoid the droplets coalescence keeping the emulsion stable. Emulsions are usually composed of Newtonian fluids, however this mixture macroscopically behaves as a single non-Newtonian fluid. The rheological properties of this equivalent fluid are determined by the drop to drop and drop to base fluid interactions, in other words, the flow behavior at the droplets scale. These interactions manly depend on the fluids viscosity ratio (Taylor, 1932; Oliveira & Cunha, 2011, 2015), interfacial tension (Schowalter et al., 1968), droplets average size and geometry (Jeffery, 1922; Batchelor, 1970), and surfactant distribution over the fluids interface (Vlahovska et al., 2002). The very first work to correlate the effective viscosity of a diluted suspension to the flow around a single particle was made by Einstein (1906). Thenceforth experimental, analytical and numerical studies have been done on the rheological behavior of the many different types of suspension, being emulsions among them.

Different sectors of the industry deal with emulsions. The petroleum industry frequently works with it, from the extraction to the transport of water and oil in pipes and ducts (Edwards et al., 1991; Sjöblom, 1992). Recently, the injection of emulsions in petroleum reservoir has been used in order to achieve a more efficient sweep (Alvarado & Manrique, 2010). Moreover, mayonnaise, creams and ointments are well known emulsified products found in food, cosmetics and pharmacy industries, respectively. Studies on the mechanics of the blood microcirculation and drug transport through it are also

closely related to the microhydrodynamics of drops and vesicles (i.e. liquid enclosed by a membrane like drug capsules and red blood cells). Finally, engineers have been expanding the use of emulsions, for the last three decades, to the enhancement of heat transfer and storage processes in the industry, such as the use of phase change materials to store more heat per volume unit of fluid.

1.3   Ferrofluid droplets and magnetic emulsions

A natural next step considering both of the mentioned research lines is to consider two-phase systems in which small droplets of a ferrofluid are dispersed in an immiscible, non-magnetic carrier liquid, defining what is usually called magnetic emulsion. As a matter of fact, ferrofluid droplets and magnetic emulsions are promising fluid-phase materials for different cutting edge applications. Droplets of ferrofluid have been extensively used as pumps, valves, and mixers in microfluidic devices for the development of lab-on-a-chip technologies (Hatch et al., 2001; Hartshorne et al., 2004; Oh et al., 2007). In these cases, the droplet motion inside microchannels is induced and controlled by adjustable external magnetic fields. Ferrofluid droplets have also been considered for biomedical purposes in retinal detachment treatment (Dailey et al., 1999; Voltairas et al., 2001; Mefford et al., 2007). Typical treatment methods consider the injection of a gas bubble into the eye to seal a tear in the retina. However, the patients need to keep their heads in a particular position for almost two weeks, making this kind of treatment very uncomfortable. As a potential alternative, a ferrofluid droplet could be injected into the eye and held in the right place by the action of an external magnetized scleral buckle. In the oil and petroleum industries, magnetic nanoparticles are used to separate immiscible oil and water mixtures through the so-called magnetic separation (Cunha & Sobral, 2004; Sobral & Cunha, 2005).

Suspensions of ferrofluid droplets arise as a new class of complex fluid with a broad range of potential applications. The improvement of already existing techniques and development of new methods rely on fundamental understanding the behavior of ferrofluid droplets under the combined action of a flow field coupled with an applied external magnetic field. However, because of the high complexity intrinsic to ferrofluids and the relatively recent interest in ferrofluid droplets, the physics fundamentals behind

the flow of droplets of a ferrofluid under the action of external magnetic fields are not well understood by researchers in the area.

1.4 Objectives

This work aims to perform a numerical study on the influence of an external magnetic field on the mechanical behavior of magnetic droplets in steady simple shear flows. More specifically, this work intends to:

1. Report an updated bibliographic review on emulsions rheology and microhydrodynamics of magnetic droplets under an applied magnetic field, including theoretical, experimental and numerical works and methods available in the literature;

2. Present a mathematical modeling of the physics of the problem, from the Maxwell equations to the inclusion of magnetic forces on the Navier-Stokes equation. Considerations on the electrical field and magnetic field time dependence are given in such a way that both can be neglected;

3. Describe a numerical formulation based on the Projection Method, Finite Differences and Level-Set to solve the considered Maxwell's equations and Navier-Stokes equation for an incompressible flow considering the magnetic forces;

4. Validate the developed model, comparing the obtained results to the experimental and numerical ones published in the literature, for a magnetic droplet shape under a uniform magnetic field and the rheology of a two-dimensional non-magnetic drop in a simple shear flow;

5. Study the influence of the external magnetic field on the droplet inclination in a shear flow as well as its influence of the bulk rheology, looking at physical explanations for every result obtained;

6. Present discussions on the influence of external magnetic fields on droplets rupture.

1.5 Literature background

The study on the mechanical behavior of suspension started with Stokes (1851) obtaining the terminal velocity U_{st} for a settling/falling hard spherical particle in a continuous viscous medium considering the Stokes' regime, in which the viscous effects are much higher than the inertial ones. Hadamard (1911) and Rybczynski (1911), independently and almost simultaneously, expanded this study for the terminal velocity of a viscous droplet, resulting in the formula known as Hadamard-Rybczynski equation. According to this equation, the terminal velocity of a viscous drop with the viscosity ratio between the drop and the external liquid going to the infinity tends to the rigid sphere terminal velocity (Stokes, 1851) but, always faster. However, this equation was not confirmed by experimental works (Lebedev, 1916; Silvey, 1916; Bond, 1927). Actually, for the vast majority of combinations of fluids and considering clean drops, the terminal velocity matches the Stokes' result, as verified by Silvey (1916) for mercury droplets in xylol. Finally, Bond & Newton (1928) verified, experimentally and theoretically, that the surface tension on drops and bubbles decreases the terminal velocity, varying from the Stokes to the Hadamard-Rybczynski results as this tension decreases. Latter experimental results from Griffith (1962) confirmed this relation. Thereafter, many numerical, experimental and theoretical works have been done on settling velocity of droplets, investigating the influence of surfactants and interactions with other bodies (Davis & Acrivos, 1966; Ishii & Zuber, 1979; Sadhal & Johnson, 1983; Ervik & Bjørklund, 2017; Mandal & Chakraborty, 2017a,b; Ghatage et al., 2017), even the application of magnetic fields on ferrofluid drops was investigated (Afkhami et al., 2008; Shi et al., 2014b,a).

The very first work to estimate the effective viscosity of a diluted suspension was Einstein (1906). In this work, the overall viscosity of a homogeneous suspension of hard spheres, neglecting Brownian motions (Peclet number much higher than the unit) and assuming the creeping motion, is obtained by the viscous dissipation of the flow around a single particle. He concluded that the suspension effective viscosity η is given by the relation $\eta = \eta_0(1 + \phi)$, which was corrected to $\eta = \eta_0(1 + 2.5\phi)$ by himself five years later (Einstein, 1911). Here, η_0 is the ambient Newtonian fluid viscosity and ϕ is the particles volume fraction. This result is only valid for very dilute suspensions, i.e. less than 5%, thus

the interaction between neighbor particles can be safely neglected. Some modifications on the work of Einstein (1911) were necessary to be done to extend the results for the case of flattened or elongated particles. The theory to consider such systems was developed by Jeffery (1922) calculating the motion of ellipsoidal particles in a viscous fluid and their effects on the effective viscosity. Another extension on Einstein's work was done by Taylor (1932) for the case of spherical drops with high surface tension, recovering Einstein's relation for very high viscosity ratios between the droplet and the outer liquids.

Taylor (1934) was the first work to explore how do drops deform in extensional and shear flows, using an ingenious apparatus to conduct experiments. In this work, Taylor defined a scalar measurement of deformation for drops with ellipsoidal geometry. After that, many other works considering small deviations from the the spherical geometry were done. Schowalter et al. (1968) considered a first order correction on the droplet deformation, capturing non-linear effects with stress jumps at the interface. Cox (1969) and Barthés-Biesel & Acrivos (1973) both did theoretical investigations on drops deformation accounting for fluid viscosity and interfacial tension effects. While the first did the study for shear and hyperbolic flows, the second only cared about the first case, however the authors found good predictions for the drop breakup condition. Taylor's classical theory for small drop deformations in Stokes' flows were experimentally recovery by Torza et al. (1972), suggesting the possibility of determining the interfacial tension of viscous drops through the analysis of the wobble and subsequent oscillations of the drop shape in a laminar flow. This work also presents the phenomenon of drops breakup and consequent formations of satellite droplets, i.e. small droplets originated in between two big drops in the droplet breakup process. In this line, Hakimi & Schowalter (1980) and Bentley & Leal (1986) also conducted experimental works on droplets dynamics in shear flows. Advances on computing process and numerical methods, such as the Boundary Integral Method, allowed deeper studies on the mechanical behavior of fluids interfaces. Cristini et al. (1998) was the first work using the Boundary Integral Method to simulate the rupture of viscous drops, being followed by many others (Cristini et al., 2001; Bazhlekov et al., 2004; Dimitrakopoulos, 2007).

External force fields, such as electric and magnetic fields, were found to have a strong effect on drop dynamics and emulsion rheology. A pioneering work in this area was presented by Allan & Mason (1962), who showed by theory and experiments that

uniform electric fields change both droplet shape and inclination angle in simple shear flows. Similar results were more recently found by Mahlmann & Papageorgiou (2009) using numerical simulations. Numerical simulations have also been used to study the effect of electric fields on the shear rheology of concentrated emulsions Fernández (2008a,b, 2009). Vlahovska (2011) presented a small-deformation perturbation analysis to study the shear rheology of dilute emulsions under uniform electric fields at the limits of small capillary number and large viscosity ratio. Notably, the results show that the external field changes not only the emulsion's effective viscosity, but also induces differences in the normal stresses. More recently, Mandal & Chakraborty (2017a,b) extended Vlahovska's theory to account for the effects of charge convection and arbitrarily oriented external electrical fields.

Sherwood (1988) and Sero-Guillaume et al. (1992) presented the first results about the effects of external magnetic fields on magnetic liquid drops suspended in another fluid. These pioneering works mainly focused on the equilibrium shape and rupture dynamics of initially static drops. Field-induced surface instability and deformation of ferrofluid droplets were considered by Flament et al. (1996) to develop different methods to calculate the surface tension between liquids. Backholm et al. (2017) extended that method and proposed a new microrheology technique based on the field-induced oscillatory motion of a ferrofluid droplet. In their method, high-speed cameras are used to analyze the frequency of the droplet oscillations, and the results can be used to well estimate the viscosity of each phase and surface tension between them. Several other researchers have addressed the equilibrium shape, deformation dynamics and field-induced motion of hydrostatic ferrofluid drops under the action of external fields Banerjee et al. (1999); Bashtovoi et al. (1999); Afkhami et al. (2008, 2010); Rowghanian et al. (2016). Shi et al. (2014b,a) studied both numerically and experimentally the problem of a ferrofluid droplet falling in a non-magnetic immiscible liquid under the action of an external, vertical magnetic field. In addition to that, it is worth mentioning that, in the case of concentrated magnetic emulsions, external magnetic fields lead to field-induced structures that might have strong effects on the resulting flow behavior of the liquid Liu et al. (1995); Flores et al. (1999); Scherer (2005); Zakinyan & Dikansky (2011).

Most of the works discussed so far have considered the interaction of ferrofluid droplets and external magnetic fields in static situations, that is, in the absence of a

background hydrodynamic flow. Drop dynamics and its effects on emulsion rheology in the combined presence of magnetic field and fluid flow is an even more challenging case and, to the best of our knowledge, it is less explored in the related literature.

1.6 Scope of the work

This work is organized as follows. In chapter 2, the complete mathematical formulation of the problem is presented, including details on the considered magnetostatic limit of the Maxwell equations, the deduction of the movement equations for interfaces, the formulation of the Level-Set method and how these three concepts are coupled together to describe the discontinuous problem of a multiphase flow interacting with a magnetic field in an elegant continuum model. Then, chapter 3 is devoted to describe the numerical methodology used in this research, considering technical aspects of the Finite Differece Method, Projection Method and Level-Set Method. In chapter 4, the mathematical and numerical methodologies developed in this work are validated by comparisons with benchmark problems available in the literature. In 5 we present and discuss all the results produced during this research, in order to well understand the physics of the problem. Finally, chapter 6 contains a brief conclusion and some suggestions for future works.

2 Mathematical formulation

This chapter is devoted to the mathematical formulation of the physics behind a magnetic droplet under the influence of a shear flow and an external magnetic field. First, the problem statement is detailed, defining all the relevant aspects and variables involved. Then, the Maxwell equations are exposed and explained, followed by the fluid magnetization and electromagnetism considerations used in this work, culminating in the so-called magnetostatic limit. Under this limit the magnetic field becomes irrotational, allowing the problem to be described by a magnetic potential field. The conservation of mass and momentum equations are used together with the hydrodynamics stress tensor, magnetic forces and capillary forces, in order to obtain the movement equations governing the two-phase flow coupled with magnetic and capillary forces. A brief discussion about drops contributions to the viscosity of diluted emulsions and how to measure this contribution is presented. Then, the Level-Set method used to capture the fluids interface as well as to compute the geometrical properties is carefully explained, followed by a summary of the equations to be solved in the problem. Finally, a list of the considered boundary conditions is presented.

2.1 Problem statement

The problem under study consists in a neutrally buoyant planar ferrofluid droplet of radius a, viscosity $\lambda\eta$, density ρ and magnetic permeability $\zeta\mu_0$, suspended in a non-magnetizable liquid with viscosity η, density ρ and magnetic permeability μ_0, which is assumed to be equal to the magnetic permeability of the free space ($\mu_0 = 4\pi \times 10^{-7}$ H·m^{-1}). Both phases are Newtonian and all properties are kept as constant for each phase. The resulting biphasic system is confined in a gap H_p between two parallel plates of length L_p. This two-dimensional domain is periodically repeated, containing a single drop in each periodic cell. The movement of the plates' in opposite directions with velocity U_p causes a shear on the system. An external uniform magnetic field $\boldsymbol{H}_0$ is applied either parallel or perpendicular to the plates. A sketch of the problem is shown in Fig. 1. The

plates velocity is such that $U_p = \dot{\gamma}/2H_p$, being $\dot{\gamma}$ the shear rate.
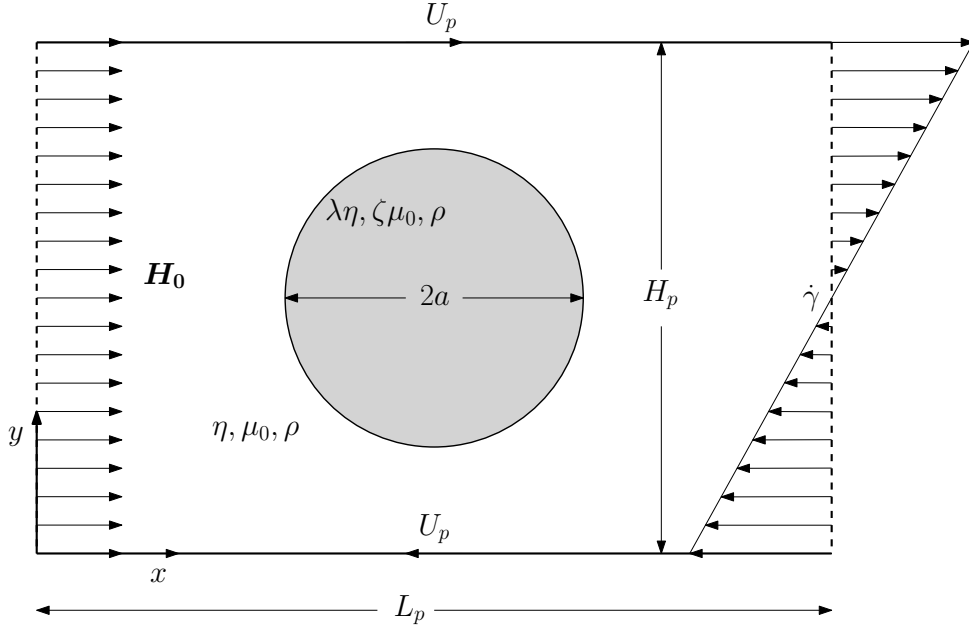
Figure 1 – Sketch of the problem (not to scale).

In the following, a formulation coupling the two-phase fluid flow problem with the applied external magnetic field is presented. Notice that the viscosity and magnetic permeability change from η and μ_0 in the outer fluid to $\lambda\eta$ and $\zeta\mu_0$ in the inner fluid.

2.2 Maxwell equations

The electromagnetism is governed by four laws: Gauss's law, Gauss's law for the magnetism, Faraday's law and Ampère-Maxwell law. Together, they compose the set of partial differential equations known as Maxwell equations (Jackson, 1999). The Gauss's law states that the flux of electrical field leaving a closed surface is proportional to the amount of charge enclosed by it, in the sense that this flux can neither be lost or created in the space. In the differential form, this law is mathematically written as

$$\nabla \cdot \boldsymbol{E} = \frac{\rho_c}{\epsilon_0}, \tag{2.1}$$

where ∇ denotes the nabla operator, $\boldsymbol{E}$ is the electric field, ρ_c the electric charge density and ϵ_0 the dielectric constant. The Gauss's law for the magnetism is similar to the last one, but for the magnetic induction field, $\boldsymbol{B}$. As a direct consequence of the nonexistence of magnetic monopoles, the flux of magnetic field through the surface is null, and so on

$\boldsymbol{B}$ obeys the continuity equation,

$$\nabla \cdot \boldsymbol{B} = 0. \tag{2.2}$$

The magnetic induction is defined as $\boldsymbol{B} = \mu_0(\boldsymbol{H} + \boldsymbol{M})$, being $\boldsymbol{H}$ the magnetic field and $\boldsymbol{M}$ the local magnetization. The last one refers to the state of polarization of the matter, which is the local average of the magnetic moments of individual nanoparticles and can be externally induced by magnetic fields. The Faraday's law of induction relates variations on the magnetic fields with electric fields. Faraday conducted many experiments on this subject and developed various technologies using this phenomenon, but this law got only mathematically expressed by Maxwell (Stewart, 2012),

$$\nabla \times \boldsymbol{E} = -\frac{\partial \boldsymbol{B}}{\partial t}. \tag{2.3}$$

Lastly, the Ampère-Maxwell law. Similar to the Faraday's law, it expresses that a magnetic field may be induced either by an electric current density $\boldsymbol{J}$ or a variation of the electric field in time.

$$\nabla \times \boldsymbol{H} = \boldsymbol{J} + \epsilon_0\frac{\partial \boldsymbol{E}}{\partial t}. \tag{2.4}$$

2.3 Ferrofluid magnetization and magnetostatic regime

In the absence of magnetic fields, the magnetic dipoles of the ferrofluids are kept randomly oriented by the Brownian movements, thus the material presents no magnetization. However, once a magnetic field is applied, the dipoles dispersed in the fluid tend to get aligned with this field, causing the magnetization of the fluid. This effect is illustrated in Fig. 2.

The stronger the magnetic field, more aligned the dipoles, reflecting in a greater magnetization, $\boldsymbol{M}$, of the suspension. Naturally, this magnetization reaches a saturation once all dipoles are perfectly aligned to the magnetic field. After a certain effort, see Rosensweig (1997), it is possible to demonstrate that the magnetization is described by

$$\frac{M}{\beta_m M_d} = coth(\alpha) - \frac{1}{\alpha} \equiv L(\alpha), \tag{2.5}$$

$$\alpha = \frac{\pi}{6}\frac{\mu_0 M_d H d^3}{kT}, \tag{2.6}$$
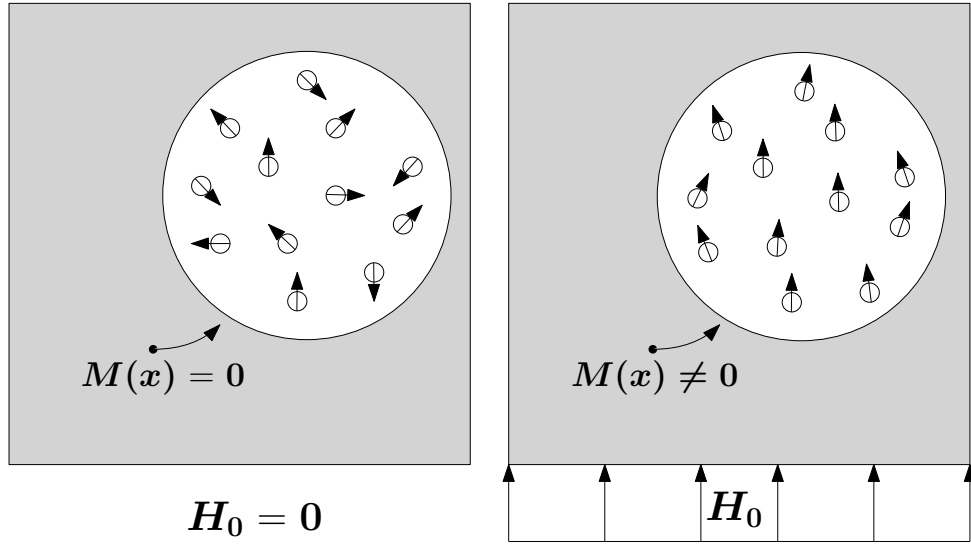
Figure 2 – Dipoles alignment under the influence of an external magnetic field, $\boldsymbol{H}_0$, in a ferrofluid, resulting in the material magnetization, $\boldsymbol{M}$.

where $M = |\boldsymbol{M}|$, β_m is the volume fraction of magnetic particles, M_d is the magnetization of the magnetic particles material, $L(\alpha)$ is the Langevin function, d is the particles diameter, k is the Boltzmann's constant and T is the absolute temperature (Rosensweig, 1987). The typical Langevin function curve is presented in Fig. 3. Notice that the Langevin function is *quasi*-linear for $\alpha \leq 1$. This is the regime of magnetization used in this work, therefore we can state that $M \propto H$.
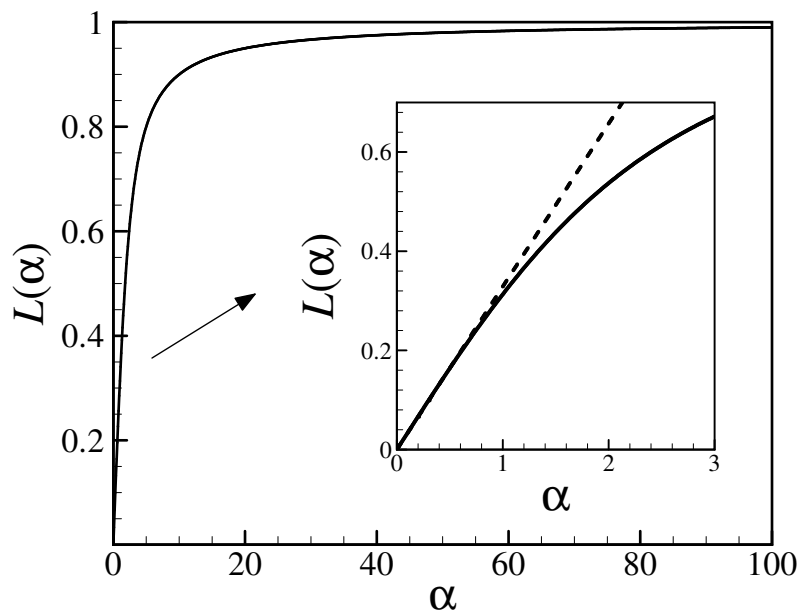
Figure 3 – Langevin function curve.

There are two mechanisms through which a colloidal ferrofluid relax after a change on the applied field. For the first, the magnetic particles rotate inside the ambient fluid aligning its magnetic moment with the applied field, and it is characterized by the Brownian rotational diffusion time τ_B. The second mechanism is based on the magnetic moment direction changing inside the magnetic particles, not related with hydrodynamics phenomena, and it is known as Néel mechanism, with characteristic time τ_N (Shliomis, 1974). In a flow, the vorticity rotates the magnetic dipoles inside the fluid causing a misalignment between $\boldsymbol{M}$ and $\boldsymbol{H}$ and, consequently, body torque of density $\mu_0 \boldsymbol{M} \times \boldsymbol{H}$, increasing the effective viscosity (Shliomis, 1971; Henjes, 1995; Shliomis, 2001). However, this phenomenon may be neglected depending on the relation between the characteristic flow time τ_F and the two others just mentioned above. If $\tau_B \ll \tau_F$ or $\tau_N \ll \tau_F$, the dipoles will always be collinear with the magnetic field and there will be no body torques (Rosensweig, 1987), which is the hypothesis considered in this work, i.e. misalignment between $\boldsymbol{M}$ and $\boldsymbol{H}$ are neglected.

In the two last paragraphs, we have explored the two considerations used in this work related to the ferrofluid magnetization. The magnetization intensity is a linear function of the local magnetic field and the magnetization vector is pointing in the very same direction of the magnetic field. Therefore, the magnetization vector obeys a linear relation to the magnetic vector field, such that $\boldsymbol{M} = \chi(\boldsymbol{x})\boldsymbol{H}$, where $\chi(\boldsymbol{x})$ is the local magnetic susceptibility. Consequently, $\boldsymbol{B} = \mu_0(\chi + 1)\boldsymbol{H}$. Defining $\mu = \mu_0(1 + \chi)$ as the material magnetic permeability, we have that

$$\boldsymbol{B} = \mu(\boldsymbol{x})\boldsymbol{H}. \tag{2.7}$$

Notice that in the vacuum $\chi = 0$ and $\mu = \mu_0$. Other important relation is given by the ratio between the local magnetic permeability and the vacuum magnetic permeability, $\zeta(\boldsymbol{x}) = \mu(\boldsymbol{x})/\mu_0$, called relative permeability.

In the absence of electrical fields and electric currents flux, as it is observed in the problem under study, the Maxwell's equations are reduced to the so-called magnetostatic regime, given by

$$\nabla \cdot \boldsymbol{B} = 0 \tag{2.8}$$

and

$$\nabla \times \boldsymbol{H} = \boldsymbol{0}. \tag{2.9}$$

Such equations characterize, respectively, the continuity of the magnetic induction in the normal direction and the continuity of the magnetic field in the tangential direction through a boundary (Jackson, 1999). Being $\boldsymbol{H}$ an irrotational field, it can be expressed as the gradient of a potential field, naturally called magnetic potential field, ψ, such that $\boldsymbol{H} = -\nabla\psi$. Therefore, Eqs. (2.8) and (2.9) can be combined to give

$$\nabla \cdot \left(\zeta(\boldsymbol{x})\nabla\psi \right) = 0. \tag{2.10}$$

Equation (2.10) gives the magnetic potential field all over the domain. Once $\zeta(\boldsymbol{x})$ is not constant in the domain, it cannot be taken out of the divergence operator.

2.4   Motion equations in view of interfaces

In the perspective of continuum mechanics, the motion is governed by the conservation equations of mass and momentum. Consider a volume of fluid occupying a region Ω, in space, bounded by $\partial\Omega$. This volume moves and deforms in time, but it is always composed by the very same particles. We assume that the fluids interface, Γ, intersects the region Ω, dividing it in two sub-regions, Ω_1 and Ω_2 respectively bounded by $\partial\Omega_1$ and $\partial\Omega_2$. The normal vector over $\partial\Omega$ points outward Ω and over Γ it points outward Ω_1. The two sub-regions are related to each fluid considered in the problem. Figure 4 presents the volume just described. Under these considerations, we have that $\Gamma = \partial\Omega_1 \cap \partial\Omega_2$, $\Omega = \Omega_1 \cup \Omega_2$ and $\partial\Omega = \partial\Omega_1 \cup \partial\Omega_2 - \Gamma$.

The total mass, m_V, of the Ω is computed by

$$m_V = \int_\Omega \rho \, dv. \tag{2.11}$$

Since this volume is always composed by the same particles, its mass must not vary in time. Therefore, using the Reynolds transport theorem, we get that

$$\frac{dm_V}{dt} = \frac{d}{dt}\int_\Omega \rho \, dv = \int_\Omega \left[\frac{\partial\rho}{\partial t} + \nabla \cdot (\rho\boldsymbol{u}) \right] d\Omega = 0. \tag{2.12}$$

By using the location theorem in Eq. 2.12, we obtain the mass conservation equation,

$$\frac{\partial\rho}{\partial t} + \nabla \cdot (\rho\boldsymbol{u}) = 0. \tag{2.13}$$
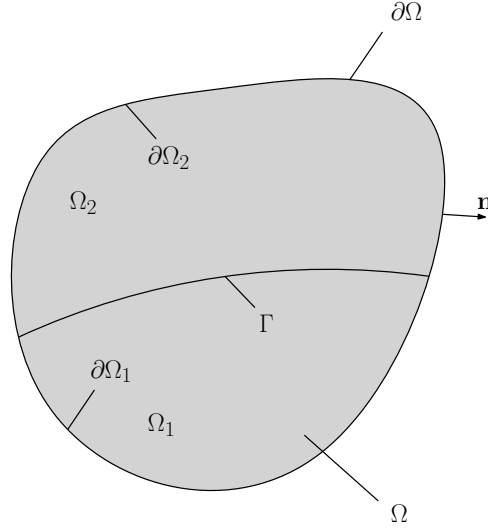
Figure 4 – Volume of study, Ω, containing the fluids interface, Γ.

Note that, despite the fact that the volume is intersected by the fluids interface, it does not modify the traditional demonstration of the mass conservation equation. However, this is not true for the momentum conservation equation. The momentum, $\boldsymbol{q}_V$, of the volume of fluid Ω, is given by

$$\boldsymbol{q}_V = \int_\Omega \rho \boldsymbol{u} \, dv. \tag{2.14}$$

Using the Reynolds transport theorem together with the mass conservation equation, we get that momentum time variation is given by

$$\frac{d\boldsymbol{q}_V}{dt} = \frac{d}{dt} \int_\Omega \rho \boldsymbol{u} \, dv = \int_\Omega \left[\frac{\partial(\rho \boldsymbol{u})}{\partial t} + \nabla \cdot (\rho \boldsymbol{u} \boldsymbol{u}) \right] d\Omega = \int_\Omega \rho \frac{D\boldsymbol{u}}{Dt} \, d\Omega, \tag{2.15}$$

where the operator $D(\ )/Dt = \partial(\ )/\partial t + \boldsymbol{u} \cdot \nabla(\ )$ is the material derivative. According to Newton's second law, the momentum time variation of a system is in balance with the external forces acting on this system. Thus,

$$\int_\Omega \rho \frac{D\boldsymbol{u}}{Dt} \, d\Omega = \int_\Omega \boldsymbol{f} \, d\Omega + \int_{\partial\Omega} \boldsymbol{\sigma} \cdot \boldsymbol{n} \, ds, \tag{2.16}$$

where $\boldsymbol{f}$ contemplates field forces volume density of any nature and $\boldsymbol{\sigma}$ is the Cauchy stress tensor. Now, decomposing the boundary integral over $\partial\Omega$, we obtain

$$\int_\Omega \rho \frac{D\boldsymbol{u}}{Dt} \, d\Omega = \int_\Omega \boldsymbol{f} \, d\Omega + \int_{\partial\Omega_1} \boldsymbol{n} \cdot \boldsymbol{\sigma} \, ds + \int_{\partial\Omega_2} \boldsymbol{n} \cdot \boldsymbol{\sigma} \, ds + \int_\Gamma [[\boldsymbol{n} \cdot \boldsymbol{\sigma}]] \, ds, \tag{2.17}$$

where $[[\boldsymbol{\sigma} \cdot \boldsymbol{n}]]$ is the stress jump in the normal direction across the fluids interface. The last integral in the right-hand side of Eq. 2.17 refers to the stress discontinuity in between the two surfaces $\partial\Omega_1$ and $\partial\Omega_2$. For the two first surface integrals, we have from the Stokes

theorem that

$$\int_{\partial\Omega_1} \boldsymbol{n} \cdot \boldsymbol{\sigma}\, ds = \int_{\Omega_1} \nabla \cdot \boldsymbol{\sigma}\, d\Omega \tag{2.18}$$

and

$$\int_{\partial\Omega_2} \boldsymbol{n} \cdot \boldsymbol{\sigma}\, ds = \int_{\Omega_2} \nabla \cdot \boldsymbol{\sigma}\, d\Omega. \tag{2.19}$$

Here, the stress jump across the fluids interface is given according the well-known Young-Laplace equation neglecting surfactants concentration gradient over the interface, defined as

$$[[\boldsymbol{\sigma} \cdot \boldsymbol{n}]] = -\kappa\sigma\boldsymbol{n}, \tag{2.20}$$

being κ the local mean curvature given by $\nabla \cdot \boldsymbol{n}$ and σ the interfacial tension between the phases. Thereafter,

$$\int_\Gamma [[\boldsymbol{\sigma} \cdot \boldsymbol{n}]]\, ds = -\int_\Gamma \kappa\sigma\boldsymbol{n}\, ds = -\int_\Omega \int_\Gamma \kappa\sigma\boldsymbol{n}\delta(\boldsymbol{x} - \boldsymbol{x}_\Gamma(t))\, ds\, d\Omega, \tag{2.21}$$

being $\delta(\boldsymbol{x} - \boldsymbol{x}_\Gamma(t))$ the Dirac delta distribution in the same dimension of Ω and $\boldsymbol{x}_\Gamma(t)$ the position of the fluids interface. Substituting Eqs. 2.18, 2.19 and 2.21 in Eq. 2.17 and using the location theorem, we obtain the momentum balance equation for the flow of fluids in presence of interfaces (Unverdi & Tryggvason, 1992)

$$\rho\frac{D\boldsymbol{u}}{Dt} = \boldsymbol{f} + \nabla \cdot \boldsymbol{\sigma} - \int_\Gamma \kappa\sigma\boldsymbol{n}\delta(\boldsymbol{x} - \boldsymbol{x}_\Gamma(t))\, ds. \tag{2.22}$$

According to Chang et al. (1996), since s is a purely Lagrangian variable, the arclength metric $|\boldsymbol{x}_s|$ must be taken in account in the singular source term of Eq. 2.22. Thus

$$\rho\frac{D\boldsymbol{u}}{Dt} = \boldsymbol{f} + \nabla \cdot \boldsymbol{\sigma} - \int_\Gamma \kappa\sigma\boldsymbol{n}\delta(\boldsymbol{x} - \boldsymbol{x}_\Gamma(t))|\boldsymbol{x}_s|\, ds. \tag{2.23}$$

2.5   Motion equations for a magnetic droplet

In the present study, the flow of both fluids are incompressible, therefore ρ is constant in time and space, and Eq. 2.13 may be rewritten as

$$\nabla \cdot \boldsymbol{u} = 0. \tag{2.24}$$

Both fluids display Newtonian behaviors, thus the stress tensor of each phase is symmetric and described by

$$\boldsymbol{\sigma} = \boldsymbol{\sigma}^T = -p_h\boldsymbol{I} + \lambda(\boldsymbol{x})\eta(\nabla\boldsymbol{u} + \nabla\boldsymbol{u}^T) \tag{2.25}$$

where p_h is the hydrodynamic pressure. Finally, the droplet being neutrally buoyant and the fluids densities constant, the magnetic field force, $\boldsymbol{f}_m$, is the only field force considered in the problem.

$$\boldsymbol{f}_m = \mu_0 \boldsymbol{M} \cdot \nabla \boldsymbol{H} = \mu_0 (\zeta(\boldsymbol{x}) - 1) \boldsymbol{H} \cdot \nabla \boldsymbol{H}. \tag{2.26}$$

Using Eqs. (2.25) and (2.26) into Eq. (2.23), the momentum conservation becomes

$$\rho \frac{D\boldsymbol{u}}{Dt} = -\nabla p_h + \nabla \cdot \left[\lambda(\boldsymbol{x}) \eta \left(\nabla \boldsymbol{u} + \nabla \boldsymbol{u}^T \right) \right] + \mu_0 (\zeta(\boldsymbol{x}) - 1) \boldsymbol{H} \cdot \nabla \boldsymbol{H} - \int_\Gamma \kappa \sigma \boldsymbol{n} \delta(\boldsymbol{x} - \boldsymbol{x}_\Gamma(t)) |\boldsymbol{x}_s| \, ds. \tag{2.27}$$

The non-dimensionalization of Eqs. (2.24) and (2.27) proceeds with the following dimensionless variables: $\boldsymbol{u}^* = \boldsymbol{u}/\dot{\gamma}a$; $t^* = t\dot{\gamma}$, $\boldsymbol{x}^* = \boldsymbol{x}/a$; $p_h^* = p_h/\rho a^2 \dot{\gamma}^2$; $\boldsymbol{H}^* = \boldsymbol{H}/|\boldsymbol{H}_0|$; $\kappa^* = a\kappa$; $\delta^* ds^* = a\delta ds$; and $\nabla^* = a\nabla$. Hereafter, all variables are dimensionless and, for convenience, the superscript * is not used anymore. Equation (2.24) remains the same in its dimensionless form. In turn, Eq. (2.27) yields

$$\begin{aligned}
\frac{D\boldsymbol{u}}{Dt} &= -\nabla p_h + \frac{1}{Re} \nabla \cdot \left[\lambda(\boldsymbol{x}) \left(\nabla \boldsymbol{u} + \nabla \boldsymbol{u}^T \right) \right] \\
&+ \frac{Ca_{mag}}{Ca\,Re} (\zeta(\boldsymbol{x}) - 1) \boldsymbol{H} \cdot \nabla \boldsymbol{H} \\
&- \frac{1}{Ca\,Re} \int_\Gamma \kappa \boldsymbol{n} \delta(\boldsymbol{x} - \boldsymbol{x}_\Gamma(t)) |\boldsymbol{x}_s| \, ds,
\end{aligned} \tag{2.28}$$

where

$$Re = \rho \dot{\gamma} a^2 / \eta \tag{2.29}$$

is the Reynolds number corresponding to the ratio between inertial and viscous forces,

$$Ca_{mag} = \mu_0 a |\boldsymbol{H}_0|^2 / \sigma \tag{2.30}$$

is the magnetic capillary number corresponding to the ratio between magnetic and capillary forces (Cunha & Couto, 2008), and

$$Ca = \eta a \dot{\gamma} / \sigma \tag{2.31}$$

is the capillary number corresponding to the ratio between viscous and capillary forces. These three dimensionless groups together with the viscosity ratio between the phases, λ, and the magnetic permeability ratio between the phases, ζ, are the main parameters of the model. Notice that σ is a constant all over the fluids interface.

2.6   Emulsions viscosity

An emulsion may be treated as a single phase system once the flow length scale under study is much larger compared to the average droplets size. The suspension being diluted enough, such that the flow disturbance caused by a particle is not observed by the others, the particles contributions to the bulk stress become independent. Thus, the suspension viscosity is linearly related to the dispersed to continuous phases volume fraction, β_v. This assumption is convenient for $\beta_v \leq 5\%$. Once the viscosity of an emulsion depends on the mechanical behavior of the drops at the micro scale and not only on the properties of the fluids, becomes convenient to denominate it as effective viscosity.

In this work, the influence of a single drop on the effective viscosity, η_{eff}, of the biphasic mixture confined between the two plates is computed by measuring the average shear stress on the plates $\langle \sigma_{xy} \rangle$. We have that $\eta_{eff} = \langle \sigma_{xy} \rangle / \dot{\gamma}$, while

$$\langle \sigma_{xy} \rangle = \frac{1}{2L_p} \int_S \eta \frac{du}{dy} dS, \tag{2.32}$$

where S is the combined surfaces of the two plates. In the study of suspensions rheology, it is often used the so-called reduced viscosity $[\eta]$, which is the effective viscosity subtracted by the based fluid viscosity and normalized by $\eta \beta_v$. Therefore,

$$[\eta] = \frac{\langle \sigma_{xy} \rangle - \eta \dot{\gamma}}{\eta \dot{\gamma} \beta_v}. \tag{2.33}$$

2.7   Level-Set method

The Level-Set method was first presented by Osher & Sethian (1988) to compute fronts propagation with curvature-dependent speed, and became a popular method in the computational study of multiphase-flows. Distinct from interface tracking methods, requiring the mesh to have points right at the interface, in the Level-Set method the remeshing during the simulation is not needed. Here, this method is used to capture the fluids interface location and geometry over time. Also, it allows to formulate the two-phase flow problem as a continuum problem.

Consider a region $\Omega(t)$, possibly multiconnected, enclosed by a moving boundary $\Gamma(t)$, representing the fluids interface. We associate to $\Gamma(t)$ a scalar signed distance function called Level-Set, $\phi = \phi(\boldsymbol{x}, t)$, measuring the distance between a point $\boldsymbol{x}$ of the domain

and the closest point belonging to $\Gamma(t)$, $\boldsymbol{x}_\Gamma$, being negative inside the dispersed phase and positive in the continuous phase. A scheme of the Level-Set function is shown in Fig. 5. Notice that the shortest distance vector is always perpendicular to the fluids interface, $(\boldsymbol{x} - \boldsymbol{x}_\Gamma) \perp \Gamma$. Let's proceed with a quick mathematical analysis on the signed distance function. We have that

$$\phi(\boldsymbol{x})^2 = (\boldsymbol{x} - \boldsymbol{x}_\Gamma) \cdot (\boldsymbol{x} - \boldsymbol{x}_\Gamma). \tag{2.34}$$

Taking the gradient in Eq. 2.34,

$$2\phi(\boldsymbol{x})\nabla\phi(\boldsymbol{x}) = 2(\boldsymbol{x} - \boldsymbol{x}_\Gamma) \cdot \boldsymbol{I}, \tag{2.35}$$

thus

$$\nabla\phi(\boldsymbol{x}) = \frac{(\boldsymbol{x} - \boldsymbol{x}_\Gamma)}{\phi(\boldsymbol{x})} = \boldsymbol{n} \tag{2.36}$$

and

$$|\nabla\phi(\boldsymbol{x})| = \frac{|(\boldsymbol{x} - \boldsymbol{x}_\Gamma)|}{\phi(\boldsymbol{x})} = 1. \tag{2.37}$$

Therefore, being the Level-Set function a distance signed function, its gradient gives the interface normal vector and it obeys an Eikonal equation, Eq. 2.37.
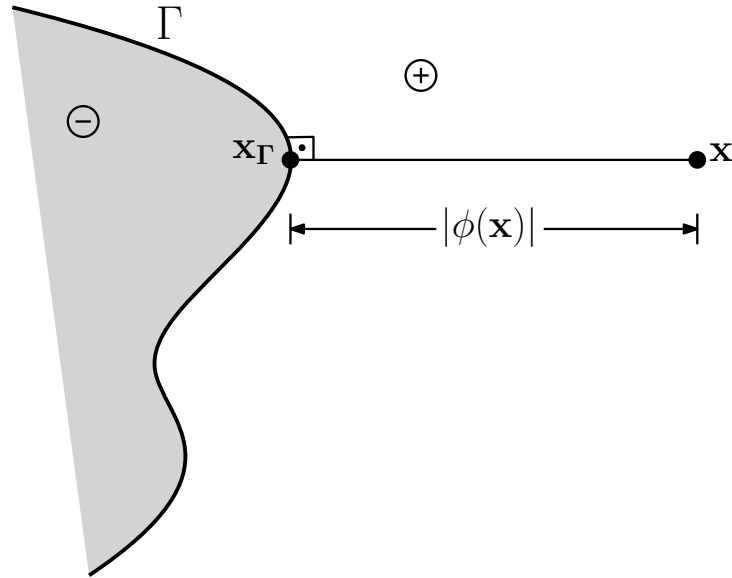
Figure 5 – Representation of the Level-Set function, $\phi(\boldsymbol{x})$.

Naturally, the interface is located where the distance function is null, therefore moving this interface is equivalent to properly updating ϕ. Consider the trajectory of a particle, $\boldsymbol{X}_0 = \boldsymbol{X}(t = 0)$, right at the fluids interface $\Gamma(t)$. Since this particle belongs to the interface, and must always do, $\phi(\boldsymbol{X}(\boldsymbol{X}_0, t), t) = 0$. Differentiating with respect to t,

we get that ϕ obeys a Hamilton-Jacobi type equation,

$$\frac{D\phi}{Dt} = \frac{\partial\phi}{\partial t} + \boldsymbol{u}\cdot\nabla\phi = 0. \tag{2.38}$$

In the problem here presented, we are looking for transformations on the droplet shape, which are only caused by movements on the normal direction. Thus, the velocity, $\boldsymbol{u}$, is projected in the interface normal direction, $\boldsymbol{n}$, and Eq. 2.38 becomes

$$\frac{\partial\phi}{\partial t} + (\boldsymbol{u}\cdot\boldsymbol{n})|\nabla\phi| = 0. \tag{2.39}$$

The solution of Eqs. 2.38 and 2.39 gives the evolution of $\Gamma(t)$ over time and, consequently, the fluids interface propagation. Despite the zero of ϕ keeps representing the position of Γ, this evolution does not guarantee the Level-Set function as the distance signed function of the interface for the all domain. That said, Sussman et al. (1994) proposed a technique to re-initialize the Level-Set function in order to be the signed distance function of Γ once again. This reinitialization is given by the steady state solution of

$$\frac{\partial\phi}{\partial\tau} = \text{sgn}(\phi_0)(1 - |\nabla\phi|), \tag{2.40}$$

where τ is the virtual time, sgn is the sign function and $\phi_0(\boldsymbol{x}) = \phi(\boldsymbol{x}, \tau = 0)$. The solution of ϕ for Eq. 2.40 will have the same sign and zero as ϕ_0, and satisfies $|\nabla\phi| = 1$, so it is the distance signed function of the fluids interface. Despite the necessity of this technique, it causes a disturb on the droplet volume, usually resulting in its degradation. In order to minimize this undesired effect, this technique is not used every time step.

These results present a great advantage of the Level-Set method. The distance function allows the easily computation of geometrical properties on the drop surface, such as the outward unit normal vector, $\boldsymbol{n}$, and curvature, κ, respectively

$$\boldsymbol{n} = \nabla\phi \tag{2.41}$$

and

$$\kappa = \nabla\cdot\boldsymbol{n}. \tag{2.42}$$

Both fluids differ in properties, $\lambda(\boldsymbol{x}) = \lambda(\phi(\boldsymbol{x}))$ and $\zeta(\boldsymbol{x}) = \zeta(\phi(\boldsymbol{x}))$, therefore, an artificial interface is considered for the problem, in which the local properties smoothly

vary from one to the other fluid. This artificial interface is located at $|\phi| \leq \varepsilon$, where ε is one half of the thickness. In order to compute the phases transition, the following Heavyside function is used

$$
H_\varepsilon(\phi) = \begin{cases} 0, & \text{if } \phi < -\varepsilon, \\ \dfrac{1}{2}\left[1 + \dfrac{\phi}{\varepsilon} + \dfrac{1}{\pi}\sin\left(\dfrac{\pi\phi}{\varepsilon}\right)\right], & \text{if } |\phi| \leq \varepsilon, \\ 1, & \text{if } \phi > \varepsilon. \end{cases} \tag{2.43}
$$

Notice that the Heavyside function is zero at the dispersed phase and the unit at the continuous phase, smoothly varying from one to the other in the artificial interface, as shown Fig. 6 for $\varepsilon = 1.5$. This leads to the continuous functions $\lambda_\varepsilon(\phi) = \lambda + (1 - \lambda)H_\varepsilon(\phi)$ and $\zeta_\varepsilon(\phi) = \zeta + (1 - \zeta)H_\varepsilon(\phi)$. Also, H_ε can be used to properly compute volume or area integrals of a quantity $p(\boldsymbol{x}, t)$ over Ω by

$$
\int_\Omega p(\boldsymbol{x}, t) H_\varepsilon(\phi) d\Omega. \tag{2.44}
$$
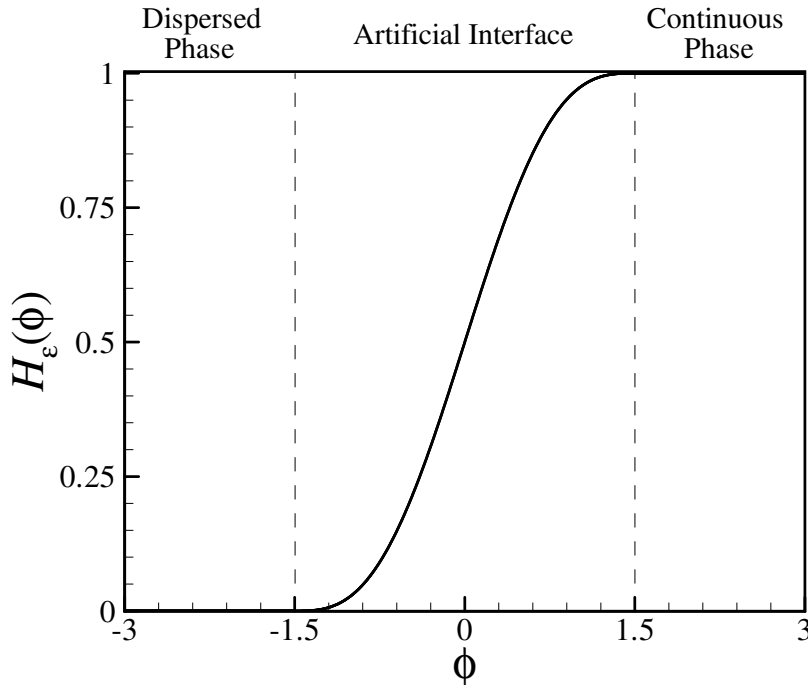
Figure 6 – Heavyside function curve for $\varepsilon = 1.5$.

From the smoothed Heaviside function it is possible to define a smoothed Dirac delta distribution, $\delta_\varepsilon(\phi)$,

$$\delta_\varepsilon(\phi) = \frac{\partial H_\varepsilon(\phi)}{\partial \phi} = \begin{cases} 0, & \text{if } |\phi| > \varepsilon, \\ \dfrac{1}{2\varepsilon}\left[1 + \cos\left(\dfrac{\pi\phi}{\varepsilon}\right)\right], & \text{if } |\phi| \le \varepsilon, \end{cases} \tag{2.45}$$

which curve is shown in Fig. 7 for $\varepsilon = 1.5$.
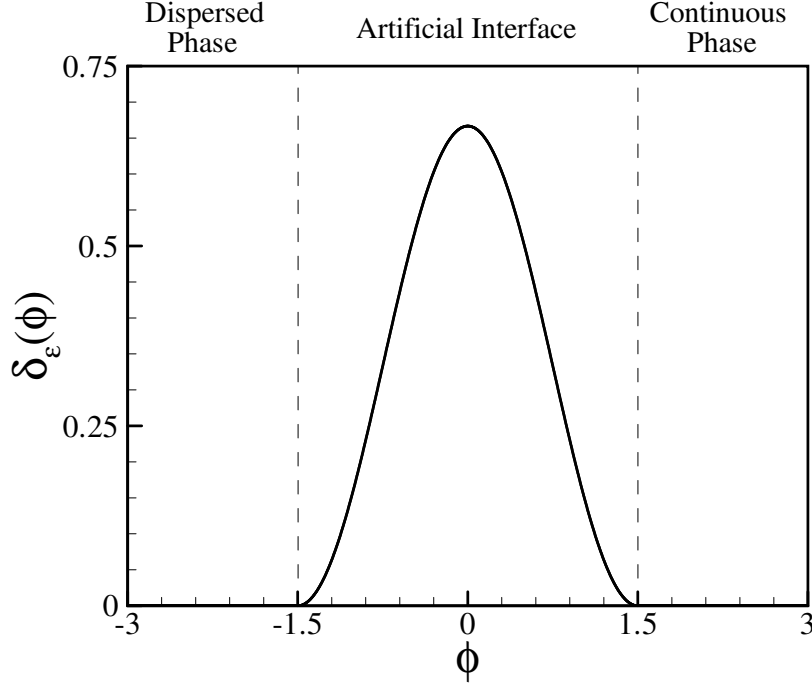
Figure 7 – Smoothed Dirac delta curve for $\varepsilon = 1.5$.

The smoothed Dirac delta equation can be used to properly compute surface or line integrals (depending on the dimension of the problem) of a quantity $p(\boldsymbol{x}, t)$ over Γ by

$$\int_\Gamma p(\boldsymbol{x}, t)\delta_\varepsilon(\phi)|\nabla\phi|d\Gamma. \tag{2.46}$$

Also, according to (Chang et al., 1996; Croce et al., 2010; Salac & Miksis, 2011), the Dirac delta function may be used to rewrite the surface integral of Eq. 2.28 as follows

$$\int_\Gamma \sigma\kappa\boldsymbol{n}\delta(\boldsymbol{x} - \boldsymbol{x}_\Gamma(t))|\boldsymbol{x}_s|\,ds = \sigma\kappa\delta(\phi)\nabla\phi. \tag{2.47}$$

2.8   Coupling the Level-Set method with magnetic and motion equations

The two-phase flow problem under study presents discontinuities due to the differences between the fluids properties, stress jump over the interface and magnetic field

discontinuity due to the droplet magnetization. However, the use of the Level-Set method allows to rewrite this problem as a continuum, by the use of the Heavyside functions, smoothed Dirac's Delta function and the capturing of the interface by the advection of the singed distance function, i.e. the Level-Set function. Thus, the overall problem of the magnetic droplet in a shear flow under the action of an external field can be described, due to the use of the Level-Set method, in continuum formulation as follows:

- The magnetic field couples with the Level-Set by the use of the Heavyside function in the computation of the local magnetic permeability, $\zeta = \zeta(\boldsymbol{x}) = \zeta_\varepsilon(\phi(\boldsymbol{x}))$. This way, this property becomes continuum all over the domain as well the magnetic potential field, and Eq. 2.10 may be rewritten as

$$\nabla \cdot \left(\zeta_\varepsilon(\phi) \nabla \psi \right) = 0. \tag{2.48}$$

- For the motion, the mass conservation equation is the same while the momentum conservation is modified in the computation of the local viscosity ratio, local magnetic permeability and capillary forces. Then, the motion equations may be rewritten in the perspective of the Level-Set method by

$$\nabla \cdot \boldsymbol{u} = 0 \tag{2.49}$$

and

$$\begin{aligned} \frac{D\boldsymbol{u}}{Dt} &= -\nabla p_h + \frac{1}{Re}\nabla \cdot \left[\lambda_\varepsilon(\phi) \left(\nabla \boldsymbol{u} + \nabla \boldsymbol{u}^T \right) \right] \\ &+ \frac{Ca_{mag}}{Ca\,Re}(\zeta_\varepsilon(\phi) - 1)\boldsymbol{H} \cdot \nabla \boldsymbol{H} \\ &- \frac{1}{Ca\,Re}\kappa\delta_\varepsilon(\phi)\nabla\phi. \end{aligned} \tag{2.50}$$

- To capture the fluids interface, it must be done the advection of the Level-Set function by the flow as well its reinitialization in order to keep it as the signed distance function, as presented in section 2.7. Therefore, the last two needed equations to close the set of equations that describe our model as continuum are

$$\frac{\partial \phi}{\partial t} + (\boldsymbol{u} \cdot \boldsymbol{n})|\nabla\phi| = 0 \tag{2.51}$$

and

$$\frac{\partial \phi}{\partial \tau} = \text{sgn}(\phi_0)(1 - |\nabla\phi|). \tag{2.52}$$

2.9 Boundary and initial conditions of the problem

The boundary and initial conditions applied to the problem matches with:

- Droplet initially circular with radius a and located right at the center of the domain;

- Flow initially in rest;

- Neumann boundary conditions for the magnetic potential field recovering the external magnetic field at the boundaries, that is, $\nabla \psi = -\boldsymbol{H}_0$;

- Periodicity of the velocity and pressure field at the sides boundaries;

- Homogeneous Neumann boundary condition for p_h at the top and bottom boundaries;

- At the top and bottom boundaries, the non-homogeneous Dirichlet boundary condition is applied to $\boldsymbol{u}$, matching the shear flow imposed by two parallel plates moving with a speed of $\dot{\gamma} H_p/2$ in opposite directions.

$$\nabla \psi = -\boldsymbol{H_0}; u = \dot{\gamma} H_p/2; v = 0; \nabla p_h = \boldsymbol{0}$$

$$\nabla \psi = -\boldsymbol{H_0} \qquad 2a \qquad \nabla \psi = -\boldsymbol{H_0}$$

$$\nabla \psi = -\boldsymbol{H_0}; u = -\dot{\gamma} H_p/2; v = 0; \nabla p_h = \boldsymbol{0}$$
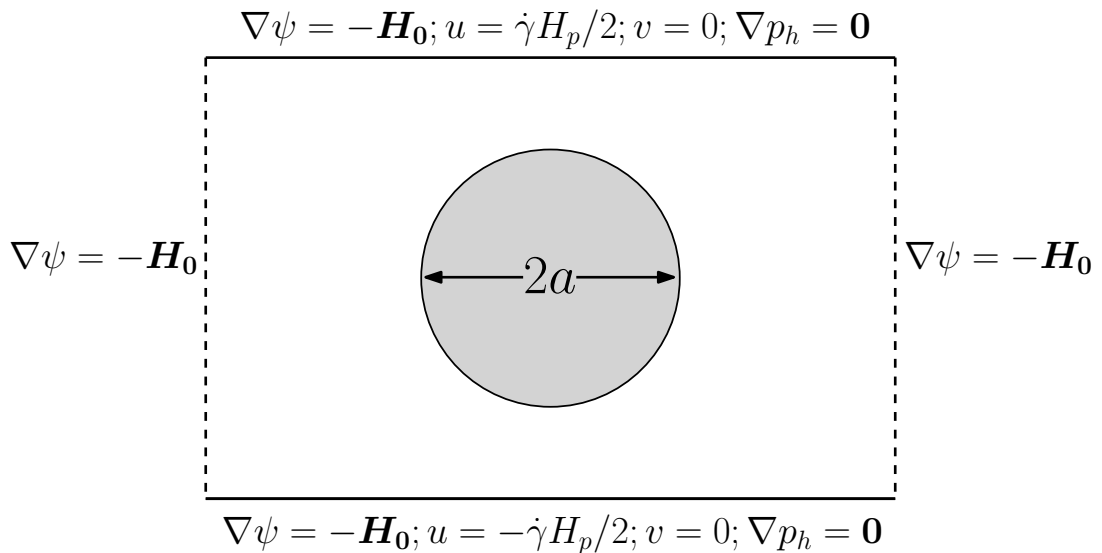
Figure 8 – Boundary conditions scheme.

3 Numerical Methodology

In this chapter, we present the numerical formulation and techniques adopted to solve the equations of magnetism, fluids motion and, the Level-Set function advection and reinitialization. We start with the Finite Difference method and some others numerical aspects such as staggered meshes used and how to build and solve the linear systems of equations. After, it is shown the numerical solution of the magnetic potential field. Then, we proceed with details of the Projection Method, discussing about the discretizations used for time and space. Finally, we expose techniques and technologies used in relation to the Level-Set method, such as geometrical properties computation, tubes technology and the solutions of the Level-Set function advection and reinitialization. The numerical application of the related boundary conditions is considered throughout the text.

3.1 Finite Difference Method

The Finite Difference Method is a numerical method based on the expansion of the Taylor's series to discretize differential equations by rewriting the derivatives as finite differences. This technique generates equations for the values of unknown functions at a finite number of points in the computational domain. The distribution of these points in the domain is known as grid. At each point, the function value is related to the values at neighboring points, resulting in a linear system of equations after the properly application of the problem boundary conditions. Finally, the solution of this system gives the problem solution at each point of the grid. The Finite Difference Method can be easily extended to multidimensional spatial domains, however it presents difficulties to lead with complex geometries.

3.1.1 Staggered grid

The two-dimensional domain discretization used in this work is based on a staggered grid (Harlow & Welch, 1965), as presented in Fig. 9. In this kind of grid, the fluids properties and scalar fields are evaluated at the center of the cells, represented in Fig. 9

by the dots, while, for the vector fields, the component in the $\hat{x}$ direction is evaluated on the cells right vertical walls and the component in the $\hat{y}$ direction is evaluated on the cells upper horizontal walls, respectively represented in Fig. 9 by the horizontal and vertical arrows. The i and j are used to enumerate the cells, respectively, from the left to the right in the horizontal direction and from the bottom to the top in the vertical direction. The staggered grid presents greater stability for the solution of the Navier-Stokes equation when compared to the collocated grid, i.e. every variable evaluated at the same position. In this work, only regular meshes are considered, such that $\Delta x = \Delta y = h$. The grid is composed by N_x cells in the horizontal direction and N_y in the vertical one. In this sense, we have $N_x \times N_y$ points for scalar fields (dots in Fig. 9) , $N_x + 1 \times N_y$ points for horizontal components of vector fields (right arrows in Fig. 9) and $N_x \times N_y + 1$ points for vertical components of vector fields (up arrows in Fig. 9). Ghosts nodes, i.e. nodes out of the domain, are commonly used for the application of boundary conditions as will be further explained.
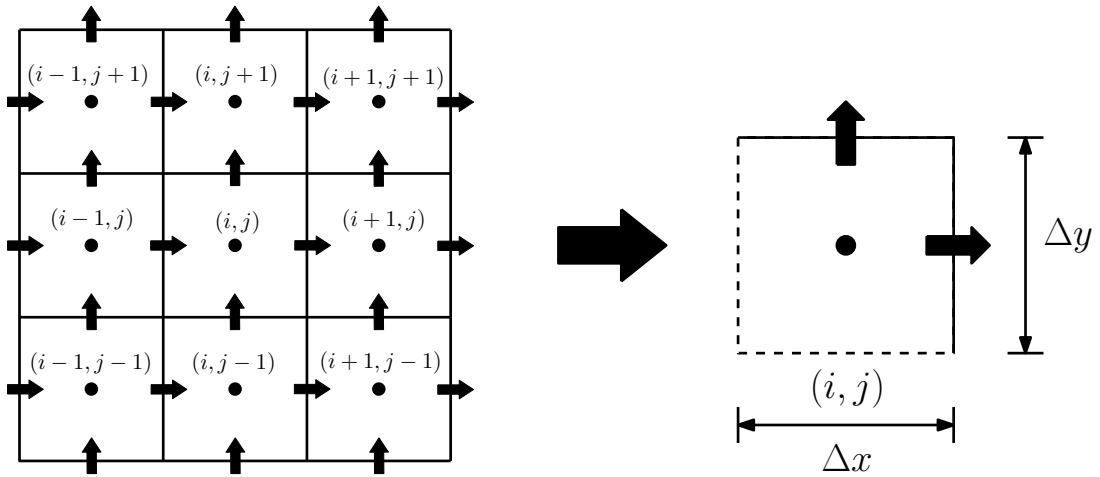
Figure 9 – Staggered grid and cell structures.

3.1.2 Discrete finite difference

The Taylor's series states that the value of a generic continuous function with all derivatives also continuous, $f = f(x)$, at a point x_a in the neighbor of x_0 may be given by

$$f(x_a) = f(x_0) + \frac{f'(x_0)}{1!}(x_a - x_0) + \frac{f''(x_0)}{2!}(x_a - x_0)^2 + \frac{f'''(x_0)}{3!}(x_a - x_0)^3 + ... \quad (3.1)$$

which can be rewritten in the more compact sigma notation as

$$f(x_a) = \sum_{n=0}^{\infty} \frac{f^{(n)}(x_0)}{n!}(x_a - x_0)^n. \tag{3.2}$$
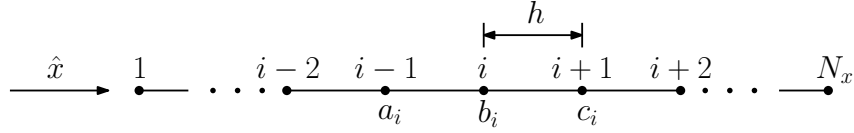
Figure 10 – Finite Difference Method one-dimensional domain discretization.

Consider the discretized one-dimensional domain as presented in Fig 10, such that $\{i \in \mathbb{Z} \mid 1 \leq i \leq N_x\}$. We can use the Taylor's series to predict the value of f at the node $i + 1$ by

$$f_{i+1} = f_i + \frac{f_i'}{1!}h + \frac{f_i''}{2!}h^2 + \mathcal{O}(h^3) \tag{3.3}$$

and predict the value of f at the node $i - 1$ by

$$f_{i-1} = f_i - \frac{f_i'}{1!}h + \frac{f_i''}{2!}h^2 + \mathcal{O}(h^3). \tag{3.4}$$

Notice that, in Eqs. 3.3 and 3.4, we are missing our predictions in a term in the order h^3, $\mathcal{O}(h^3)$. Subtracting and adding both equation we, respectively, get the central first and second differential derivatives

$$f_i' = \frac{f_{i+1} - f_{i-1}}{2h} + \mathcal{O}(h^3) \tag{3.5}$$

and

$$f_i'' = \frac{f_{i+1} - 2f_i + f_{i-1}}{h^2} + \mathcal{O}(h^3), \tag{3.6}$$

both with errors of order h^3. Infinity combinations of the Taylor's series expansion can be done in order to obtain the most varied types of numerical derivatives with different orders.

3.1.3 Building the liner system of equations

Once the differential equation is rewritten in term of finite differences, it is obtain the relation between the function value at a node and its neighbors. As example, let's work with the following two-dimensional Poisson equation for $\alpha = \alpha(\boldsymbol{x})$

$$\nabla^2 \alpha = p(\boldsymbol{x}), \tag{3.7}$$

where $p(\boldsymbol{x})$ is an arbitrary scalar function of the space. The discretization of the Eq. 3.7 in terms of central second-order finite difference is given by

$$\frac{1}{h^2}\left(\alpha_{(i-1,j)} + \alpha_{(i,j-1)} - 4\alpha_{(i,j)} + \alpha_{(i+1,j)} + \alpha_{(i,j+1)}\right) = p_{(i,j)} \qquad (3.8)$$

which can be rewritten as

$$a_{(i,j)}\,\alpha_{(i-1,j)} + b_{(i,j)}\,\alpha_{(i,j-1)} + c_{(i,j)}\,\alpha_{(i,j)} + d_{(i,j)}\,\alpha_{(i+1,j)} + e_{(i,j)}\,\alpha_{(i,j+1)} = f_{(i,j)}, \qquad (3.9)$$

being $a_{(i,j)}$, $b_{(i,j)}$, $c_{(i,j)}$, $d_{(i,j)}$ and $e_{(i,j)}$ the coefficients respectively multiplying $\alpha_{(i-1,j)}$, $\alpha_{(i,j-1)}$, $\alpha_{(i,j)}$, $\alpha_{(i+1,j)}$, and $\alpha_{(i,j+1)}$, and $f_{(i,j)}$ the single term.

In this example, we are using what is called an stencil of five points to describe the equation for each node, once there are five nodes being used to write the equation for the node (i,j). In numerical analysis, a stencil is a geometric arrangement of a group of nodes related to a point of interest. Figure 11 presents a compact two-dimensional stencil and the notation here used for each node. Notably, the size of the stencil is proportional to the order of the method, since finite difference approximation of higher order require more nodes in the computation.
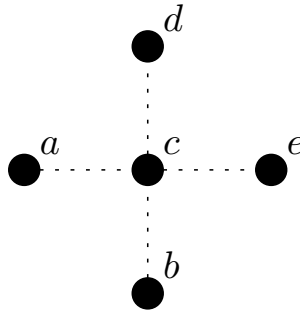
Figure 11 – Compact two-dimensional stencil with 5 nodes.

Now, we have a single equation for each node. However, we still need to apply the problem boundary conditions to the nodes at the boundaries. Once these conditions are applied, it becomes possible to write the linear system $\boldsymbol{A} \cdot \boldsymbol{\alpha} = \boldsymbol{b}$, in which: the solution vector, $\boldsymbol{\alpha}$, contains the value of the function α evaluated at every node; $\boldsymbol{A}$ is the matrix of the coefficients $a_{(i,j)}$, $b_{(i,j)}$, $c_{(i,j)}$, $d_{(i,j)}$ and $e_{(i,j)}$; and $\boldsymbol{b}$ is the vector of the coefficient $f_{(i,j)}$.

In this work, the solution of the linear system is obtained by the use of the symmetric successive over-relaxation preconditioned Conjugated Gradient Method presented

in Li et al. (2013). This method excludes the necessity of building the matrix $\boldsymbol{A}$, once only the product $\boldsymbol{A} \cdot \boldsymbol{\alpha}$ takes part in the algorithm, which can be easily computed. Each element $b_{(i,j)}$ of the product $\boldsymbol{A} \cdot \boldsymbol{\alpha}$ is computed by

$$b_{(i,j)} = a_{(i,j)}\, \alpha_{(i-1,j)} + b_{(i,j)}\, \alpha_{(i,j-1)} + c_{(i,j)}\, \alpha_{(i,j)} + d_{(i,j)}\, \alpha_{(i+1,j)} + e_{(i,j)}\, \alpha_{(i,j+1)}. \tag{3.10}$$

In this sense, it is avoided the waste of computational memory and processing time, since the matrix $\boldsymbol{A}$ is a sparse matrix.

3.2 Magnetic potential field numerical solution

The magnetic potential field is governed by Eq. 2.48. The central second-order spatial discretization of Eq. 2.10 is given by

$$\begin{aligned}
\nabla \cdot (\zeta \nabla \psi)_{(i,j)} &= \psi_{(i-1,j)}\zeta_{(i-1/2,j)}/h^2 + \psi_{(i,j-1)}\zeta_{(i,j-1/2)}/h^2 & (3.11)\\
&- \psi_{(i,j)}\left(\zeta_{(i-1/2,j)} + \zeta_{(i,j-1/2)} + \zeta_{(i+1/2,j)} + \zeta_{(i,j+1/2)}\right)/h^2 & (3.12)\\
&+ \psi_{(i+1,j)}\zeta_{(i+1/2,j)}/h^2 + \psi_{(i,j+1)}\zeta_{(i,j+1/2)}/h^2. & (3.13)
\end{aligned}$$

Therefore,

$$\begin{aligned}
a_{i,j} &= \zeta_{(i-1/2,j)}/h^2 \\
b_{i,j} &= \zeta_{(i,j-1/2)}/h^2 \\
c_{i,j} &= \left(\zeta_{(i-1/2,j)} + \zeta_{(i,j-1/2)} + \zeta_{(i+1/2,j)} + \zeta_{(i,j+1/2)}\right)/h^2 \\
d_{i,j} &= \zeta_{(i+1/2,j)}/h^2 \\
e_{i,j} &= \zeta_{(i,j+1/2)}/h^2 \\
f_{i,j} &= 0. \tag{3.14}
\end{aligned}$$

The index $(i + 1/2, j)$ refers to a position in between $(i + 1, j)$ and (i, j), and, according to Patankar (1980), the ζ at this position should be computed by the harmonic average of $\zeta_{(i+1,j)}$ and $\zeta_{(i,j)}$, in order to avoid instabilities.

The boundary conditions for the potential field are applied as heterogeneous Neumann condition, representing a Dirichlet condition for the magnetic field, $\nabla \psi = -\boldsymbol{H}_0$. Let's focus on the application of this condition at the right boundary. Important to remember that the potential field is computed at the center of the computational cell, i.e.
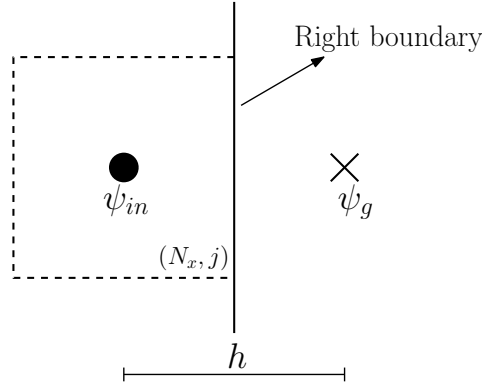
Figure 12 – Boundary conditions application on the right.

the dot in Fig. 9. In Fig. 12, the cross represents where the left neighbor node would be, usually called as ghost.

Applying $\partial\psi/\partial x = -H_{0x}$ as finite difference at the right boundary, we get that

$$\frac{\psi_g - \psi_{in}}{h} = -H_{0x}, \tag{3.15}$$

being ψ_g the potential field at the ghost node. Thus,

$$\psi_g = \psi_{in} - hH_{0x}. \tag{3.16}$$

Finally, in the equation for the nodes at right boundary $(i = N_x, j)$, the coefficient $c_{(i,j)}$ receives $c_{(i,j)} + d_{(i,j)}$ while ψ_g receives $-hH_{0x}$. Notice that, despite the ghost node does not physically exist, its value takes place at the product of the matrix of coefficients and solution vector for the Conjugate Gradient Method. The same procedure is done for the others boundaries.

Important to emphasize that, the Eq. 2.48 with Neumann conditions applied at every boundary presents infinity solutions for ψ varying by a constant. Any of these solutions satisfy our problem, since only $\nabla\psi$ interests us. The Conjugated Gradient Method will give the closest solution to the given first guess, which here is $\psi(\boldsymbol{x}) = 0$.

3.3 Projection method

First presented by Chorin (1967), the projection method became a popular numerical methodology for solving time-dependent incompressible viscous flow problems. It is based on decoupling the solutions of the velocity and pressure fields by the introduction

of an artificial compressibility, in such a way that it does not affect the final results. This method relies on different types of finite dicretization of time on the equations of motion, each one resulting in different approaches of the original method with respective convergence orders (Brown et al., 2001). Typically, the momentum equation is solved for the velocity field in a mid-time-step position, denoted predictor step. Then, the pressure field is solved enforcing the divergence free of the velocity field in the next time-step. Finally, a corrector of the velocity predictor is computed from the pressure field gradient.

In this work, the predictor velocity, $\boldsymbol{u}^*$, is first computed using a second order backward finite difference, as follows

$$\frac{3\boldsymbol{u}^* - 4\boldsymbol{u}^n + \boldsymbol{u}^{n-1}}{2\Delta t} = \frac{\lambda}{Re}\nabla^2\boldsymbol{u}^* + \boldsymbol{\mathcal{G}}(\hat{\boldsymbol{u}}) + \hat{\boldsymbol{F}}_m + \hat{\boldsymbol{F}}_c, \tag{3.17}$$

where Δt is the numerical time step, $\hat{\boldsymbol{u}} = 2\boldsymbol{u}^n - \boldsymbol{u}^{n-1}$ is an extrapolation of $\boldsymbol{u}^{n+1}$,

$$\hat{\boldsymbol{F}}_m = \frac{Ca_{mag}}{Ca\,Re}(\zeta(\hat{\phi}) - 1)\boldsymbol{H}\cdot\nabla\boldsymbol{H} \tag{3.18}$$

is the magnetic force computed with the extrapolation of $\hat{\phi}$ for ϕ^{n+1},

$$\hat{\boldsymbol{F}}_c = -\frac{1}{Ca\,Re}\kappa\delta(\hat{\phi})\nabla\hat{\phi} \tag{3.19}$$

is the capillary force computed with the extrapolation of $\hat{\phi}$ for ϕ^{n+1} and

$$\boldsymbol{\mathcal{G}}(\hat{\boldsymbol{u}}) = -\hat{\boldsymbol{u}}\cdot\nabla\hat{\boldsymbol{u}} - \frac{\lambda}{Re}\nabla^2\hat{\boldsymbol{u}} + \frac{1}{Re}\nabla\cdot(\lambda(\phi)(\nabla\hat{\boldsymbol{u}} + \nabla\hat{\boldsymbol{u}}^T)). \tag{3.20}$$

The velocity at the time t^{n+1} is related with p_h^{n+1} and $\boldsymbol{u}^*$ by

$$\frac{3}{2\Delta t}(\boldsymbol{u}^{n+1} - \boldsymbol{u}^*) = -\nabla p_h^{n+1}. \tag{3.21}$$

Notice that, by substituting Eq. 3.21 in Eq. 3.17 the original Eq. 2.50 is recovered for $\Delta t \to 0$. For the flow incompressibility to be satisfied at t^{n+1}, we get that Eq. 3.21 becomes Eq. 3.22 by simply taking the divergent on both side of the equation.

$$\nabla^2 p_h^{n+1} = \frac{3}{2\Delta t}\nabla\cdot\boldsymbol{u}^*. \tag{3.22}$$

Then, with the solution of Eq. 3.22, p_h^{n+1} and u^* can be used in Eq. 3.21 in order to get $\boldsymbol{u}^{n+1}$.

3.3.1 Numerically solving the projection method

The numerical solution of the projection method must start by solving $\boldsymbol{u}^*$. Working on the spatial discretization of Eqs. 3.17 to 3.20 for the component $\boldsymbol{u}^*$ in the $\hat{x}$ direction, u^*, we get

$$\frac{3u^*_{(i,j)} - 4u^n_{(i,j)} + u^{n-1}_{(i,j)}}{2\Delta t} = \frac{\lambda_{(f)}}{Re}\left(\nabla^2 u^*\right)_{(i,j)} + \boldsymbol{\mathcal{G}}(\hat{\boldsymbol{u}})_{x(i,j)} + \boldsymbol{F}_{mx(i,j)} + \boldsymbol{F}_{cx(i,j)}, \qquad (3.23)$$

Notice that, since $\lambda_{(i,j)}$ is a property, it is evaluated at the center of the cell (i,j) while $u^*_{(i,j)}$, being the component of a vector, is evaluated at the right face of this cell (see Fig. 9). Therefore, the value of λ at the same position of $u^*_{(i,j)}$, $\lambda_{(f)}$, is computed by the arithmetic average between $\lambda_{(i+1,j)}$ and $\lambda_{(i,j)}$. This same notation will be used for ζ, κ and ϕ, once all of them are evaluated at the cell center. Equation 3.23 can be rewritten in the stencil notation as:

$$
\begin{aligned}
a_{(i,j)} &= -\frac{\Delta t\left(\lambda_{(f)}\right)}{Re\,h^2} \\
b_{(i,j)} &= -\frac{\Delta t\left(\lambda_{(f)}\right)}{Re\,h^2} \\
c_{(i,j)} &= \frac{3}{2} + \frac{4\Delta t\left(\lambda_{(f)}\right)}{Re\,h^2} \\
d_{(i,j)} &= -\frac{\Delta t\left(\lambda_{(f)}\right)}{Re\,h^2} \\
e_{(i,j)} &= -\frac{\Delta t\left(\lambda_{(f)}\right)}{Re\,h^2} \\
f_{(i,j)} &= 2u^n - \frac{u^{n-1}}{2} + \Delta t\left(\boldsymbol{\mathcal{G}}(\hat{\boldsymbol{u}})_{x(i,j)} + \boldsymbol{F}_{mx(i,j)} + \boldsymbol{F}_{cx(i,j)}\right).
\end{aligned}
\qquad (3.24)
$$

The magnetic force in the x direction, $\boldsymbol{F}_{mx(i,j)}$, is computed by

$$(\boldsymbol{F}_{mx})_{(i,j)} = \frac{Ca_{mag}}{Ca\,Re}\left(\zeta_{(f)} - 1\right)(\boldsymbol{H}\cdot\nabla\boldsymbol{H})_{x(i,j)}, \qquad (3.25)$$

where

$$
\begin{aligned}
(\boldsymbol{H}\cdot\nabla\boldsymbol{H})_{x(i,j)} &= H_{x(i,j)}\left(\frac{H_{x(i+1,j)} - H_{x(i-1,j)}}{2h}\right) \\
&+ \left(\frac{H_{y(i,j)} + H_{y(i+1,j)} + H_{y(i,j-1)} + H_{y(i+1,j-1)}}{4}\right)\left(\frac{H_{x(i,j+1)} - H_{x(i,j-1)}}{2h}\right).
\end{aligned}
$$
$$(3.26)$$

The capillary force in the x direction, $\boldsymbol{F}_{cx(i,j)}$, is computed by

$$(\boldsymbol{F}_{cx})_{(i,j)} \;=\; -\frac{1}{Ca\,Re}\kappa_{(f)}\left(\frac{\phi_{(i+1,j)} - \phi_{(i,j)}}{h}\right)\delta_\varepsilon\left(\phi_{(f)}\right). \tag{3.27}$$

Finally, $\boldsymbol{\mathcal{G}}(\hat{\boldsymbol{u}})_{x(i,j)}$ is computed by

$$
\begin{aligned}
\boldsymbol{\mathcal{G}}(\hat{\boldsymbol{u}})_{x(i,j)} \;=\; & -\left(\hat{u}\frac{\partial \hat{u}}{\partial x} + \hat{v}\frac{\partial \hat{u}}{\partial y})\right)_{(i,j)} \\
& -\left(\frac{\lambda}{Re}\nabla^2\hat{u}\right)_{(i,j)} \\
& +\left[\frac{1}{Re}\frac{\partial}{\partial x}\left(2\lambda\frac{\partial \hat{u}}{\partial x}\right)\right]_{(i,j)} \\
& +\left[\frac{1}{Re}\frac{\partial}{\partial y}\left(\lambda\left(\frac{\partial \hat{u}}{\partial y} + \frac{\partial \hat{v}}{\partial x}\right)\right)\right]_{(i,j)}.
\end{aligned}
\tag{3.28}
$$

The convective term, $\left(\hat{u}\frac{\partial \hat{u}}{\partial x} + \hat{v}\frac{\partial \hat{u}}{\partial y}\right)_{(i,j)}$, presents unwanted oscillations since its numerical computation is not always numerically accurate (Sussman et al., 1994). Therefore, this term is computed with the upwind second-order using the ENO (Essentially Non-Oscillatory) scheme presented in Shu & Osher (1988); Mulder et al. (1992), in order to keep the method stable. Following with the discretization,

$$\left(\frac{\lambda}{Re}\nabla^2\hat{u}\right)_{(i,j)} = \frac{\lambda_{(f)}}{Re}\left(\frac{\hat{u}_{(i-1,j)} + \hat{u}_{(i,j-1)} - 4\hat{u}_{(i,j)} + \hat{u}_{(i+1,j)} + \hat{u}_{(i,j+1)}}{h^2}\right), \tag{3.29}$$

$$\left[\frac{1}{Re}\frac{\partial}{\partial x}\left(2\lambda\frac{\partial \hat{u}}{\partial x}\right)\right]_{(i,j)} = \frac{2}{Re}\left(\frac{\lambda_{(lf)}\hat{u}_{(i-1,j)} - (\lambda_{(lf)} + \lambda_{(rt)})\hat{u}_{(i,j)} + \lambda_{(rt)}\hat{u}_{(i+1,j)}}{h^2}\right), \tag{3.30}$$

and

$$
\begin{aligned}
\left[\frac{1}{Re}\frac{\partial}{\partial y}\left(\lambda\left(\frac{\partial \hat{u}}{\partial y} + \frac{\partial \hat{v}}{\partial x}\right)\right)\right]_{(i,j)} \;=\; & \frac{1}{Re}\left(\frac{\lambda_{(dn)}\hat{u}_{(i,j-1)} - \left(\lambda_{(dn)} + \lambda_{(up)}\right)\hat{u}_{(i,j)} + \lambda_{(up)}\hat{u}_{(i,j+1)}}{h^2}\right) \\
& + \frac{1}{Re}\left(\frac{\lambda_{(dn)}\left(\hat{v}_{(i,j-1)} - \hat{v}_{(i+1,j-1)}\right) + \lambda_{(up)}\left(\hat{v}_{(i+1,j)} - \hat{v}_{(i,j)}\right)}{h^2}\right).
\end{aligned}
\tag{3.31}
$$

Here,

$$
\begin{aligned}
\lambda_{(lf)} &= \lambda_{(i,j)} \\
\lambda_{(rt)} &= \lambda_{(i+1,j)} \\
\lambda_{(dn)} &= \frac{\left(\lambda_{(i,j)} + \lambda_{(i+1,j)} + \lambda_{(i,j-1)} + \lambda_{(i+1,j-1)}\right)}{4} \\
\lambda_{(up)} &= \frac{\left(\lambda_{(i,j)} + \lambda_{(i+1,j)} + \lambda_{(i,j+1)} + \lambda_{(i+1,j+1)}\right)}{4}
\end{aligned}
\tag{3.32}
$$

Once we got the discretized equation for u^*, we must proceed with the boundary conditions. Since $\nabla p = \mathbf{0}$ is a boundary condition of the problem at the upper and botton plates, following Eq. 3.21, u^* must be equal to u^{n+1} at these boundaries, i.e. U_p and $-U_p$ for the upper and button plates, respectively. Since there are no evaluated points of u^* on these boundaries, we must proceed with the use of ghost nodes, as done for the magnetic potential field. Figure 13 presents a scheme of the boundary condition application for u^* at the upper boundary.
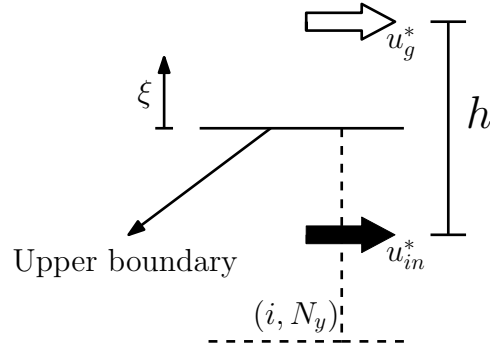
Figure 13 – Boundary conditions application for u^* at the upper boundary.

From the interpolation between u^*_{in} and u^*_b (u^* evaluated at the boundary), we get $u^* = u^*(\xi)$ as

$$
u^*(\xi) = u^*_b + \xi \left(\frac{u^*_b - u^*_{in}}{h/2}\right),
\tag{3.33}
$$

thus

$$
u^*(h/2) = u^*_g = 2u^*_b - u^*_{in}.
\tag{3.34}
$$

In the equation for the node at the upper boundary ($i = i, N_y$), the coefficient $c_{(i,j)}$ receives $c_{(i,j)} + d_{(i,j)}$ while u^*_g receives $2u^*_b$. The same procedure is done for the button boundary. For the side boundaries, the periodic boundary condition is applied, such that

the right boundary sees the left boundary, and vice versa. Numerical manipulations are not needed for the boundary conditions of v^* at the upper and bottom plates, since the evaluation point for this component lays right on these boundaries, thus the Dirichlet condition can be directly applied.

Once the $\boldsymbol{u}^*$ field is computed, we must go on with the solution of the pressure field, given by the numerical solution of Eq. 3.22. This equation can be rewritten in the stencil notation as follows:

$$
\begin{aligned}
a_{(i,j)} &= \frac{1}{h^2} \\
b_{(i,j)} &= \frac{1}{h^2} \\
c_{(i,j)} &= -\frac{4}{h^2} \\
d_{(i,j)} &= \frac{1}{h^2} \\
e_{(i,j)} &= \frac{1}{h^2} \\
f_{(i,j)} &= \frac{3}{2\Delta t}\left(\frac{u_{i+1,j}^* - u_{i-1,j}^*}{h} + \frac{v_{i,j+1}^* - v_{i,j-1}^*}{h}\right).
\end{aligned}
\tag{3.35}
$$

The boundary conditions for the pressure field are applied in the same way as done for the magnetic potential field, however $\nabla p = \boldsymbol{0}$ at every boundary.

With both $\boldsymbol{u}^*$ and pressure fields solved, we are finally able to compute $\boldsymbol{u}^{n+1}$ with Eq. 3.21. For the horizontal component,

$$
u^{n+1} = -\frac{2\Delta t}{3}\frac{\partial p_h^{n+1}}{\partial x} + u^*,
\tag{3.36}
$$

which in the discretized form becomes,

$$
u_{i,j}^{n+1} = \frac{2\Delta t}{3}\left(\frac{p_{i+1,j}^{n+1} - p_{i,j}^{n+1}}{h}\right) + u_{i,j}^*.
\tag{3.37}
$$

3.4   Level-Set numerical aspects

The Level-Set method lays on the advection of the level-set function and its reinitialization, respectively given by the numerical solution of Eqs. 2.38 and 2.52. However, these numerical solutions are not trivial and take great computational efforts. Here, it is presented all the numerical techniques used to deal with the numerical instabilities and to reduce computational efforts.

3.4.1   Initializationn of the Level-Set function

The initialization of the signed distance function is the first thing to be done in relation to the Level-Set method. In this work, the droplet initial shape is always a circumference, therefore this step becomes quite trivial. For every node of the grid, the distance function is set as the smallest distance measured between the node and many points over the circumference. Remembering that the distance function is measured at the center of the cell (the dots in Fig. 9). These points are equally spaced by an angle increment, and as smaller it is this increment, more accurate is the computation of the distance function. Finally, the distance from the node to the center of the circumference is used to verify if it is located inside or outside the droplet domain. If inside, the distance function is singed as negative, otherwise positive. Notice that, during the all numerical simulation, this procedure is done only once.

3.4.2   Computation of geometric properties

In the problem under study, the accurate computation of geometric properties related to the droplet geometry is extremely important. Here, we present how to compute these properties.

- Normal vector ($\boldsymbol{n}$): As presented in section 2.7, case ϕ is the signed distance function, the interface normal vector may be computed as $\nabla\phi$. However, since the reinitialization process is not applied at each time step of the simulation, we cannot guarantee that $|\nabla\phi| = 1$ all the time. Therefore, we compute the normal vector as

$$\boldsymbol{n} = \frac{\nabla\phi}{|\nabla\phi|}. \tag{3.38}$$

The numerical computation of this property is given by

$$
\begin{aligned}
n_{x(i,j)} &= \frac{\phi_{(i+1,j)} - \phi_{(i-1,j)}}{\sqrt{\left(\phi_{(i+1,j)} - \phi_{(i-1,j)}\right)^2 + \left(\phi_{(i,j+1)} - \phi_{(i,j-1)}\right)^2}} \\
n_{y(i,j)} &= \frac{\phi_{(i,j+1)} - \phi_{(i,j-1)}}{\sqrt{\left(\phi_{(i+1,j)} - \phi_{(i-1,j)}\right)^2 + \left(\phi_{(i,j+1)} - \phi_{(i,j-1)}\right)^2}}
\end{aligned}
\tag{3.39}
$$

being $n_{x(i,j)}$ and $n_{y(i,j)}$ the components of the normal vector in the x and y directions, respectively, compuetd at the center of the cell.

- Curvature (κ): Also presented in section 2.7, the computation of the curvature is given by $\kappa = \nabla \cdot \boldsymbol{n}$. Its geometric property is also computed at the center of the cell, thus its numerical computation is given by

$$\kappa_{(i,j)} = \frac{n_{x(i+1,j)} - n_{x(i-1,j)}}{2h} + \frac{n_{y(i,j+1)} - n_{y(i,j-1)}}{2h}. \tag{3.40}$$

Important to notice that, the computation of the curvature at the (i, j) depends on the value of ϕ in two more nodes in each direction, giving a total of 9 points, i.e. a stencil of 9 points as presented in Fig. 14.
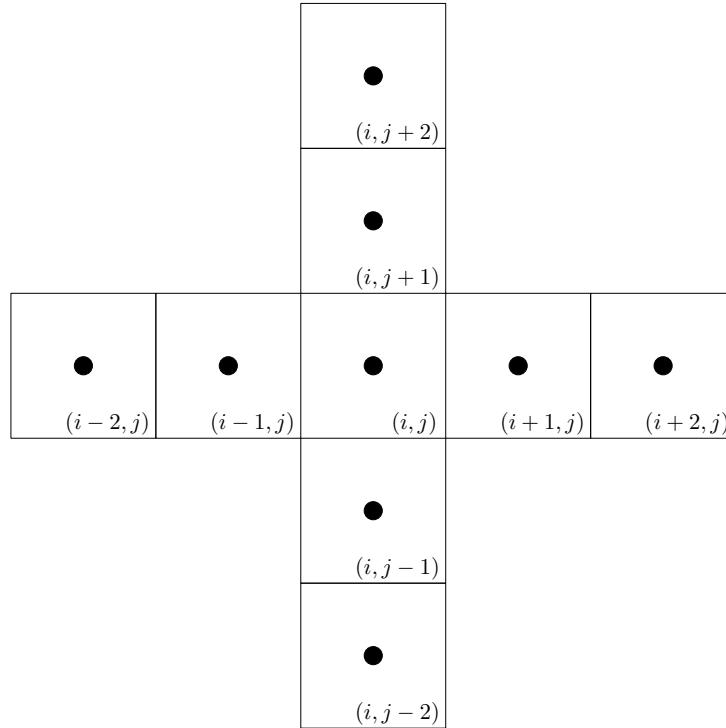
Figure 14 – Stencil of nine points to compute the curvature at the center of the cell (i, j).

- Sign function ($\text{sgn}(\phi)$): The computation of the signed function of ϕ is fundamental for the reinitialization scheme of the level-set function (see Eq. 2.52). The traditional signed function returns the values 1 or -1, which will enter as the propagation velocity of ϕ in the reinitialization process. However, its use may cause some numerical instabilities to the method. Peng et al. (1999) suggests the introduction of a smooth signed function, $S_s(\phi)$, given by

$$S_s(\phi) = \frac{\phi}{\sqrt{\phi^2 + (|\nabla\phi|h)^2}}. \tag{3.41}$$

The use of S_s ensures that the interface is confined to one cell in the reinitialization step. Also, it solves the problem of the changing of sing of ϕ in the reinitialization

step when ϕ is steep, which would move the interface across the cell boundary, and speeds up the convergence when ϕ is flat at the interface. The numerical computation of the smoothed signed function is then given by

$$S_s\left(\phi_{(i,j)}\right) = \frac{\phi_{(i,j)}}{\sqrt{\phi_{(i,j)}^2 + \left(|\nabla\phi|_{(i,j)}h\right)^2}} \tag{3.42}$$

where

$$|\nabla\phi|_{(i,j)} = \sqrt{\left(\frac{\phi_{(i+1,j)} - \phi_{(i-1,j)}}{2h}\right)^2 + \left(\frac{\phi_{(i,j+1)} - \phi_{(i,j-1)}}{2h}\right)^2}. \tag{3.43}$$

3.4.3 Tubes technology

First introduced by Peng et al. (1999), the use of the tubes technology strongly decreases the computational efforts related to the solution of the advection and reinitialization equations of the level-set function by delimiting regions in the domain where these equations will be solved, and also avoids numerical problems close to the boundaries. Consider three constants α_t, β_t and γ_t comparable to the cell size, h, such that $0 < \alpha_t < \beta_t < \gamma_t$. Let's define the tube T_L around the fluids interface as being the sub-domain

$$T_L = \{\boldsymbol{x} : \phi(\boldsymbol{x}) < \gamma_t\}. \tag{3.44}$$

In this perspective, the level-set function $\phi(\boldsymbol{x})$ must only coincide with the signed distance function in T_L. Thus, the advection of the level-set function is done with,

$$\frac{\partial\phi}{\partial t} = c(\phi)\boldsymbol{u} \cdot \nabla\phi = 0 \tag{3.45}$$

or

$$\frac{\partial\phi}{\partial t} = c(\phi)u_n|\nabla\phi| = 0, \tag{3.46}$$

where $c(\phi)$ is the cut-off function given by

$$c(\phi) = \begin{cases} 1, & \text{if } \phi < \beta_t, \\ (\phi - \gamma)^2(2\phi + \gamma - 3\beta)/(\gamma - \beta)^3, & \text{if } \beta_t < \phi \leq \gamma_t, \\ 0, & \text{if } \phi > \gamma_t. \end{cases} \tag{3.47}$$

The use of the cut-off function in Eqs. 3.45 and 3.46 prevents numerical oscillations at the tube boundary. Notice that: we are solving the original level-set advection equation only in the tubes of radius α_t and β_t; in the region $\{\boldsymbol{x} : \beta_t < \phi(\boldsymbol{x}) < \gamma_t\}$, the motion is modified by the cut-off function; and outside the tube T_L we do not update ϕ. The use of the cut-off function in Eqs. 3.45 and 3.46 prevents numerical oscillations at the tube boundary.

Since extensional effects of the droplet surface plays no role in the problem under study (e.g. Marangoni effect), we do only care about modifications on the droplet geometry (i.e. deformation on the normal direction), therefore we solve the Eq. 3.46 to advect ϕ. The time step, Δt, used to evolve ϕ must be such that the fluid interface does not moves more than one cell size, $\Delta t|\boldsymbol{u}| < h$. Since this front moves less than one cell size, we choose the region N_L where the level-set function must suffer the reinitialization as

$$N_L = \{\boldsymbol{x} : \phi(\boldsymbol{x}) + h < \gamma_t\}. \tag{3.48}$$

Thus, ϕ is the signed distance function just for $\boldsymbol{x} \in N_L$.

Despite the tube α_t plays no role at the cut-off function, this region defines where the Level-Set function and geometric properties must be the most precisely computed as possible. This region contains the smoothed Dirac Delta function (δ_ε) differing from zero and variations on the Heavyside function (H_ε), which couples the fluids interface effects to the motion and magnetic equations.

3.4.4 Solving the level set function advection

The advection of the level-set function is here computed by Eq. 3.46. As a hyperbolic equation, its solution only requires initial conditions. Here, this solution is obtained by the use of the Total-Variation-Diminishing (TVD) third-order method presented in Shu & Osher (1988). This is a third order method in time, which guarantees that this solution will not affect the method overall order. Also, this method presents a great stability due to the reduction on the error accumulation over the iterations. This Runge-Kutta method is completed in three steps:

$$\begin{aligned}
\phi^{(1)} &= \phi^{(0)} + \boldsymbol{u} \cdot \nabla \phi^{(0)} c(\phi) \Delta t \\
\phi^{(2)} &= \frac{3}{4}\phi^{(0)} + \frac{1}{4}\phi^{(1)} + \frac{1}{4}\boldsymbol{u} \cdot \nabla \phi^{(1)} c(\phi) \Delta t \\
\phi^{(3)} &= \frac{1}{3}\phi^{(0)} + \frac{2}{3}\phi^{(2)} + \frac{2}{3}\boldsymbol{u} \cdot \nabla \phi^{(2)} c(\phi) \Delta t,
\end{aligned} \tag{3.49}$$

being $\phi^{(0)}$ the level-set function before the advection, $\phi^{(1)}$ and $\phi^{(2)}$ the level-set function at middle steps, and $\phi^{(3)}$ the advected level-set function in a time step of Δt. In order to guarantee a great approximation of the spatial derivatives, the convective term, $\boldsymbol{u} \cdot \nabla \phi$, is computed using the Weighted Essentially Non-Oscillatory (WENO) scheme of fifth order, presented in Jiang & Peng (2000). In face of that, Peng et al. (1999) recommend to set $\alpha_t = 3h$, $\beta_t = 6h$ and $\gamma_t = 9h$ to build the tubes, since the computation of the space derivatives demands a stencil of 11 points (see Jiang & Peng (2000)).

3.4.5 Solving the reinitialization

As done for the advection of the level-set function, the reinitialization equation is solve using the third order TVD and fifth order WENO. This strategy is pretty similar to the one used in Sussman et al. (1994). We define

$$\begin{aligned}
a\left(\phi_{(i,j)}\right) &= D_x^- \phi_{(i,j)} \\
b\left(\phi_{(i,j)}\right) &= D_x^+ \phi_{(i,j)} \\
c\left(\phi_{(i,j)}\right) &= D_y^- \phi_{(i,j)} \\
d\left(\phi_{(i,j)}\right) &= D_y^+ \phi_{(i,j)}
\end{aligned} \tag{3.50}$$

and

$$\begin{aligned}
G(\phi)_{(i,j)} &= S_{s(i,j)}^+ \left(\sqrt{\max\left[\left(a_{(i,j)}^+\right)^2, \left(b_{(i,j)}^-\right)^2\right] + \max\left[\left(c_{(i,j)}^+\right)^2, \left(d_{(i,j)}^-\right)^2\right]} - 1 \right) \\
&+ S_{s(i,j)}^- \left(\sqrt{\max\left[\left(a_{(i,j)}^-\right)^2, \left(b_{(i,j)}^+\right)^2\right] + \max\left[\left(c_{(i,j)}^-\right)^2, \left(d_{(i,j)}^+\right)^2\right]} - 1 \right)
\end{aligned} \tag{3.51}$$

Here, $D_x^\pm$ and $D_y^\pm$ are the one-sided differences computed with fifth order WENO scheme, as presented in see Jiang & Peng (2000). Therefore, the TVD method is completed with

$$
\begin{aligned}
\phi^{(1)} &= \phi^{(0)} - G(\phi^{(0)})\Delta\tau \\
\phi^{(2)} &= \frac{3}{4}\phi^{(0)} + \frac{1}{4}\phi^{(1)} - \frac{1}{4}G(\phi^{(1)})\Delta\tau \\
\phi^{(3)} &= \frac{1}{3}\phi^{(0)} + \frac{2}{3}\phi^{(2)} + \frac{2}{3}G(\phi^{(2)})\Delta\tau,
\end{aligned}
\tag{3.52}
$$

being $\phi^{(0)}$ the level-set function before the reinitialization, $\phi^{(1)}$ and $\phi^{(2)}$ the level-set function at middle steps, and $\phi^{(3)}$ the reinitialized level-set function in a time step of $\Delta\tau$. This procedure is repeated until the $|\nabla\phi|$ reaches the unit in the tubes regions, i.e. the steady state of Eq. 2.52.

4 Numerical Validation

This chapter is devoted to the validation of the described mathematical model and numerical methodology. For this purpose, it is studied four benchmark problems, comparing the predictions here obtained with analytical, experimental and numerical results available in the related literature (Taylor, 1934; Rosensweig, 1997; Flament et al., 1996; Ghigliotti et al., 2010). First, the numerical solution for the magnetic field for a circular magnetic droplet subjected to an external uniform magnetic field is set side by side with the analytical solution of a magnetizable disk immersed in a uniform magnetic field (Rosensweig, 1997). Then, we do comparisons between the equilibrium shape for a magnetic drop in a uniform magnetic field given by simulations and similar cases experimented by Flament et al. (1996) in a Hele-Shaw cell. After, the result obtained in Taylor (1934) for the droplet inclination in the limit of small capillary numbers is recovered. Following, the inclination and reduced viscosity of a two-dimensional droplet in a shear flow imposed by parallel plates from Ghigliotti et al. (2010) is reproduced here. Finally, a study on the method convergence rate is done, considering the case of a single drop under the influence of both shear flow and magnetic effects.

4.1 Magnetic field for a circular droplet

The magnetic potential field, ψ, for a disk immersed in a uniform magnetic field is a classical problem in magnetostatics, governed by the Laplace equation, $\nabla^2 \psi = 0$. The analytical solution in polar coordinates (r, θ) is well known and given by:

$$\psi(r, \theta) = \sum_n \left(A_n r^n + \frac{B_n}{r^n} \right) \left(C_n \cos n\theta + D_n \sin n\theta \right). \tag{4.1}$$

Once the disk radius a, the magnetic permeability ratio between the disk and the outer domain ζ and the applied magnetic field $\boldsymbol{H}_0 = H_0 \hat{\boldsymbol{e}}_x$, the general solution brings us to

the following:

$$\boldsymbol{H}(r,\theta) = \begin{cases} (-c_1 + c_2/r^2)\cos\theta\hat{\boldsymbol{e}}_r + (c_1 + c_2/r^2)\sin\theta\hat{\boldsymbol{e}}_\theta, & \text{if } r > a \\ c_3(\cos\theta\hat{\boldsymbol{e}}_r - \sin\theta\hat{\boldsymbol{e}}_\theta), & \text{if } r < a. \end{cases} \tag{4.2}$$

Applying the boundary conditions at the infinity as $\boldsymbol{H}(r \to \infty, \theta) = H_0\cos\theta\hat{\boldsymbol{e}}_r - H_0\sin\theta\hat{\boldsymbol{e}}_\theta$ and considering the continuities of $\boldsymbol{B}$ on the normal direction and $\boldsymbol{H}$ on the tangential direction at the disk boundaries, we get that

$$c_1 = -H_0, \tag{4.3}$$

$$c_2 = H_0\, a^2 \left[1 - \frac{2}{(\zeta + 1)} \right] \tag{4.4}$$

and

$$c_3 = \frac{2H_0}{\zeta + 1}. \tag{4.5}$$

The numerical method employed in this work does not allow the application of boundary conditions at the infinity, as prescribed for the problem. Therefore, the domain should be large enough in order to settle this condition. In view of that, we will proceed with two distinct investigations. First, how the numerical solution approaches the analytical one as a function of the domain size, then the method convergence for such a given domain size. This study is done evaluating the magnetic field at the center of the droplet. According to the analytical solution, the magnetic field inside the droplet for $\zeta = 2$ must be homogeneous and equal to $2H_0/3$. For every result here presented, the domain is square with side L, the droplet of radius $a = 1$ is located at the center of the domain and the external magnetic field points in the horizontal direction.

Figure 15 presents the relative numerical error computed for the magnetic field at the center of the droplet in function of the domain size, setting $h = 0.04$.

As shown in the Fig. 15, the bigger the domain, more accurate the numerical solution. This fact occurs due to the influence of the magnetizable droplet on the magnetic field close to it. For the analytical solution, the boundary conditions are applied at an infinite distance from the droplet. Since this condition is not applicable in the present methodology, we set this external field condition at the domain boundaries. The larger
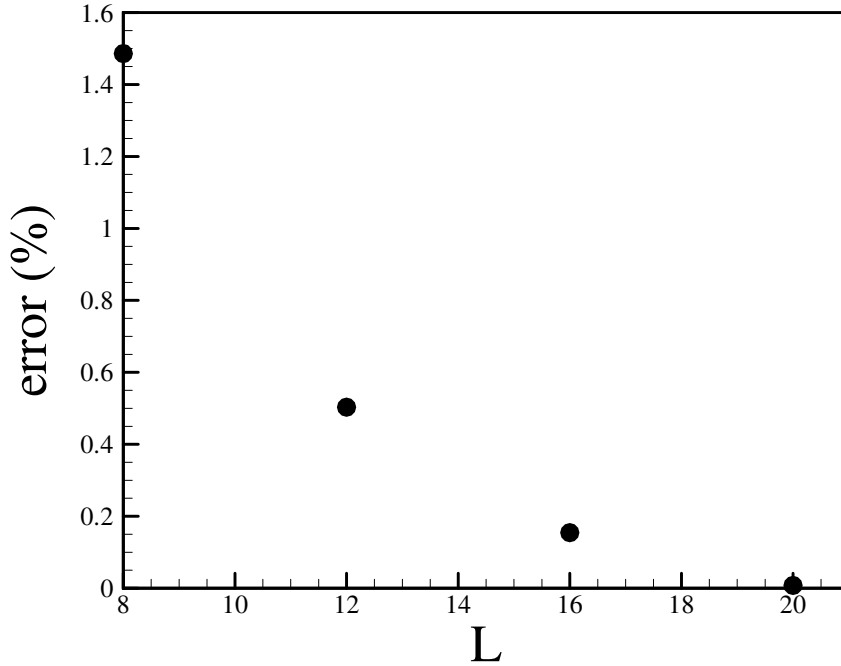
Figure 15 – Magnetite field relative error at the center of the droplet as a function of the size of the square domain side, L, for $a = 1$, $\zeta = 2$, $h = 0.04$ and $\boldsymbol{H} = H_0 \hat{e}_x$.

the domain, larger the distance between the droplet and the domain boundaries, bringing the numerical solution closer to the analytical one. Therefore, we conclude that our methodology recovers the analytical solution inside the droplet.

Figure 16 presents the relative numerical error computed for the magnetic field at the center of the droplet in function of the mesh refinement, $N_x = N_y = N$, setting $L = 20$. As refined is the mesh, smaller it is the relative error, varying from 0.946% for $N = 100$ to 0.008% for $N = 500$. Through this results, we can conclude that the method for the computation of the magnetic field converges with the mesh refinement.

For a clear comparison, Fig. 17 brings the analytical and numerical solutions for the magnetic field, respectively, the half above and the half below. The simulation was performed for $\zeta = 2.0$, $a = 1$ and $\boldsymbol{H}_0 = H_0 \hat{e}_x$ in a square domain with side $L = 12$ and mesh refinement of $N_x = N_y =$256. Also, Fig. 18 presents the numerical error evaluated all over the domain, for this very same case, excluding regions where the Heaviside function is not null, i.e. in the artificial fluids interface. The computed highest error for $|\boldsymbol{H}|$ was 1.356%. In conclusion, the numerical methodology is well computing the potential field.
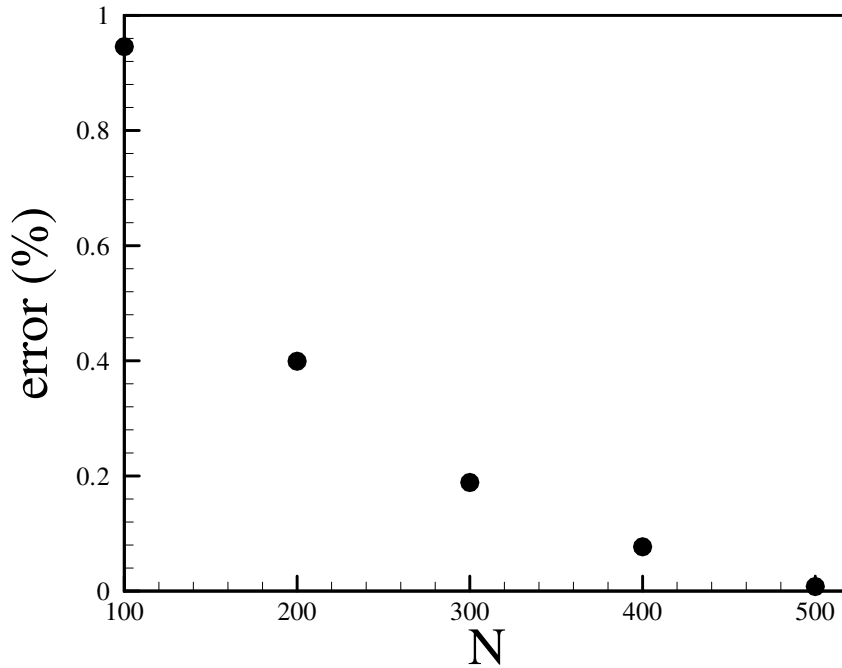
Figure 16 – Magnetite field relative error at the center of the droplet as a function of the mesh refinement, $N_x = N_y = N$, for $a = 1$, $\zeta = 2$, $L = 20$ and $\boldsymbol{H} = H_0 \hat{e}_x$.
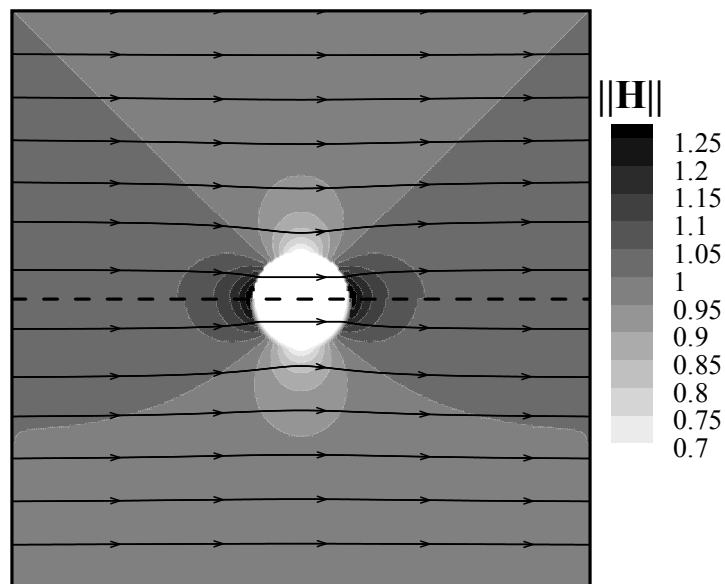
Figure 17 – Analytical (half above) and numerical (half below) solutions for the magnetic field, for $\zeta = 2.0$, $a = 1$, $\boldsymbol{H}_0 = H_0 \hat{e}_x$ and $L = 12$ with mesh refinement of $N_x = N_y = 256$.
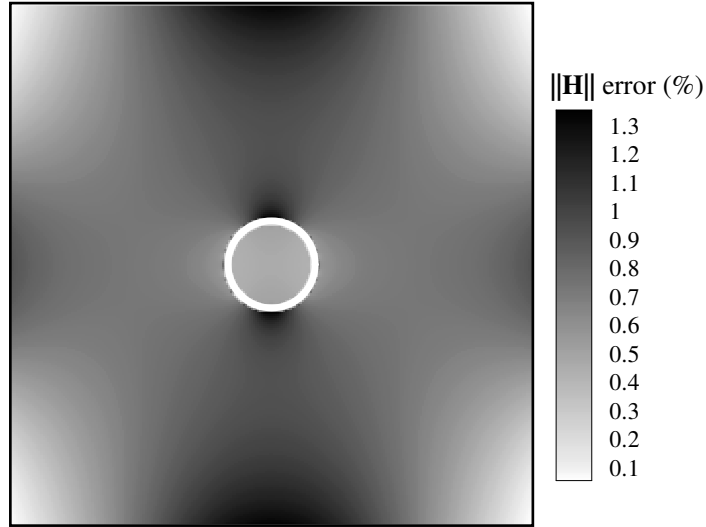
Figure 18 – Magnetic field numerical error for the magnetic field, setting $\zeta = 2.0$, $a = 1$, $\boldsymbol{H}_0 = H_0 \hat{e}_x$ and $L = 12$ with mesh refinement of $N_x = N_y = 256$.

4.2 Magnetic droplet deformation in a uniform magnetic field

In this section, it is considered the effect of a uniform magnetic field on the equilibrium shape of a ferrofluid droplet in the absence of an external flow. Due to a magnetic stress jump across the drop interface, which is consequence of a discontinuity on the magnetic field between the phases, the equilibrium shape is dictated by the balance between magnetic and capillary forces, being usually not spherical (Flament et al., 1996; Afkhami et al., 2010; Zakinyan & Dikansky, 2011; Rowghanian et al., 2016). For instance, Flament et al. (1996) used a Hele-Shaw cell to analyze a ferrofluid droplet subjected to a uniform magnetic field tangential to the walls. In this situation, it was found that the droplet equilibrium shape is approximately ellipsoidal. Here, we investigate the same static problem and characterize the ellipsoidal equilibrium shape by using a form factor e that is defined as the ratio between the shortest and the longest axis of the ellipsoidal droplet. Figure 19 compares the numerical predictions with the experimental results of Flament et al. (1996) in terms of e as a function of Ca_{mag}. The simulations were performed for a droplet of unitary radius, with $\lambda = 1$ and $\zeta = 3.2$ in a square domain with side $L = 12$ discretized with $N_x = N_y = 256$. Also, Fig. 20 compares the droplet equilibrium shape with the experimental visualizations. As can be seen, the numerical results agree well with

the experimental observations in both cases, leading to the conclusion that the magnetic and capillary forces at the interface are both being well computed.
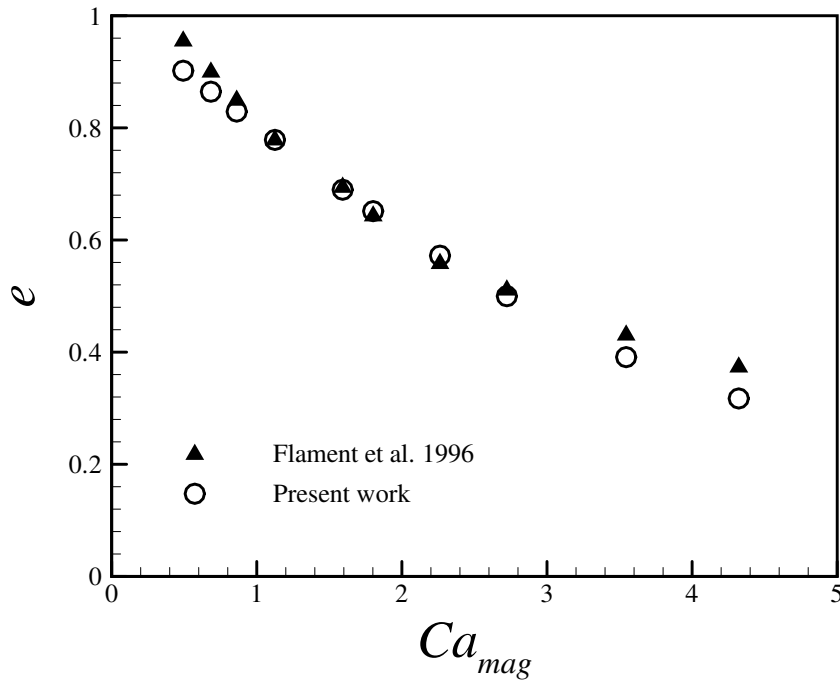
Figure 19 – Comparison with Flament et al. (1996) for the ellipsoidal form factor, e, as a function of magnetic capillary number, Ca_{mag}. Simulations performed with $\lambda = 1$ and $\zeta = 3.2$.
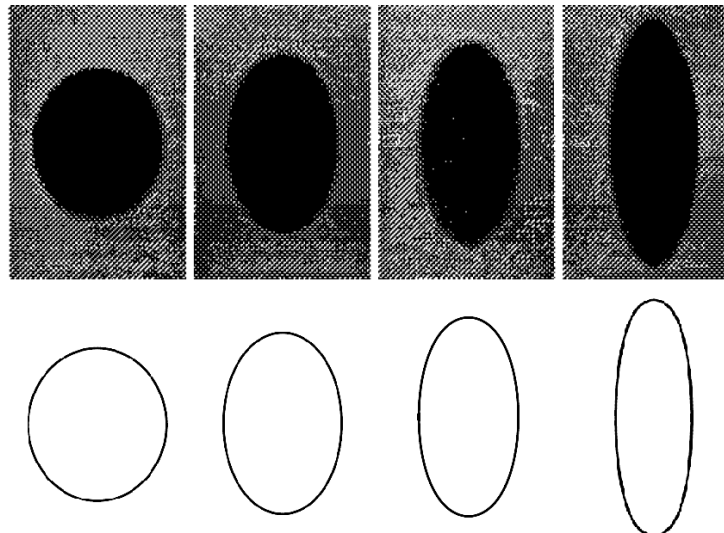
Figure 20 – Comparison with Flament et al. (1996) for the droplet equilibrium shape at, from the left to the right, $Ca_{mag} = 0.5$, 1.8, 2.7 and 4.3. Experimental visualization taken from Flament et al. (1996) in the upper row and numerically obtained in the present work in the bottom row. Simulations performed for $\lambda = 1$ and $\zeta = 3.2$.

4.3 Droplet inclination and rheology in shear flow

Still with the intention of validating the present formulation, we do a study on the behavior of a droplet undergoing a simple shear flow in the absence of an external magnetic field. Subjected to simple shear flows, droplets elongate and rotate. These movements are resultant from the action of the two components of this flow, extensional and rotational. Usually, the major axis of the deformed drop is not aligned with the flow. Actually, this inclination angle is determined by the balance of torques from the two cited components. The more viscous the drop, more aligned to the flow is the the major axis of the deformed drop, once the increasing in the viscosity reduces the extensional effects (Vlahovska, 2011).

In the limit of small capillary numbers, Taylor (1934) demonstrates that the droplet must present an inclination of 45° with the flow. In order to reproduce this theoretical limit, simulations were conducted considering each time smaller values of Ca for a droplet of $\lambda = 1$ in a shear flow, setting $Re = 10^{-2}$, a square domain of side $L = 12$ and a mesh refinement of $N_x = N_y = 400$. The small value set to the Reynolds number aims to recover the mechanical behavior of drops in the Stokes regime, the one considered by Taylor. In Fig. 21 it is possible to notice that the droplet inclination approaches 45° for the limit of Ca going to zero, recovering the Taylor's theoretical and experimental prediction.

Next, we proceed with the reproduction of the two-dimensional numerical study conducted by Ghigliotti et al. (2010), analyzing the droplet inclination and rheology in function of viscosity ratio, λ, when subjected to a simple shear flow considering the Stokes regime. Comparisons between the results of both studies are presented as follows. Figure 22 shows the droplet inclination, in degrees, with respect to the flow direction, θ, as a function of λ. The simulations were performed with $Re = 10^{-2}$ and $Ca = 0.3$ in a square domain with side $L = 12$ discretized with $N_x = N_y = 256$. Also, Fig. 23 presents the reduced viscosity, $[\eta]$, as a function of λ. Finally, Fig. 24 displays the droplet equilibrium shape and velocity vector field for $\lambda = 2$. These results show that the here produced predictions are in considerable agreement with the ones presented by Ghigliotti et al. (2010), despite the fact of using a different numerical method and solving the full Navier-Stokes equations.
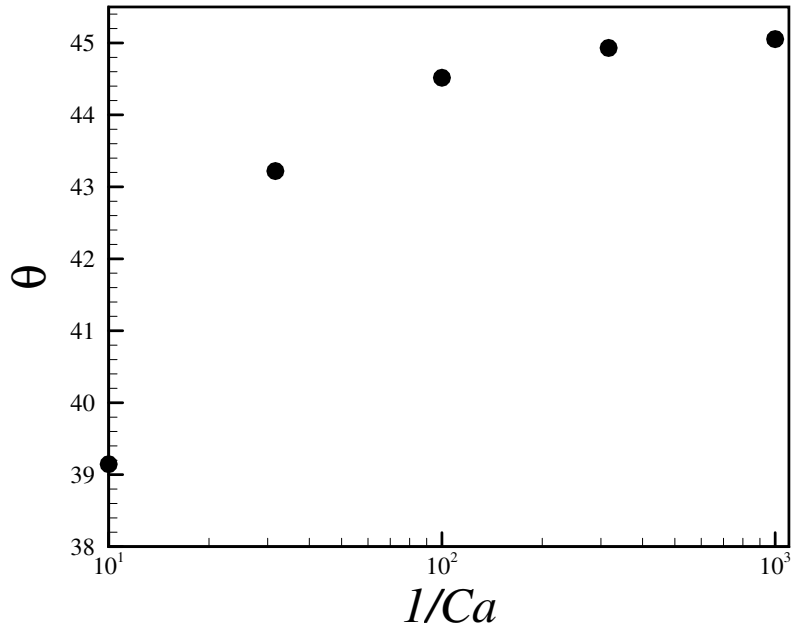
Figure 21 – Inclination measured in degrees, θ, for a droplet in a shear flow as a function of $1/Ca$, for $Re = 10^{-2}$ and $\lambda = 1$, considering a square domain of side $L = 12$ and mesh refinement of $N_x = N_y = 400$.
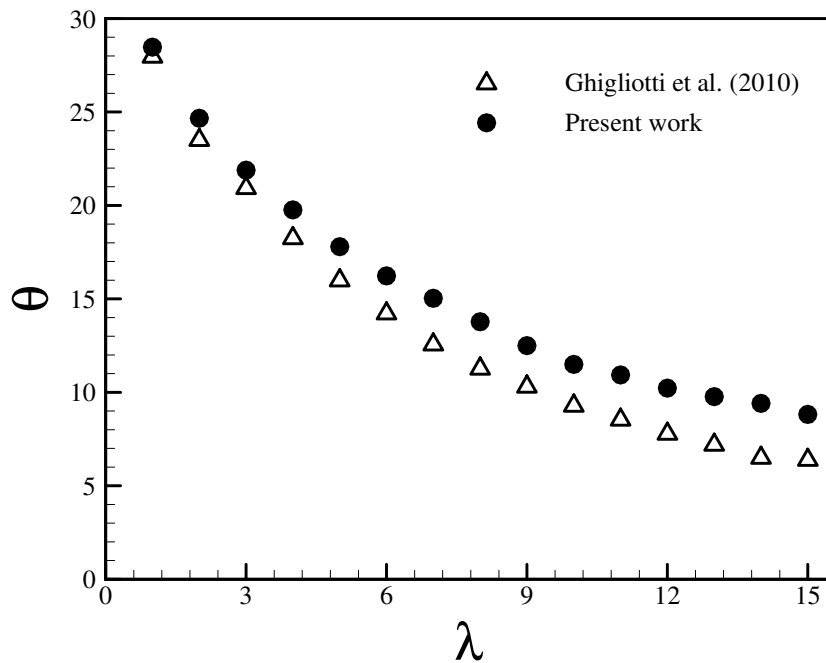
Figure 22 – Comparison with the work of Ghigliotti et al. (2010): droplet inclination in degrees, θ, as a function of the viscosity ratio, λ. Simulations performed with $Re = 10^{-2}$ and $Ca = 0.3$.
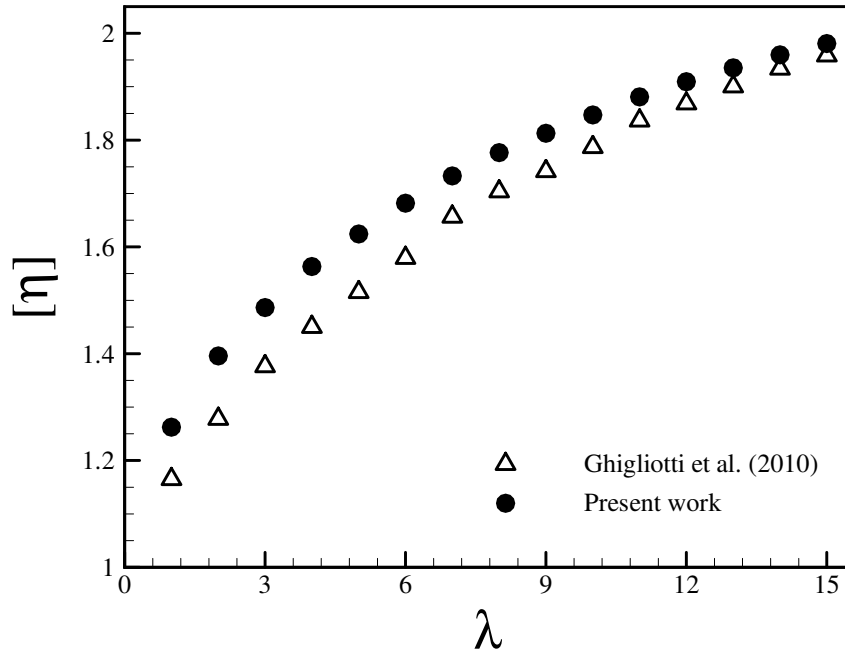
Figure 23 – Comparison with the work of Ghigliotti et al. (2010): reduced viscosity, $[\eta]$, as a function of the viscosity ratio, λ. Simulations performed with $Re = 10^{-2}$ and $Ca = 0.3$.
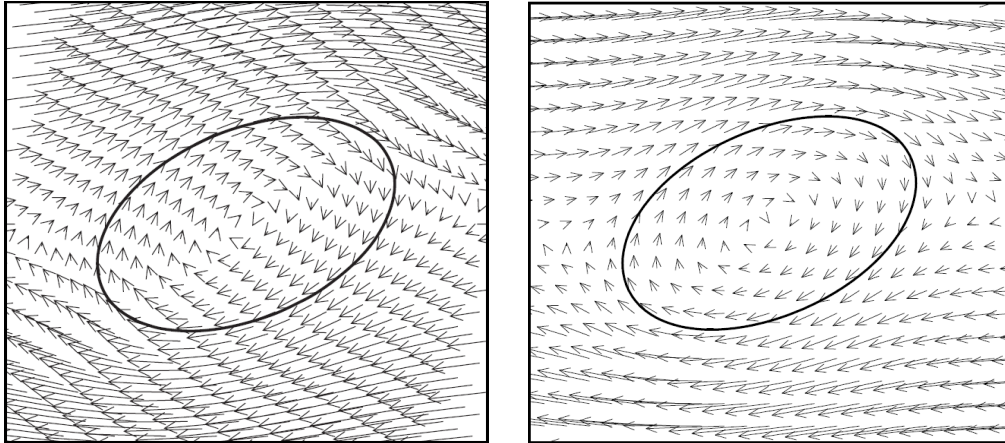
Figure 24 – Comparison with the work of Ghigliotti et al. (2010) (on the left): equilibrium droplet shape and velocity vector field. Simulations performed with $Re = 10^{-2}$, $Ca = 0.3$, and $\lambda = 2$.

4.4   Numerical order of the method

In order to verify the method convergence and perform a numerical resolution study, the case of a magnetic droplet subject to a simple shear flow and an external magnetic field perpendicular to the flow was done using different domain discretizations, $N_x = N_y = N$. The simulations were performed for $Re = 10^{-2}$, $Ca = 0.1$, $Ca_{mag} = 10$,

$\lambda = 2$ and $\zeta = 2$ in a square domain with side $L = 12$ during a period of time $t = 1.3$. Table 1 presents the droplet inclination, reduced viscosity and velocity in the horizontal direction at the position $\boldsymbol{x} = (3, 3)$ computed with four distinct meshes. It was found that the variation from the mesh $N = 300$ to $N = 400$ was 0.4% for the reduced viscosity and 0.06% for the drop inclination, while from $N = 200$ to $N = 300$ the reduced viscosity varied 1.13% and the drop inclination varied 0.17%. From these results, it is concluded that the numerical approach used in this work is consistent and presents an order ≈ 1.7 in relation to the cell size, h.

Table 1 – Computed droplet inclination in degrees, θ, and reduced viscosity, $[\eta]$, with different mesh discretizations for a droplet immersed in a simple shear flow and uniform magnetic field, setting $Re = 10^{-2}$, $Ca = 0.1$, $Ca_{mag} = 10$, $\lambda = 2$, $\zeta = 2$, $L = 12$ and $t = 1.3$.

N	θ	$[\eta]$	$u(3,3)$
100	77.1458	4.4197	2.69894
200	77.6010	4.6397	2.67697
400	77.7762	4.7115	2.67034

5 Results and discussions

In this chapter we studied the influence of external magnetic fields on the droplets inclination, magnetic emulsion viscosity and the process of droplets ruptures when submitted to shear flows. The results and discussions are organized in two sections. In the first, the investigation on control of the droplet inclination and emulsion viscosity by means of external magnetic fields is done by varying the applied magnetic field for a given case. Secondly, the induction of topological transformations is analyzed considering cases in which the drop breakup happens and does not happen in absence of external fields.

5.1 Droplet inclination and emulsion viscosity

In absence of flows, magnetic droplets elongates in the direction of external magnetic fields (see section 4.2). This effect may be used to control the inclination of drops in shear flows, inducing them to get more or less aligned with the flow and, also, modifying their geometry. Once these parameters are directly related to the emulsion effective viscosity, they lead us to think about the possibility of controlling the rheology of a magnetic emulsion by means of external fields. For instance, recent works have addressed this fact for emulsions of drops that undergo small deformations induced by external electrical fields (Vlahovska, 2011; Mandal & Chakraborty, 2017a). Here, we will proceed with numerical investigations on the external magnetic fields influence on the droplets inclination and emulsion viscosity, both considering a single droplet in a simple shear flow imposed by parallel plates.

The procedure used in this analysis consists in running simulations for a given case, varying Ca_{mag} for the magnetic field applied parallel and perpendicular to the flow, and measuring the droplet inclination in relation to the flow and the reduced viscosity once reached the steady state. For each case, the simulation is run in absence of magnetic fields until the droplet achieves an equilibrium shape, only then the magnetic field is turned on, computing the inclination and reduced viscosity at the steady state. All simulations were performed with $a = 1$, $Re = 10^{-2}$, $Ca = 0.1$, $\lambda = 2$, and $\zeta = 2$ in a square domain

with side $L = 12$ discretized with $N_x = N_y = 400$. At this condition and in absence of magnetic field, $\theta = 36.8°$, $[\eta] = 1.66$, and the the droplet does not breakup in the flow.
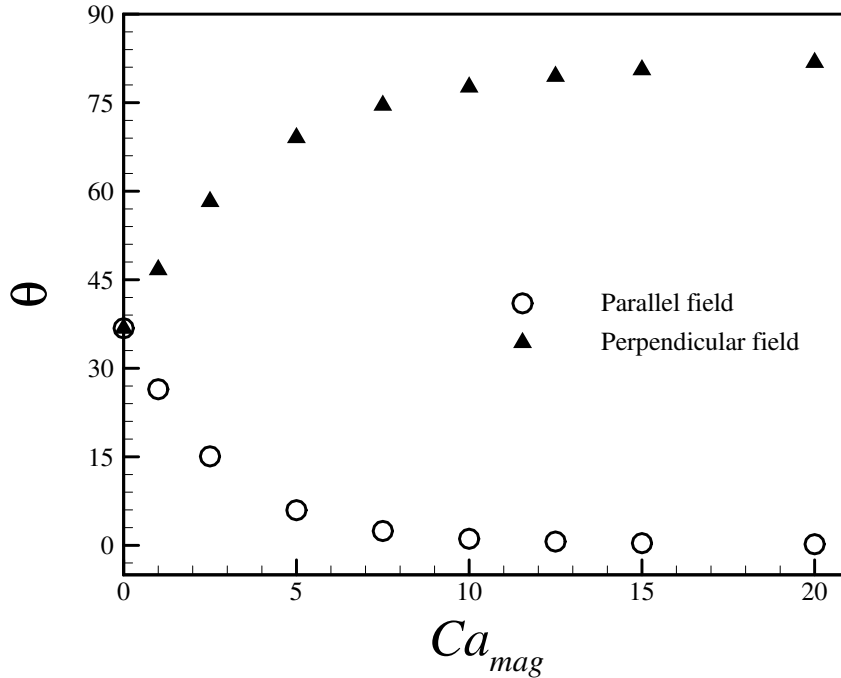
Figure 25 – Droplet inclination in degrees, θ, as a function of the magnetic capillary number, Ca_{mag}. Simulations for $Re = 10^{-2}$, $Ca = 0.1$, $\lambda = 2$, and $\zeta = 2$.

Figures 25 and 26 show how the droplet inclination and reduced viscosity change with the magnetic field intensity in terms of θ and $[\eta]$ as a function of Ca_{mag}, respectively. The induced alignment with the magnetic field direction gets stronger as the field intensity increases. When the field is parallel to the flow direction, θ decreases with Ca_{mag}, tending asymptotically to zero at high enough Ca_{mag}. As the droplet gets more aligned with the flow, it becomes easier to the streamlines to go around the particle surface, which decreases the reduced viscosity. As a consequence, $[\eta]$ falls with Ca_{mag}. For instance, $[\eta] = 0.62$ and $\theta = 0.18°$ at $Ca_{mag} = 20$. In turn, when the external field is perpendicular to the flow direction, θ increases with Ca_{mag}. In this case, there is a competition between shear and magnetic forces. On the one hand, the magnetic field stretches the droplet in the vertical direction. However, it increases the torque caused by the shear flow, which acts in order to rotate the droplet back to the horizontal direction. The final equilibrium position depends on the balance between these two effects. The misalignment with the flow requires that the streamlines deflect to contour the droplet shape, which increases the reduced viscosity. Therefore, $[\eta]$ strongly increases with Ca_{mag}. At $Ca_{mag} = 20$, it is found $\theta = 81.8°$ and
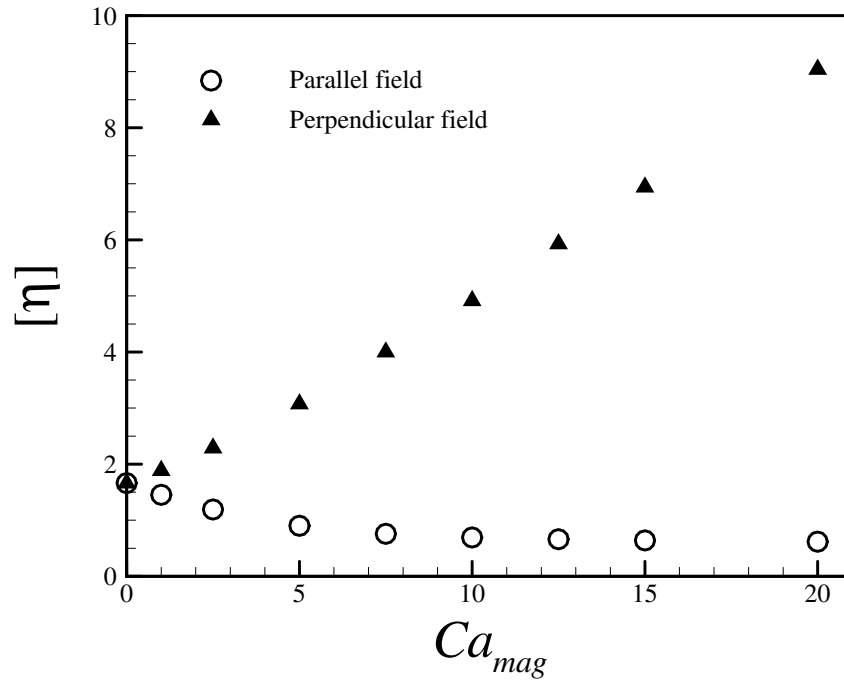
Figure 26 – Reduced viscosity, $[\eta]$, as a function of the magnetic capillary number, Ca_{mag}. Simulations for $Re = 10^{-2}$, $Ca = 0.1$, $\lambda = 2$, and $\zeta = 2$.

$[\eta] = 9.04$, which indicates that the external magnetic field increases the emulsion viscosity in one order of magnitude. This analysis is confirmed by Figs. 27 and 28, which display the evolution of the droplet equilibrium shape with the magnetic capillary number and the behavior of the streamlines and horizontal velocity field at $Ca_{mag} = 10$.
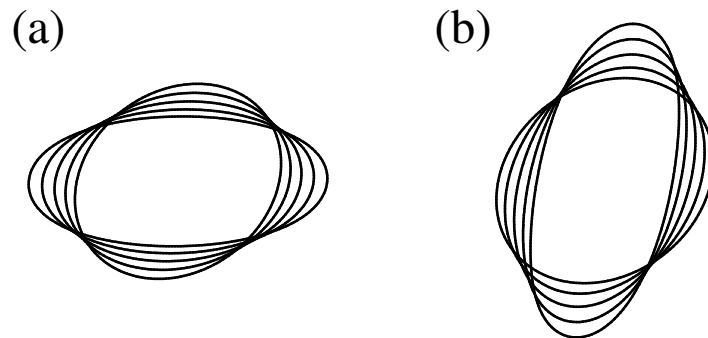
Figure 27 – Droplet equilibrium shape for $Ca_{mag} = 0, 2.5, 5, 7.5$, and 10: (a) magnetic field parallel to the flow direction; and (b) magnetic field perpendicular to the flow direction.
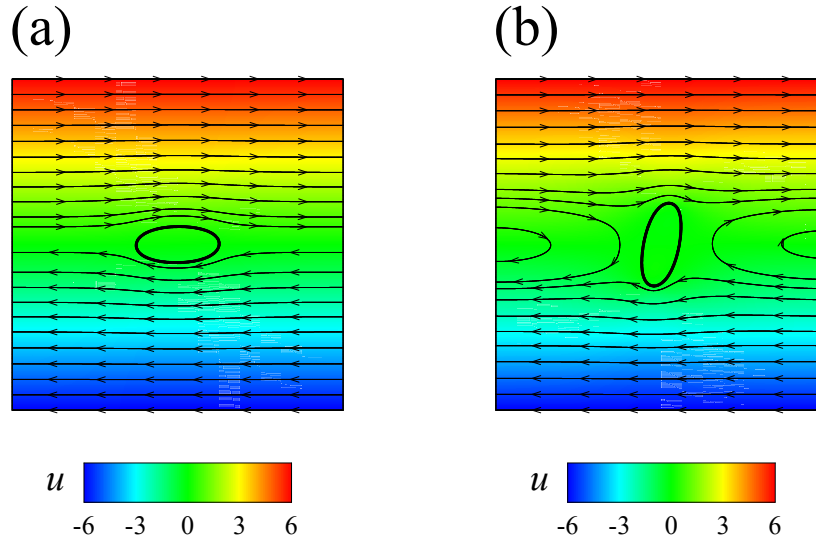
Figure 28 – Streamlines and horizontal velocity field at $Ca_{mag} = 10$: (a) magnetic field parallel to the flow direction; and (b) magnetic field perpendicular to the flow direction.

5.2 Droplet breakup process

Here, it is analyzed how topological transformations on magnetic droplet in shear flows can be influenced by the action of external magnetic fields, inducing or avoiding breakups. Unless it is stated the contrary, all results presented in this section were obtained with $a = 1$, $Re = 1$, $Ca = 0.5$, $\lambda = 1.2$, and $\zeta = 2$ in a rectangular domain of dimensions 12×6 discretized with $N_x = 300$ and $N_y = 150$. For this set of parameters, the droplet breaks in the absence of external magnetic field ($Ca_{mag} = 0$), as shown in Fig. 29. The balance between shear and capillary forces drastically changes the droplet shape and ultimately leads to the droplet breakup. Notice that the rupture of the original drop results in three new daughter drops. The central, smallest daughter drop is also known as satellite drop, being common in drop breakup process. The narrow region observed in Fig. 29 for $t = 22.52$ is here refereed as neck and contains the portion of fluid which will originate the satellite drops.

The effect of the magnetic field on the breakup process was analyzed by increasing the magnetic field intensity in terms of the magnetic capillary number. The evolution

of the droplet shape under the simultaneous action of shear flow and magnetic field for $Ca_{mag} = 2$, 4, 8, and 12 is reported in Figs. 30 - 33, where it is considered magnetic fields parallel to the flow direction.
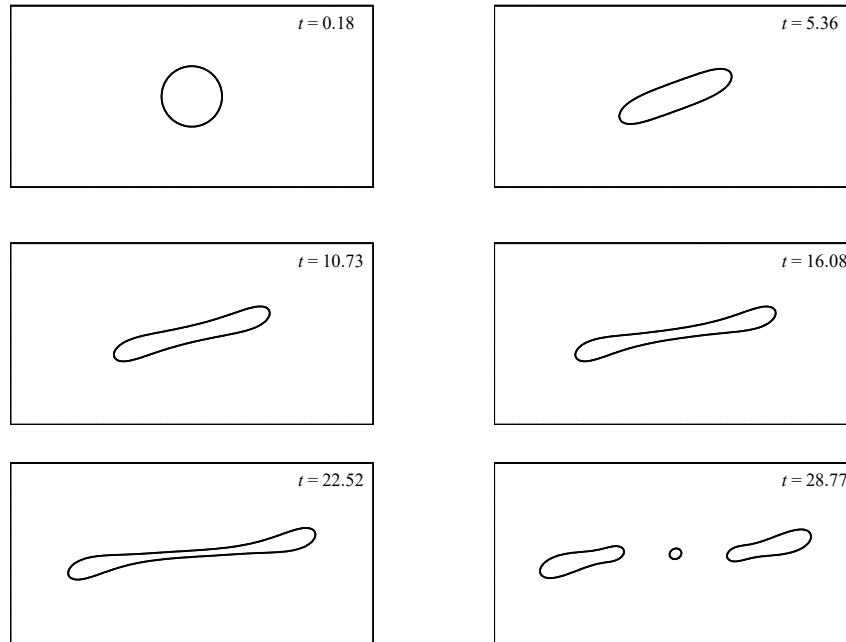
Figure 29 – Evolution of the droplet shape in the absence of external magnetic field.
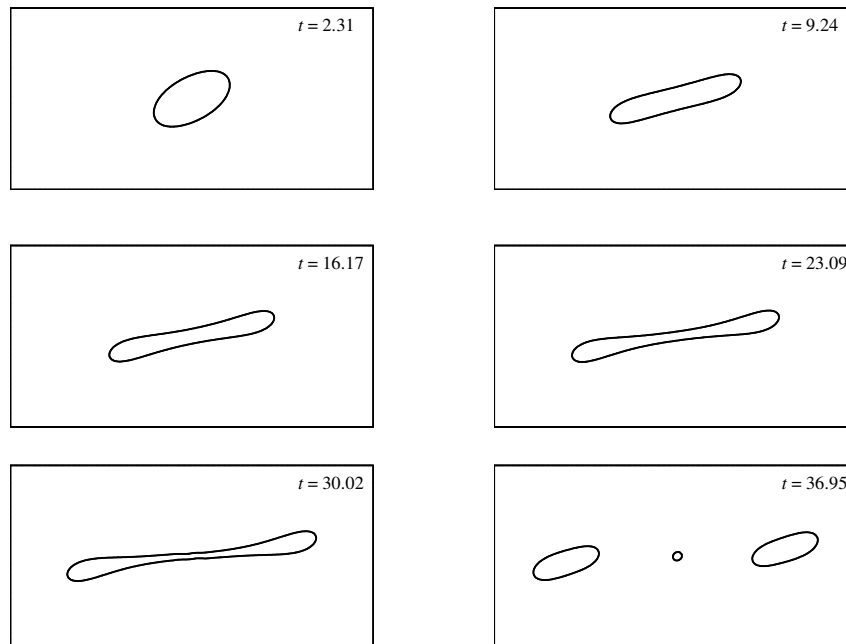
Figure 30 – Evolution of the droplet shape under the action of external magnetic field parallel to the flow direction with $Ca_{mag} = 2$.
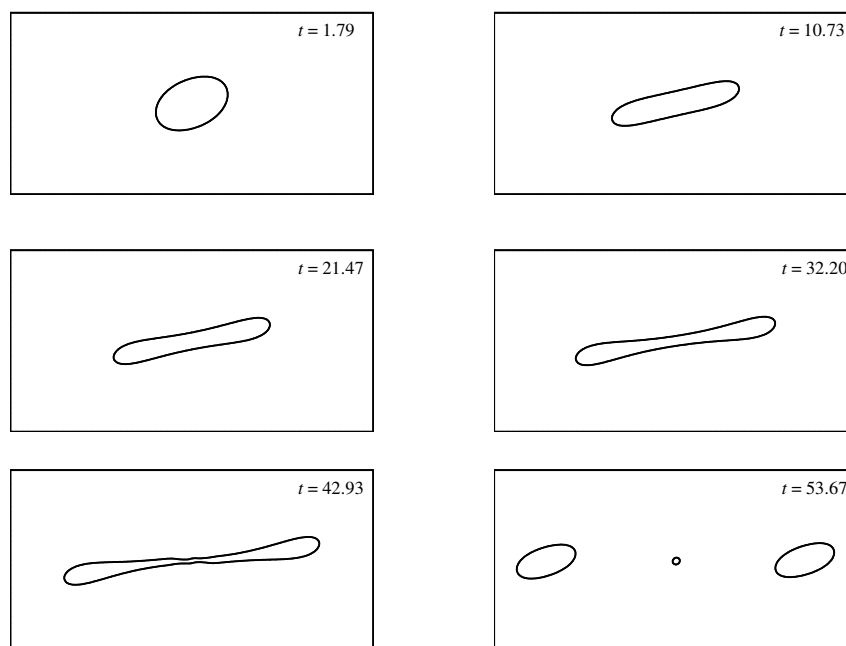
Figure 31 – Evolution of the droplet shape under the action of external magnetic field parallel to the flow direction with $Ca_{mag} = 4$.
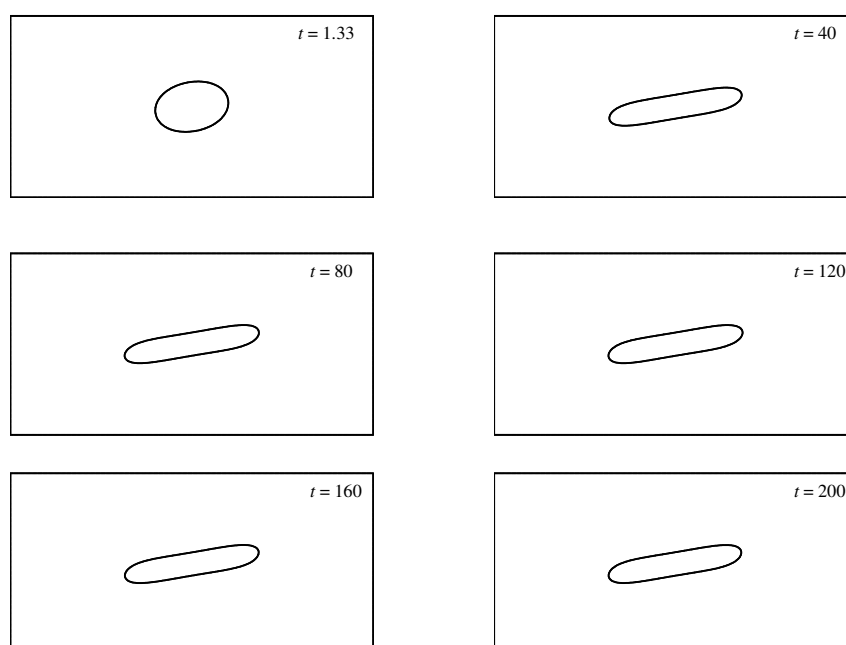
Figure 32 – Evolution of the droplet shape under the action of external magnetic field parallel to the flow direction with $Ca_{mag} = 8$.
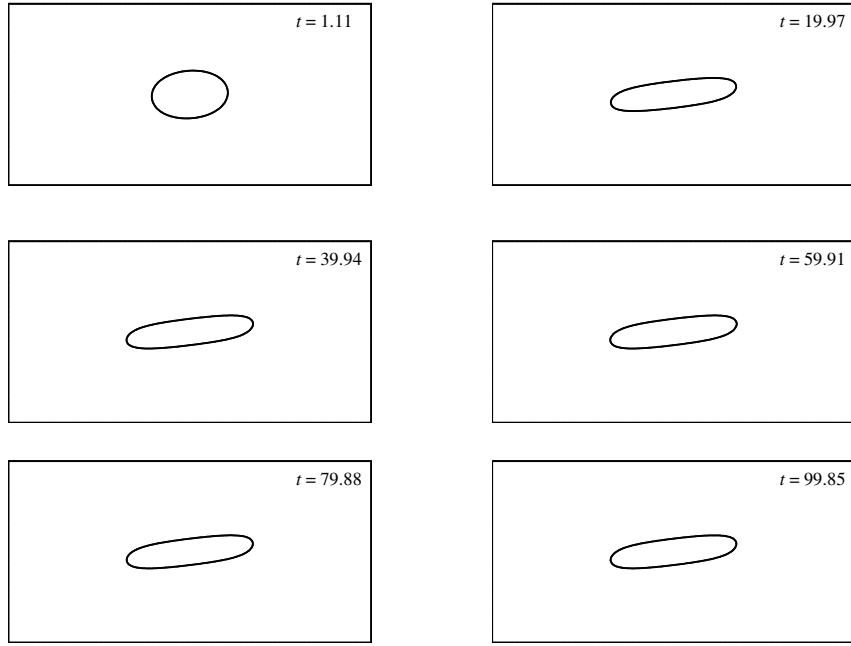
Figure 33 – Evolution of the droplet shape under the action of external magnetic field parallel to the flow direction with $Ca_{mag} = 12$.

When the applied magnetic field is parallel to the flow direction, increasing the magnetic field intensity postpones and even avoids the droplet rupture process. In Fig. 34, it is presented the time until the rupture as a function of Ca_{mag}^{-1}, which shows that the time to breakup increases with magnetic field intensity. Also, there is a critical magnetic capillary number Ca_{mag}^* above which the time to rupture tends to infinite, thus the droplet should not break. A power law fitting suggests that $Ca_{mag}^* = 6.7$ and the time to breakup scales as $\sim (Ca_{mag}^{-1} - Ca_{mag}^{*-1})^{-1/4}$. Also, it is verified that, for $0 < Ca_{mag} < Ca_{mag}^*$, the size of the satellite drop after the rupture decreases with Ca_{mag}. Figure. 35 shows the relative size of the satellite droplet with respect to the size of the original drop as a function of Ca_{mag}^{-1} and suggests that it scales as $\sim (Ca_{mag}^{-1} - Ca_{mag}^{*-1})^{1/3}$. It happens because stronger magnetic fields increase the droplet extension in the flow direction before the rupture, reducing the amount of liquid in the neck. This result indicates that the size of the satellite droplet is zero for $Ca_{mag} = Ca_{mag}^*$, suggesting no rupture for such case once again. In fact, it is observed the rupture for $Ca_{mag} = 2$ and $Ca_{mag} = 4$ in Figs. 30 and 31, but it is not verified for $Ca_{mag} = 8$ and $Ca_{mag} = 12$ in Figs. 32 and 33. For $Ca_{mag} > Ca_{mag}^*$, the droplet is so aligned with the flow direction that the resulting shear force acting on its surface is not strong enough to induce the rupture process.
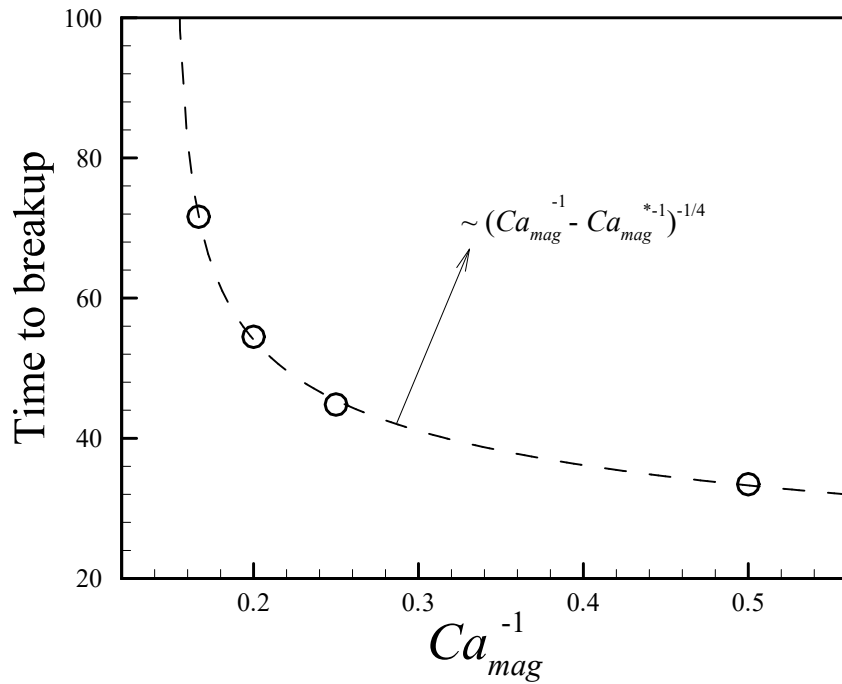
Figure 34 – Time to droplet breakup as a function of Ca_{mag}^{-1}, for the magnetic filed parallel to the flow.
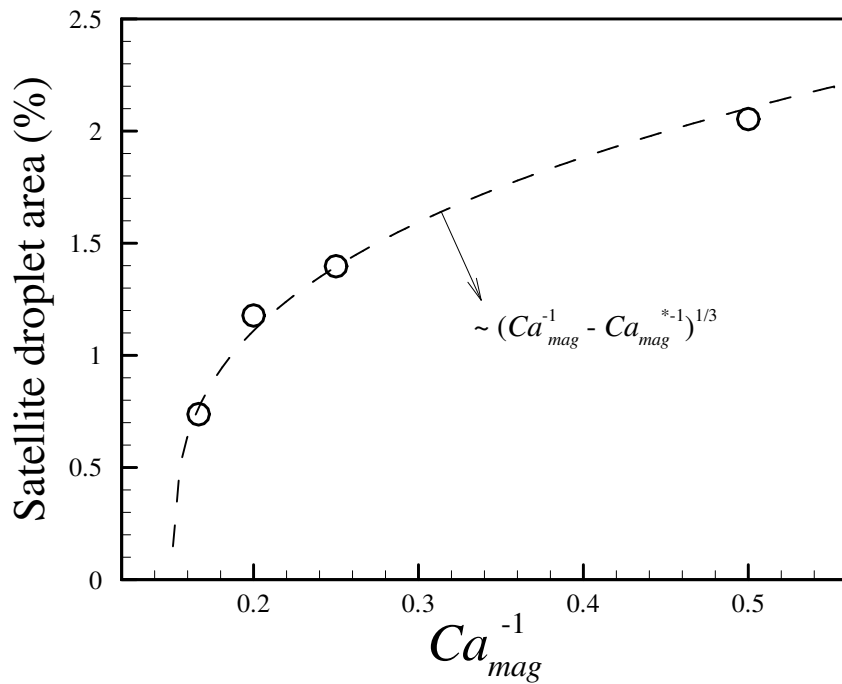
Figure 35 – Area of the satellite drop relative to the original drop as a function of Ca_{mag}^{-1}, for the magnetic filed parallel to the flow.

A very different behavior happens when the magnetic field is applied perpendicularly to the flow direction, as reported in Figs. 36 - 39 for $Ca_{mag} = 2$, 4, 8, and 12.
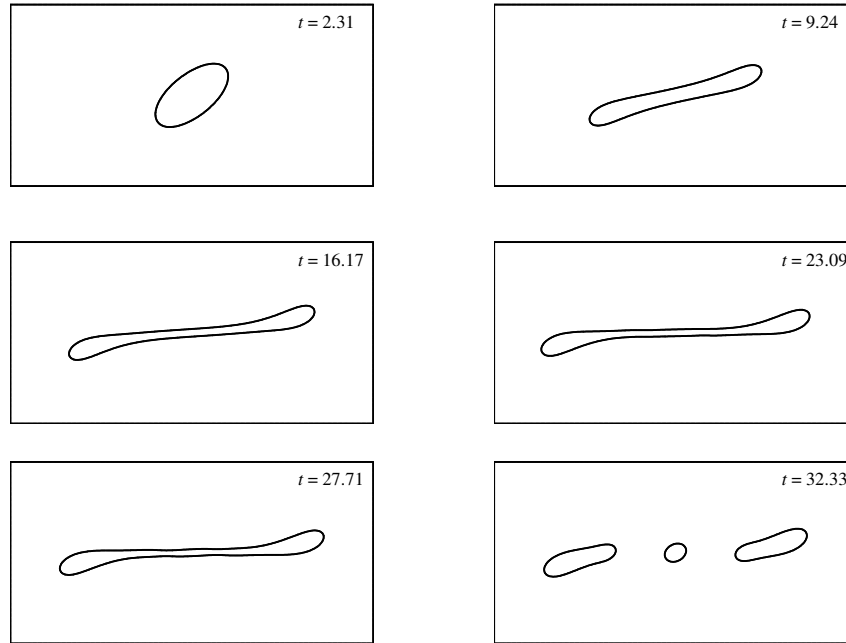
Figure 36 – Evolution of the droplet shape under the action of external magnetic field perpendicular to the flow direction with $Ca_{mag} = 2$.
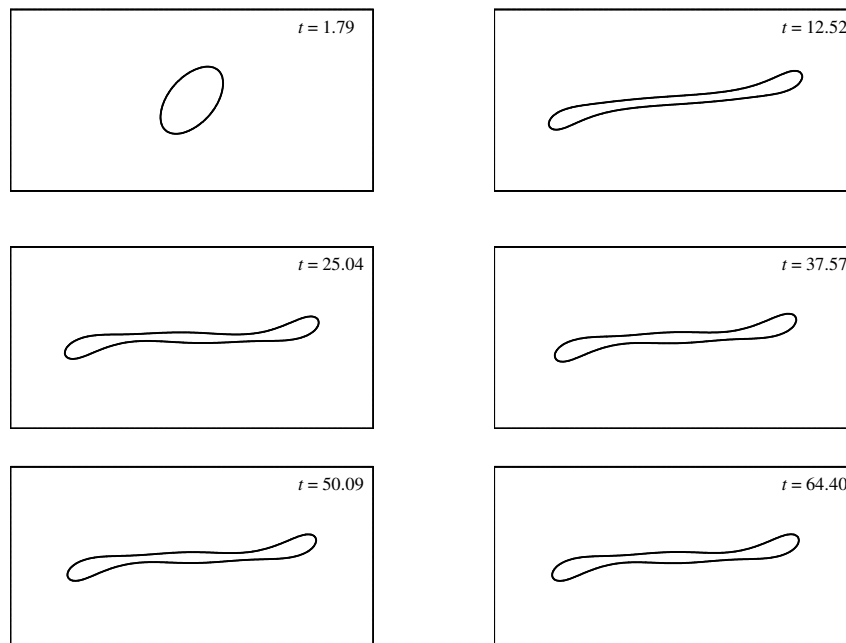
Figure 37 – Evolution of the droplet shape under the action of external magnetic field perpendicular to the flow direction with $Ca_{mag} = 4$.
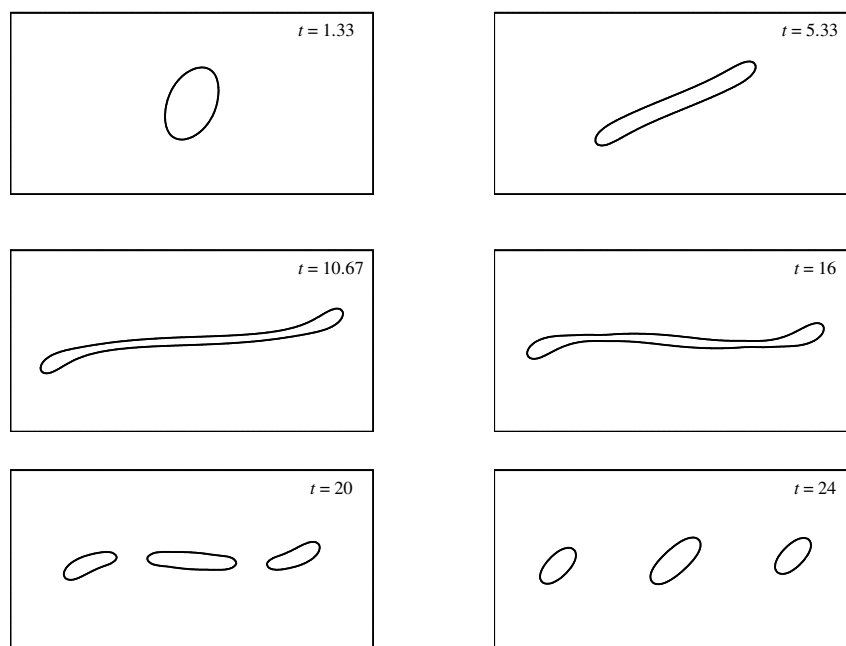
Figure 38 – Evolution of the droplet shape under the action of external magnetic field perpendicular to the flow direction with $Ca_{mag} = 8$.
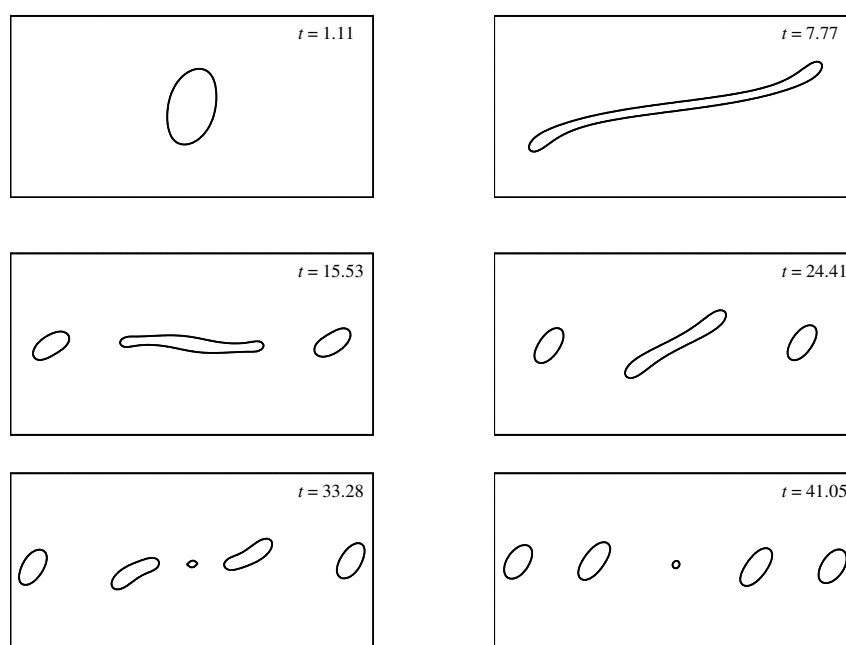
Figure 39 – Evolution of the droplet shape under the action of external magnetic field perpendicular to the flow direction with $Ca_{mag} = 12$.

For instance, at $Ca_{mag} = 2$, the time to rupture and the size of the satellite drop increases when compared to the situation when there is no external magnetic field, as shown in Fig. 36. At an intermediate range, the magnetic field avoids the breakup, such that the droplet remains with a stable shape similar to the one presented in Fig. 37 for $Ca_{mag} = 4$. At even higher magnetic capillary number, the rupture happens again, and the time to breakup decreases while the size of the satellite drop increases with Ca_{mag}. This is reported in Figs. 38 and 39 for $Ca_{mag} = 8$ and $Ca_{mag} = 12$. This behavior is a consequence of a competition between magnetic and shear effects. On the one hand, the magnetic field stretches the droplet in the direction perpendicular to the flow direction, which intensifies the shear effects over the surface that lead to the breakup. In turn, it also increases the amount of liquid in the neck of the deformed droplet, which acts against the rupture process.

Finally, it is also considered the effect of an external magnetic field on the breakup process when the droplet does not break under the flow action only. As a matter of fact, this happens for $Re = 10^{-1}$, $Ca = 0.3$, $\lambda = 1.2$, and $\zeta = 2$. For this set of parameters, we considered magnetic fields parallel and perpendicular to the flow direction with $Ca_{mag} = 1$, 10, and 20. Among the six cases, we verified that the rupture occurs when the field is perpendicular to the flow direction with $Ca_{mag} = 20$. The evolution of the droplet shape in this case is shown in Fig. 40. This result indicates that external magnetic fields can also be used to induce the rupture process when the shear flow is not strong enough to do so.
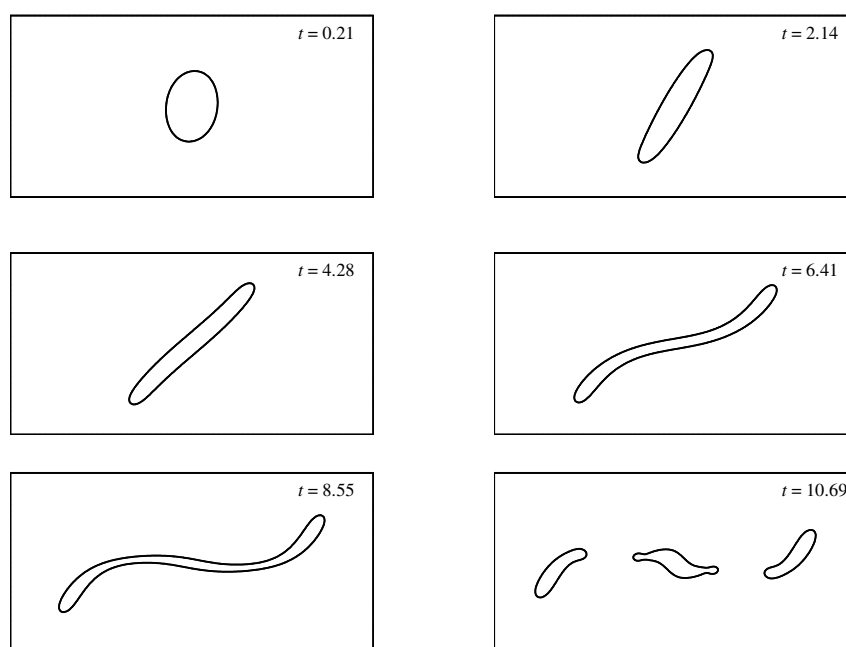
Figure 40 – Evolution of the droplet shape under the action of external magnetic field perpendicular to the flow direction with $Ca_{mag} = 20$. Simulations for $Re = 10^{-1}$, $Ca = 0.3$, $\lambda = 1.2$, and $\zeta = 2$.

6 Final remarks

6.1 Conclusions

This work has analyzed the response of a planar ferrofluid droplet suspended in a non-magnetic liquid to the combined action of an external magnetic field and a simple shear flow, investigating the influence of the field on the droplet inclination, emulsion viscosity and droplet breakup, and how it can be used to externally control magnetic emulsions. Indeed, fundamental understanding in this regard is quite important for the improvement of already existing techniques and development of new methods using this modern class of complex fluids. Within this context, we developed a complete continuum mathematical model for the multiphase problem under analysis. Due to the absence of an electrical field and variations of the magnetic field with time, the Maxwell equations are reduced to the magnetostatic limit, allowing the magnetic field to be described by the gradient of a magnetic potential field and guaranteeing the continuity of the magnetic induction field. Under such considerations, the magnetic potential field becomes governed by the Laplace equation. The motion equations for a volume containing two fluids separated by an interface is detailed under the perspective of mass and momentum conservation (Unverdi & Tryggvason, 1992; Chang et al., 1996). Hydrodynamic and magnetic effects are coupled in the formulation by including magnetic field forces to the motion equations just mentioned. In this work, the ferrofluid droplet is considered neutrally buoyant, therefore gravitational forces are neglected. At this point, we already produced a mathematical formulation for the problem, however it presents discontinuities on the fluids properties, stress tensor and magnetic potential field across the fluids interface. In order to alleviate this condition, we use a signed distance function, here called Level-Set function, allowing us to smooth the interface and describe the problem as continuum. This is a scalar function which indicates the shortest distance between a given point of the domain and the front (i.e. fluids interface), and it is signed as negative if inside the droplet and positive if outside. Thus, we are capable of capture the front by computing where this function is

null. The droplet surface movement due to the flow is captured by advecting the Level-Set function with the flow, which must be solved together with a reinitialization scheme in order to keep it as the the signed distance function. Lastly, we end up with three different but related problems to be solved: the potential magnetic field, the Navier-Stokes equations considering magnetic and capillary forces and the evolution of the Level-Set function.

The numerical formulation proposed in this work is based on the Finite Difference method, the Projection method and the Level-Set method. The first problem to be solved in our numerical scheme is the potential magnetic field, which solution is obtained with the Finite Difference method. The governing equation of the magnetic potential field is not time dependent, thus its solution depends only on the instantaneous droplet shape and boundary conditions. Once the potential magnetic field is computed, we proceed with the solution of the Navier-Stokes equations considering magnetic and capillary forces, which is done using the Projection Method. The Projection Method is a popular numerical methodology for solving time-dependent incompressible viscous problems, based on decoupling the solutions of the velocity and pressure fields. The solutions of the differential equations for the velocity and pressure field are also solved via Finite Difference method. Finally, with the velocity field computed, we are able to work on the advection and reinitialization of the Level-Set function. Both of this equations are solved using the Total Variation Diminishing method. All these mentioned steps are repeated in a loop in order to evolve the simulation in time.

For the validation of the mathematical and numerical model, we studied four benchmark problems: the magnetic field for a disk immersed in an external uniform magnetic field, the deformation suffered by a ferrofluid droplet in a Hele-Shaw cell when submitted to an external magnetic field, the inclination of a droplet subjected to a shear flow in the limit of small capillary numbers and the rheology of a planar droplet in a shear flow. The good agreement obtained between the results produced in this work and the analytical, experimental and numerical ones available in the literature leads us to conclude that the presented methodology is in accordance with the physics of the problem, proving to be a reliable tool for the study under analysis in this work.

By the results produced in this work, we found that the magnetic force has a strong influence on the droplet inclination and emulsion rheology. Stronger it is the magnetic field,

more aligned to the field the droplet is. When the magnetic field is applied parallel to the flow, the droplet inclination in relation to the imposed velocity is reduced. Once the droplet gets more aligned with the flow, the deviation suffered by the velocity streamlines to contour the drop is alleviated, reducing the emulsion viscosity. Oppositely, for the magnetic field applied perpendicular to the flow, the droplet inclination gets higher, inducing a greater deviation of the velocity streamlines to contour the drop which increases the emulsion viscosity.

In relation to the rupture of droplets in shear flows, we found out that the magnetic effects can either induce and avoid the breakup process, as well control the time it takes and size ration of the daughters drops. First, it was analyzed a case in which the droplet breakup occurs in absence of external fields. It was observed that the application of external fields parallel to the flow increase the time for the breakup to occur and, also, reduces the size of the satellite daughter. The great alignment between droplet inclination and flow reduces the shear acting on the droplet making it difficult for the droplet to break, consequently retarding this phenomenon. If the magnetic field is too strong, the droplet gets so aligned to the flow that the shear is not capable of stretching and breaking the drop. It also occur that the elongation suffered by the drop in the direction of the magnetic field when applied parallel to the flow reduces the amount of fluid in the neck region, which originates the satellite drop. Therefore, case the drop breaks when the magnetic field is applied parallel to the flow, the resultant satellite droplet is smaller as strong is the magnetic field. When the external field is applied perpendicular to the flow, the amount of liquid in the neck region of the deformed drop is increased, making it more difficult for the rupture to occur, but resulting in bigger satellite daughters. However, the greater inclination makes the drop more susceptible to the shear flow action, assisting the breakup process. Finally, by analyzing a case in which the droplet breakup does not occurs in absence of external fields, it was verified that it is possible to induce the rupture of a droplet by applying the magnetic field perpendicular to the flow.

6.2   Future works

Since we are dealing with a relatively new class of complex fluids, there are, naturally, a great amount of lines of researches that must be explored from the studies

presented in this work. These studies are needed to build a solid comprehension on this field, which is fundamental for its implementation in the industry and people daily life. Some of these research lines are:

- Implement the computation of the Landau-Batchelor tensor by means of surface integrals to proceed with further rheological studies;

- Studies on the rheological responses of magnetic emulsions under the influence of magnetic fields and flows different to the one considered in the present work, such as oscillatory shear flows, extensional flows, step strain flow, among others;

- The implementation of the numerical methodology in three dimensions, aiming to explore all the physical mechanisms related to the problem. In this case, it will become possible to quantify the influence of the interaction between the magnetic field and the ferrofluid droplet on the viscosity of the magnetic emulsion. Also, the complete physics behind the droplet breakup will be able to be investigated, once the curvature in the third dimension will be included in the computation besides the effects of the third dimensional component of the flow. This advance may be challenging due to the great amount of computational effort related to the inclusion of another dimension;

- Modifications on the mathematical model in order to include the evolution of the magnetization existing out of the superparamagnetism regime. These modifications would consider situations in which the dipoles are misaligned with the magnetic field, carrying to variations on the ferrofluid droplet viscosity due to magnetic body torques in this fluid, which would directly affect the emulsion viscosity;

- The study of the interaction between two droplets in presence and absence of an imposed flow, in order to verify attractive and repulsive effects between the drops. These interactions are important in the determination of some macroscopic properties of the emulsion such as the rheology and concentration due to diffusive effects. This study may be also extended to the interaction between many droplets.

- Investigation on the influence of magnetic fields on the migration of droplets when subjected to shear gradients. This is an important study in engineering to verify and understand how external fields can be used to control the migration of droplets

and particles. In practice, this technique would be of great value for the coating area to better control the suspension concentration when applied over the surface, fundamental parameter in the quality of the final product. Also, it could be of interest in the drug targeting area by increasing or reducing the drug concentration close to the veins walls.

- Trajectory control of droplets in micro system by the application of magnetic fields gradients. Despite it is an already used technique in the field of lab-on-a-chip technologies, the literature presents a lack of numerical works in this matter. The use of numerical methodologies similar to the one here presented, would be a useful tool to conduct researches and build greater understanding about this technique.

- Further modifications on the mathematical and numerical modeling to study the interaction of magnetic vesicles with magnetic fields. Vesicles is a liquid drop enclosed by membrane suspended in a liquid medium, which are believed to represent an interest model system for studying viscoelastic properties of real cells and it is also used for the design of drug delivery vehicles. The application of magnetic vesicles in the drug industry is of great interest once it possibility to controlling the drug transport through the organism by means of external magnetic fields;

- Numerical investigation on the enhancement of heat transfer systems by magnetic forced convection using magnetic emulsions. Since the magnetization of ferrofluids decreases with the temperature, the colder magnetic drops would get more susceptible to magnetic conventions. In this sense, it becomes possible to control the convection effects in a system permitting the design of enhanced heat transfer system using magnetic emulsions.

References

Afkhami, S., Renardy, Y., Renardy, M., Riffle, J. S., & Pierre, T. G. S. (2008). Field-induced motion of ferrofluid droplets through immiscible viscous media. *Journal of Fluid Mechanics*, 610, 363–380.

Afkhami, S., Tyler, A. J., Renardy, Y., Renardy, M., Pierre, T. G. S., Woodward, R. C., & Riffle, J. S. (2010). Deformation of a hydrophobic ferrofluid droplet suspended in a viscous medium under uniform magnetic fields. *Journal of Fluid Mechanics*, 663, 358–384.

Allan, R. S. & Mason, S. G. (1962). Particle behaviour in shear and electric fields. I. deformation and burst of fluid drops. *Proc. R. Soc. Lond. A*, 267, 45–61.

Alvarado, V. & Manrique, E. (2010). *Enhanced Oil Recovery: Field Planning and Development Strategies*. Elsevier, 1 ed.

Backholm, M., Vuckovac, M., Schreier, J., Latikka, M., Hummel, M., Linder, M. B., & Ras, R. H. A. (2017). Oscillating ferrofluid droplet microrheology of liquid-immersed sessile droplets. *Langmuir*.

Banerjee, S., Fasnacht, M., Garoff, S., & Widom, M. (1999). Elongation of confined ferrofluid droplets under applied fields. *Physical Review E*, 60(4), 4272.

Barthés-Biesel, D. & Acrivos, A. (1973). Deformation and burst of a liquid droplet freely suspended in a linear field. *Journal of Fluid Mechanics*, 61, 1–21.

Bashtovoi, V., Pogirnitskaya, S., & Reks, A. (1999). Dynamics of deformation of magnetic fluid flat drops in a homogeneous longitudinal magnetic field. *Journal of magnetism and magnetic materials*, 201(1), 300–302.

Batchelor, G. K. (1970). Stress system in a suspension of force-free particles. *Journal of Fluid Mechanics*, 41, 545–570.

Bazhlekov, I. B., Anderson, P. D., & Meijer, H. E. H. (2004). Nonsingular Boundary Integral Method for deformable rops in viscous flows. *Physics of Fluids*, 16, 1064–1081.

Bentley, B. J. & Leal, L. G. (1986). An experimental investigation of drop deformation and breakup in steady, two-dimensional linear flows. *Journal of Fluid Mechanics*, 167, 241–283.

Bond, W. N. (1927). Lxxxii. Bubbles and drops and Stokes' law. *The London, Edinburgh, and Dublin Philosophical Magazine and Journal of Science*, 4(24), 889–898.

Bond, W. N. & Newton, D. A. (1928). Lxxxii. Bubbles, drops, and Stokes' law.(paper 2). *The London, Edinburgh, and Dublin Philosophical Magazine and Journal of Science*, 5(30), 794–800.

Brown, D. L., Cortez, R., & Minion, M. L. (2001). Accurate projection methods for the incompressible navier–stokes equations. *Journal of computational physics*, 168(2), 464–499.

Byrom, J., Han, P., Savory, M., & Biswal, S. L. (2014). Directing assembly of dna-coated colloids with magnetic fields to generate rigid, semiflexible, and flexible chains. *Langmuir*, 30(30), 9045–9052.

Chang, Y.-C., Hou, T., Merriman, B., & Osher, S. (1996). A level set formulation of eulerian interface capturing methods for incompressible fluid flows. *Journal of computational Physics*, 124(2), 449–464.

Chorin, A. J. (1967). A numerical method for solving incompressible viscous flow problems. *Journal of computational physics*, 2(1), 12–26.

Cox, R. G. (1969). The deformation of a drop in a general time-dependent fluid flow. *Journal of fluid mechanics*, 37(3), 601–623.

Cristini, V., Blawzdziewicz, J., & Loewenberg, M. (1998). Drop breakup in three-dimensional viscous flows. *Physics of Fluids*, 10, 1781–1783.

Cristini, V., Blawzdziewicz, J., & Loewenberg, M. (2001). An adaptive mesh algorithm for evolving surface: simulations of drop breakup and coalescence. *Journal of Computational Physics*, 168, 445–463.

Croce, R., Griebel, M., & Schweitzer, M. A. (2010). Numerical simulation of bubble and droplet deformation by a level set approach with surface tension in three dimensions. *International Journal for numerical methods in fluids*, 62(9), 963–993.

Cunha, F. R. & Couto, H. L. G. (2008). A new boundary integral formulation to describe three-dimensional motions of interfaces between magnetic fluids. *Applied mathematics and computation*, 199(1), 70–83.

Cunha, F. R. & Sobral, Y. D. (2004). Characterization of the physical parameters in a process of magnetic separation and pressure-driven flow of a magnetic fuid. *Physica A*, 343, 36–64.

Cunha, F. R. & Sobral, Y. D. (2005). Asymptotic solution for pressure-driven flows of magnetic fluids in pipes. *Journal of Magnetism and Magnetic materials*, 289, 314–317.

Cunha, F. R., Sobral, Y. D., & Gontijo, R. G. (2013). Stabilization of concentration waves in fluidized beds of magnetic particles. *Powder technology*, 241, 219–229.

Dailey, J. P., Phillips, J. P., Li, C., & Riffle, J. S. (1999). Synthesis of silicone magnetic fluid for use in eye surgery. *Journal of magnetism and magnetic materials*, 194(1-3), 140–148.

Davis, R. E. & Acrivos, A. (1966). The influence of surfactants on the creeping motion of bubbles. *Chemical Engineering Science*, 21(8), 681–685.

Dimitrakopoulos, P. (2007). Interfacial dynamics in stokes flow via a three-dimensional fully-implicit interfacial spectral boundary element algorithm. *Journal of Computational Physics*, 225(1), 408–426.

Edwards, D., Brenner, H., & Wasan, T. D. (1991). *Interfacial Transport Processes and Rheology*. Butterworth-Heinemann.

Einstein, A. (1906). Eine nene bestimmung der molekuldimension. *Annalen der Physik*, 19, 289–306.

Einstein, A. (1911). Berichtigung zu meiner arbeit: Eine nene bestimmung der molekuldimension. *Annalen der Physik*, 34, 591–592.

Ervik, A. & Bjørklund, E. (2017). The transition in settling velocity of surfactant-covered droplets from the stokes to the Hadamard–Rybczynski solution. *European Journal of Mechanics-B/Fluids*.

Fernández, A. (2008a). Response of an emulsion of leaky dielectric drops immersed in a simple shear flow: Drops more conductive than the suspending fluid. *Physics of fluids*, 20(4), 043303.

Fernández, A. (2008b). Response of an emulsion of leaky dielectric drops immersed in a simple shear flow: Drops more conductive than the suspending fluid. *Physics of fluids*, 20(4), 043303.

Fernández, A. (2009). Shear flow of an emulsion of drops less conductive than the suspending fluid immersed in an electric field by numerical simulation. *Colloids and Surfaces A: Physicochemical and Engineering Aspects*, 338(1-3), 68–79.

Flament, C., Lacis, S., Bacri, J. C., Cebers, A., Neveu, S., & Perzynski, R. (1996). Measurements of ferrofluid surface tension in confined geometry. *Physical Review E*, 53(5), 4801.

Flores, G. A., Liu, J., Mohebi, M., & Jamasbi, N. (1999). Magnetic-field-induced nonequilibrium structures in a ferrofluid emulsion. *Physical Review E*, 59(1), 751.

Ghatage, S. V., Khan, M. S., Peng, Z., Doroodchi, E., Moghtaderi, B., Padhiyar, N., Joshi, J. B., Evans, G. M., & Mitra, S. (2017). Settling/rising of a foreign particle in solid-liquid fluidized beds: Application of dynamic mesh technique. *Chemical Engineering Science.*

Ghigliotti, G., Biben, T., & Misbah, C. (2010). Rheology of a dilute two-dimensional suspension of vesicles. *Journal of Fluid Mechanics*, 653, 489–518.

Gontijo, R. G. (2018). Heat transfer increase for a laminar pipe flow of a magnetic fluid subjected to constant heat flux: an initial theoretical approach. *Mechanics Research Communications*, 91, 27–32.

Griffith, R. M. (1962). The effect of surfactants on the terminal velocity of drops and bubbles. *Chemical Engineering Science*, 17(12), 1057–1070.

Hadamard, J. S. (1911). Motion of liquid drops (viscous). *Comp. Rend. Acad. Sci. Paris*, 154, 1735–1755.

Hakimi, F. S. & Schowalter, W. R. (1980). The effects of shear and vorticity on deformation of a drop. *Journal of Fluid Mechanics*, 98(3), 635–645.

Harlow, F. H. & Welch, J. E. (1965). Numerical calculation of time-dependent viscous incompressible flow of fluid with free surface. *The physics of fluids*, 8(12), 2182–2189.

Hartshorne, H., Backhouse, C. J., & Lee, W. E. (2004). Ferrofluid-based microchip pump and valve. *Sensors and Actuators B: Chemical*, 99(2-3), 592–600.

Hatch, A., Kamholz, A. E., Holman, G., Yager, P., & Bohringer, K. F. (2001). A ferrofluidic magnetic micropump. *Journal of Microelectromechanical systems*, 10(2), 215–221.

Henjes, K. (1995). Maxwell's equations and vorticity: A note on the viscosity of magnetic fluids. *Journal of magnetism and magnetic materials*, 146(3), L236–L240.

Ishii, M. & Zuber, N. (1979). Drag coefficient and relative velocity in bubbly, droplet or particulate flows. *AIChE Journal*, 25(5), 843–855.

Jackson, J. D. (1999). *Classical Electrodynamics.* John Wiley & Sons.

Jeffery, G. B. (1922). The motion of ellipsoidal particles immersed in a viscous fluid. In *Proceedings of the royal society of London A: Mathematical, physical and engineering sciences*, volume 102(715) (pp. 161–179).: The Royal Society.

Jiang, G.-S. & Peng, D. (2000). Weighted eno schemes for hamilton–jacobi equations. *SIAM Journal on Scientific computing*, 21(6), 2126–2143.

Lebedev, A. A. (1916). Stokes' law as applied to liquid balls. *J. Russ. Phys. Chem. Soc. Part. Phys*, 48, 97–131.

Li, D., Banon, S., & Biswal, S. L. (2010). Bending dynamics of dna-linked colloidal particle chains. *Soft Matter*, 6(17), 4197–4204.

Li, G., Tang, C.-a., & Li, L.-c. (2013). High-efficiency improved symmetric successive over-relaxation preconditioned conjugate gradient method for solving large-scale finite element linear equations. *Applied Mathematics and Mechanics*, 34(10), 1225–1236.

Liu, J., Lawrence, E. M., Wu, A., Ivey, M. L., Flores, G. A., Javier, K., Bibette, J., & Richard, J. (1995). Field-induced structures in ferrofluid emulsions. *Physical review letters*, 74(14), 2828.

Lübbe, A. S., Alexiou, C., & Bergemann, C. (2001). Clinical applications of magnetic drug targeting. *Journal of Surgical Research*, 95(2), 200–206.

Mahlmann, S. & Papageorgiou, D. T. (2009). Numerical study of electric field effects on the deformation of two-dimensional liquid drops in simple shear flow at arbitrary Reynolds number. *Journal of Fluid Mechanics*, 626, 367–393.

Malvar, S., Gontijo, R. G., & Cunha, F. R. (2018). Nonlinear motion of an oscillating bubble immersed in a magnetic fluid. *Journal of Engineering Mathematics*, 108, 143–170.

Mandal, S. & Chakraborty, S. (2017a). Effect of uniform electric field on the drop deformation in simple shear flow and emulsion shear rheology. *Physics of Fluids*, 29(7), 072109.

Mandal, S. & Chakraborty, S. (2017b). Uniform electric-field-induced non-newtonian rheology of a dilute suspension of deformable Newtonian drops. *Physics Review Fluids*, 2(9), 093602.

Mefford, O. T., Woodward, R. C., Goff, J. D., Vadala, T. P., Pierre, T. G. S., Dailey, J. P., & Riffle, J. S. (2007). Field-induced motion of ferrofluids through immiscible viscous media: Testbed for restorative treatment of retinal detachment. *Journal of Magnetism and Magnetic Materials*, 311(1), 347–353.

Mulder, W., Osher, S., & Sethian, J. A. (1992). Computing interface motion in compressible gas dynamics. *Journal of Computational Physics*, 100(2), 209–228.

Odenbach, S. (2008). *Ferrofluids: magnetically controllable fluids and their applications*, volume 594. Springer.

Odenbach, S. (2009). *Colloidal magnetic fluids: basics, development and application of ferrofluids*, volume 763. Springer.

Oh, D.-W., Jin, J. S., Choi, J. H., Kim, H.-Y., & Lee, J. S. (2007). A microfluidic chaotic mixer using ferrofluid. *Journal of Micromechanics and Microengineering*, 17(10), 2077.

Oliveira, T. F. & Cunha, F. R. (2011). A theoretical description of a dilute emulsion of very viscous drops undergoing unsteady simple shear. *Journal of Fluids Engineering*, 133, 101208.

Oliveira, T. F. & Cunha, F. R. (2015). Emulsion rheology for steady and oscillatory shear flows at moderate and high viscosity ratio. *Rheologica Acta*, 54, 951–971.

Osher, S. & Sethian, J. A. (1988). Fronts propagating with curvature-dependent speed: algorithms based on Hamilton-Jacobi formulations. *Journal of computational physics*, 79(1), 12–49.

Patankar, S. (1980). *Numerical heat transfer and fluid flow.* CRC press.

Peng, D., Merriman, B., Osher, S., Zhao, H., & Kang, M. (1999). A pde-based fast local level set method. *Journal of computational physics*, 155(2), 410–438.

Puri, I. K. & Ganguly, R. (2014). Particle transport in therapeutic magnetic fields. *Annual Review of Fluid Mechanics*, 46, 407–440.

Rosa, A. P., Gontijo, R. G., & Cunha, F. R. (2016). Laminar pipe flow with drag reduction induced by a magnetic field gradient. *Applied Mathematical Modelling*, 40(5-6), 3907–3918.

Rosensweig, R. (1997). *Ferrohydrodynamics.* Dover Books on Physics. Dover Publications.

Rosensweig, R. E. (1987). Magnetic fluids. *Annual review of fluid mechanics*, 19(1), 437–461.

Rowghanian, P., Meinhart, C. D., & Campàs, O. (2016). Dynamics of ferrofluid drop deformations under spatially uniform magnetic fields. *Journal of Fluid Mechanics*, 802, 245–262.

Rybczynski, W. (1911). On the translatory motion of a fluid sphere in a viscous medium. *Bull. Acad. Sci., Cracow, Series A*, 40.

Sadhal, S. S. & Johnson, R. E. (1983). Stokes flow past bubbles and drops partially coated with thin films. part 1. stagnant cap of surfactant film–exact solution. *Journal of Fluid Mechanics*, 126, 237–250.

Salac, D. & Miksis, M. (2011). A level set projection model of lipid vesicles in general flows. *Journal of Computational Physics*, 230(22), 8192–8215.

Scherer, C. (2005). Computer simulation of magnetorheological transition on a ferrofluid emulsion. *Journal of magnetism and magnetic materials*, 289, 196–198.

Schowalter, W. R., Chaffey, C. E., & Brenner, H. (1968). Rheological behavior of a dilute emulsion. *Journal of colloid and interface science*, 26(2), 152–160.

Sero-Guillaume, O. E., Zouaoui, D., Bernardin, D., & Brancher, J. P. (1992). The shape of a magnetic liquid drop. *Journal of Fluid Mechanics*, 241, 215–232.

Sherwood, J. D. (1988). Breakup of fluid droplets in electric and magnetic fields. *Journal of Fluid Mechanics*, 188, 133–146.

Shi, D., Bi, Q., He, Y., & Zhou, R. (2014a). Experimental investigation on falling ferrofluid droplets in vertical magnetic fields. *Experimental Thermal and Fluid Science*, 54, 313–320.

Shi, D., Bi, Q., & Zhou, R. (2014b). Numerical simulation of a falling ferrofluid droplet in a uniform magnetic field by the VOSET method. *Numerical Heat Transfer, Part A: Applications*, 66(2), 144–164.

Shliomis, M. I. (1971). Effective viscosity of magnetic suspensions. *Zh. Eksp. Teor. Fiz*, 61, 2411–2418.

Shliomis, M. I. (1974). Magnetic fluids. *Soviet Physics Uspekhi*, 17(2), 153.

Shliomis, M. I. (2001). Comment on magnetoviscosity and relaxation in ferrofluids. *Physical Review E*, 64(6), 063501.

Shu, C.-W. & Osher, S. (1988). Efficient implementation of essentially non-oscillatory shock-capturing schemes. *Journal of computational physics*, 77(2), 439–471.

Silvey, O. W. (1916). Comparison of the fall of a droplet in a liquid and in a gas. *Physical Review*, 7(1), 87.

Sjöblom, J. (1992). *Emulsions – A Fundamental Approach*. Kluwer Academic Publishes.

Sobral, Y. D. & Cunha, F. R. (2003). A stability analysis of a magnetic fluidized bed. *Journal of magnetism and magnetic materials*, 258, 464–467.

Sobral, Y. D. & Cunha, F. R. (2005). Drift velocity and deformation of polarized drops in magnetic fields. *Journal of magnetism and magnetic materials*, 289, 318–320.

Stewart, I. (2012). *In pursuit of the unknown: 17 equations that changed the world*. Basic Books.

Stokes, G. G. (1851). On the effect of the internal friction of fluids on the motion of pendulums. *Transactions of the Cambridge Philosophical Society*, 9, 8.

Sussman, M., Smereka, P., & Osher, S. (1994). A level set approach for computing solutions to incompressible two-phase flow. *Journal of Computational physics*, 114(1), 146–159.

Taylor, G. I. (1932). The viscosity of a fluid containing small drops of another fluid. *Proceedings of the Royal Society of London. Series A, Containing Papers of a Mathematical and Physical Character*, 138(834), 41–48.

Taylor, G. I. (1934). The formation of emulsions in definable fields of flow. *Proceedings of the Royal Society of London. Series A, Containing Papers of a Mathematical and Physical Character*, 146(858), 501–523.

Torza, S., Cox, R. G., & Mason, S. G. (1972). Particle motions in sheared suspensions xxvii. transient and steady deformation and burst of liquid drops. *Journal of colloid and interface science*, 38(2), 395–411.

Unverdi, S. O. & Tryggvason, G. (1992). A front-tracking method for viscous, incompressible, multi-fluid flows. *Journal of computational physics*, 100(1), 25–37.

Vlahovska, P. M. (2011). On the rheology of a dilute emulsion in a uniform electric field. *Journal of Fluid Mechanics*, 670, 481–503.

Vlahovska, P. M., Blawzdziewicz, J., & Loewenberg, M. (2002). Nonlinear rheology of a dilute emulsion of surfactant-covered spherical drops in time-dependent flows. *Journal of Fluid Mechanics*, 463, 1–24.

Voltairas, P. A., Fotiadis, D. I., & Massalas, C. V. (2001). Elastic stability of silicone ferrofluid internal tamponade (sfit) in retinal detachment surgery. *Journal of Magnetism and Magnetic Materials*, 225(1-2), 248–255.

Voltairas, P. A., Fotiadis, D. I., & Michalis, L. K. (2002). Hydrodynamics of magnetic drug targeting. *Journal of Biomechanics*, 35(6), 813–821.

Zakinyan, A. & Dikansky, Y. (2011). Drops deformation and magnetic permeability of a ferrofluid emulsion. *Colloids and Surfaces A: Physicochemical and Engineering Aspects*, 380(1), 314–318.